Università degli Studi di Torino
Scuola di Dottorato in Scienza ed Alta Tecnologia

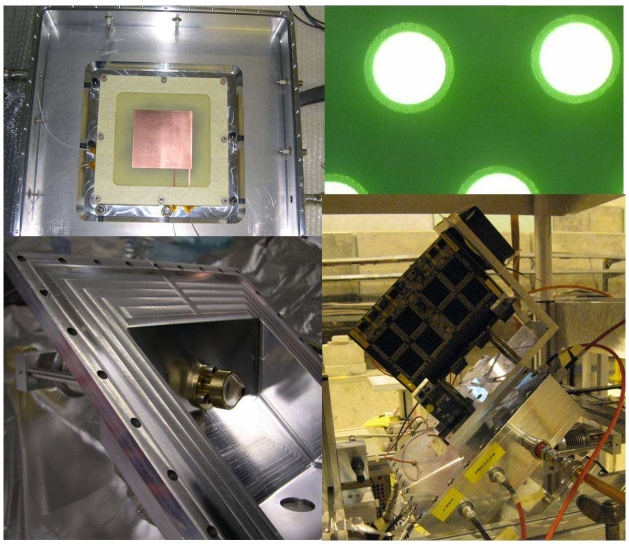

Development of a gaseous photon detector for Cherenkov imaging applications

Elena Rocco

Università degli Studi di Torino
Scuola di Dottorato in Scienza ed Alta Tecnologia

Indirizzo di Fisica ed Astrofisica

Development of a gaseous photon detector for Cherenkov imaging applications

Elena Rocco

Tutor: Prof. Daniele Panzieri
Co-Supervisor: Dr. Silvia Dalla Torre

A Matteo, papà, mamma e Lara.

Contents

Chapter 1

Introduction

This thesis is dedicated to the R&D activity aiming at a novel micro pattern gaseous photon detector based on the THick Gas Electron Multiplier (THGEM). The goal application of the novel photon detector is the detection of single photon in Ring Imaging CHerenkov (RICH) counters. The THGEM principle is derived from the Gas Electron Multiplier (GEM) one, even if the material, the production technology and the size scale are different: a THGEM is a Circuit Printed Board (PCB) coated with thin copper layers on both faces, with holes obtained by drilling. Part of the THGEM features are similar to those of the GEMs, but a number of characteristics aspects result substantially different: in fact, if the geometrical parameters can be scaled from the GEM ones, the parameters related to the electrons multiplication, which is a microscopic physical phenomenon, do not. This is why, before starting the photon detector development, we have performed a systematic study of the THGEM multiplier. A photon detector is formed coupling a multi layer THGEM-based detector with a solid state caesium iodide (CsI) photo cathode. We have studied the properties of THGEM-based photon detector prototypes. The next step of the R&D programme, not included in this thesis, is the engineering phase, needed to realise sets of large size photon detectors.

The structure of this thesis is the following: Chapters 2-4 are dedicated to reviewing existing information concerning RICH counters, GEMs and THGEMs; the following chapters describe the original R&D work.

More in detail, this introduction (Chapter 1), is followed by a short

overview of the Cherenkov imaging counters and of the detectors of single photons employed (Chapter 2). Chapter 3 is devoted to the GEM-based detectors of ionising particles, briefly recalling their structure and their main properties, as well as the recent and future GEM applications. In Chapter 4 the information about THGEM present available in the literature is summarised.

In Chapter 5 the laboratory equipment used for the R&D activity is described, including custom devices developed for this activity. The studies related to the THGEM production aspects are presented in Chapter 6. The systematic studies of single layer THGEM-detectors performed to characterise the THGEM electron multipliers in detecting ionising particle are reported in Chapter 7. Chapter 8 is dedicated an experimental re-visitation of the effective CsI quantum efficiency in gaseous atmosphere as a function of the electric field. The results obtained with a multi-layer THGEM photon detector are reported in Chapter 9. Conclusions and an outlook are given in Chapter 10.

This detector development is performed by an European Collaboration including several institutes[1]. This activity is also part of the scientific program of the RD51 Collaboration [1]. My personal contribution concerns the laboratory studies described in Chapters 7, 8 and 9.

[1]CERN, European Organisation for Nuclear Research, Geneva, Switzerland; Charles University, Praha, Czech Republic and JINR, Dubna, Russia; INFN, Sezione di Torino, Torino, Italy; INFN, Sezione di Torino and University of the East Piemonte, Alessandria, Italy, INFN, Sezione di Torino and University of Torino, Torino, Italy; INFN, Sezione di Trieste, Trieste, Italy; INFN, Sezione di Trieste and University of Trieste, Trieste, Italy; Technical University of Liberec, Liberec, Czech Republic; TERA Foundation, Novara, Italy; Universitä Freiburg, Physikalisches Institut, Freiburg, Germany

Chapter 2

Cherenkov Imaging Counters and Detectors of Single Photons

2.1 The Cherenkov radiation

The Cherenkov radiation, named after the Russian physicist who discovered it [2], is produced by a charged particle moving through a medium with a velocity greater than the local phase velocity of light: a glow analogous to a sonic shock wave is emitted. The theoretical interpretation based on classical dynamics [3] is based on the fact that the atoms of the medium become polarised in the region along the charged particle track. Owing to transient nature of this phenomenon, polarised atoms relax back to the equilibrium by emitting a short electromagnetic pulse. When the velocity of the particle doesn't exceed the local phase velocity of the light, the emitted electromagnetic pulses interfere destructively. Otherwise, namely, when the particle moves faster than the light phase velocity, a coherent wavefront, at a specific angle θ_C with respect to the particle direction, is produced: in fact, in these conditions, the polarisation field is symmetric along the particle track. The bandwidth of frequencies covered by the Cherenkov radiation corresponds to the Fourier transformed components of the electromagnetic pulses emitted by the medium dipoles. Even if the photons emitted by Cherenkov effect are few, an order of magnitude smaller than the photons emitted in scintillating

material, the threshold nature of the effect and the fixed direction of the Cherenkov light offer a powerful tool for the application in ionising particle detectors. The basic equation which includes the properties of the Cherenkov radiation is:

$$cos\theta_C = \frac{1}{n\beta} \tag{2.1}$$

which links the emission angle θ_C of Cherenkov photons to the velocity of the charged particle given in units of the speed of light and to the refractive index n of the medium. Equation 2.1 is known as the Cherenkov equation. The spectral dependence of the radiation is described by Frank and Tamm's equation; the energy radiated per unit path length dx by a particle of charge Ze is:

$$\frac{d^2W}{dxd\omega} = \frac{Z^2e^2\omega}{c^2}\left(1 - \frac{1}{\beta^2 n^2(\omega)}\right) \tag{2.2}$$

The chromatic dispersion of the optical medium results in a dependence of the refractive index n from the radiation frequency: $n{=}n(\omega)$.

The number N of Cherenkov photons emitted with energy $\hbar\omega$ is deducible from the Frank and Tamm's equation:

$$N = 2\pi L Z^2 \alpha \int_{\beta n>1} \left[1 - \left(\frac{\beta_t(\lambda)}{\beta}\right)^2\right] \frac{d\lambda}{\lambda^2} \tag{2.3}$$

where α is the fine structure constant, λ is the light wavelength, L is the radiating path length and β_t is the particle velocity corresponding to the threshold of the Cherenkov effect and it is a function of λ due to the chromaticity of the medium.

2.2 Cherenkov Imaging Counter

A particle is identified when its mass and charge are determined. The mass determination is performed by measuring a couple of kinematic quantities, so that the equations of the special relativity can be solved. The most typical experimental approach consists in the measurement of momentum and

velocity. The momentum is usually determined by the particle deflection in magnetic field. The relation between the momentum and the velocity in unit of speed light is the following:

$$p = mc\gamma\beta \tag{2.4}$$

A counter able to provide an independent measurement of the velocity makes it possible to identify the particle. This is why equipments used to measure particle velocity are regarded as detectors for Particle IDentification (PID). Particle detectors based on the Cherenkov effect and making use only of its threshold property are known as threshold Cherenkov counters; historically, the first use of the Cherenkov effect in the field of particle counters is of this type. These detectors allow to discriminate between two particle species on the base of the detector response; no direct measurement of the particle velocity is performed. Discrimination between particle species is also performed using Differential Cherenkov counters, but in this case the detectors make use of the directionality of the Cherenkov radiation, namely of the fixed emission angle.

The particle velocity is measured employing Ring Imaging CHerenkov counters (RICH).

The Cherenkov Imaging Counters are detectors used for PID in a wide momentum domain and able to operate effectively also when the final state is characterised by large particle multiplicity; they offer a superior resolution in the measurement of β of the particles with velocity v=βc. From equation 2.4, the precision of the mass determination is:

$$\left(\frac{dm}{m}\right)^2 = \left(\gamma^2\frac{d\beta}{\beta}\right)^2 + \left(\frac{dp}{p}\right)^2 \tag{2.5}$$

For the momentum p relatively well measured, the resolution of particles with masses m_1 and m_2 requires a velocity resolution $\Delta\beta$ given by:

$$\frac{\Delta\beta}{\beta} \simeq \frac{m_1^2 - m_2^2}{2p^2} \tag{2.6}$$

The basic components always present in a RICH detector are:

- the transparent dielectric medium, called radiator, whose refractive index is appropriate for the range of particle momentum being measured, where the Cherenkov light is emitted and transmitted;

- the photon detector, where the photons are converted into photoelectrons, in order to be detected.

More components can be required according to the different implementation, as shortly discussed below. In all cases, the optical properties of the radiator and the other optical media are fundamental elements to take into account when designing a RICH detector.

Moreover, one has to deal with many sources of inefficiency as the reflection losses at the medium interfaces, the materials which have to be fully isotropic to the polarised light, the multiple scattering in the radiator, the aberration of the optical systems and the efficiency of the photon detector. These effects either reduce the number of detected photons or limit the detector resolution.

In particular, the chromatic aberration of the radiator $\frac{\Delta n}{n}$ is usually the dominant contribution to the detector precision $\frac{\sigma_\beta}{\beta}$ especially for RICH detector operating in the ultraviolet region, where the chromatic effects are stronger.

A complete discussion about the limit of the accuracy of the Cherenkov angle measurement and its resolution is beyond the scope of this thesis (a complete analysis can be found in [4] and references therein). The point to be stressed is that an improvement in number of photons detected allows to improve the accuracy of the measurement of the Cherenkov angle.

Three architectures have been used in experiment. In the following they are illustrated via outstanding examples.

RICH counters with focusing system are used when the radiator volume is extended and, thus, no image can be formed without proper focusing (Fig. 2.1). This is the case when the radiator material has low density, namely when radiator material in gas phase is used, a compulsory choice to perform PID at high momenta ($\geq$ 10 GeV/c). In fact, this application requires radiator material with very low-value refractive index; to detect a

number of Cherenkov photons adequate for effective imaging, a long particle path through the radiator volume is needed (typically from 1 m to 10 m and more). COMPASS RICH-1 is in operation at the COMPASS experiment at CERN SPS since 2001, in its initial version [5] up to 2004 and in its upgraded version [6] characterised by a more powerful photon detection system since 2006. Its large transverse size matches the large angular acceptance of the COMPASS spectrometer. RICH-1 employs a gaseous radiator: particles cross 3 m of C_4F_{10}. Image focusing is obtained by means of a 21 m^2 wall formed by a mosaic arrangement of 116 spherical UV mirror elements. In its upgraded version, RICH-1 is equipped with two different photon detection systems. In the peripheral regions (75% of the surface), populated by the images produced by lower momentum hadrons, and where the uncorrelated background level is less severe, the photon detectors are MultiWire Proportional Chambers (MWPC) equipped with solid state CsI photocathodes (Sec. 2.3).

The Cherenkov images produced by the high momenta particles are detected in the central photon detection area (25% of the surface), a region highly populated by images due to the uncorrelated background generated by the huge halo of the muon beam. Here very good resolution of the measured Cherenkov angle to perform PID at high momenta and time resolution at the ns level to discriminate the uncorrelated background are needed. This region is instrumented with a fast detection system based on MultiAnode PhotoMultiplier Tubes (MAPMT) coupled to individual telescopes of fused silica lenses to enlarge the active area of the photon detectors. The system allows the detection of about four times more Cherenkov photons than in the peripheral detectors. At saturation, namely for particle with $\beta \rightarrow 1$, the number of detected photons per ring is on average 56 (about 14 with the MWPCs) and the Cherenkov angle is measured with a resolution of $\sigma = 0.3$ mrad (0.6 mrad in the peripheral region).

RICH counters with proximity focusing scheme are employed when thin radiator layers (typically about 1 cm) are used (Fig. 2.2). Dense radiator materials, namely in liquid or solid phase, are required to detect enough photons for effective imaging. Correspondingly, the refractive index has large

values and the domain of application is the few GeV/c momentum range (indicatively < 5 GeV/c). ALICE HMPID [7] is an extended counter ready for data taking at the CERN LHC experiment ALICE. It consists of 7 large size proximity focusing RICH modules; the radiator layer is formed by 15 mm of C_6F_{14} in liquid phase and the photon detectors are MWPCs with CsI photocathodes. The expansion gap is 80 mm long. A smaller detector with the same architecture has been used at the STAR experiment at Brookhaven National Laboratory (BNL) RHIC [8]; its performance confirm the HMPID expected one, namely π-K separation up to 3 GeV/c and π-p separation up to 5 GeV/c.

A single detector based on the principle of the **Detection of Internally Reflected Cherenkov light** (**DIRC**, Fig. 2.3) has been used in an experiment so far: the BABAR DIRC [9] in operation till Spring 2008 at the BABAR experiment at SLAC. In this detector, long (4.9 m) fused silica bars form both the radiator elements and the light guides. The majority of the Cherenkov photons produced in the bars by the through-going particles are trapped inside the bar due to total refraction. The bar faces are parallel and optically polished; the photons travel by reflections along the bar preserving their angular information. At the end of the bars, the photons enter an expansion volume 1.1 m long, filled with demineralised water, and they are detected in a set of about 11 thousand PhotoMultiplier Tubes (PMT). The lever arm length and the size of two cross-sections, namely the bar one and PMT cathode area, dictate the angular resolution. The separation between kaons and pions is about 4σ at 3 GeV/c declining to about 2.5σ at 4.1 GeV/c.

The number of fields of experimental studies where RICH counters are required is continuously increasing and it includes a large number of sectors in particle, nuclear and astroparticle physics: physics at high energy electron-positron colliders, quark spectroscopy, B and K physics, nucleon structure studies, heavy ion physics and quark-gluon fusion, hypernuclei, and space-born experiments to study the cosmic ray composition.

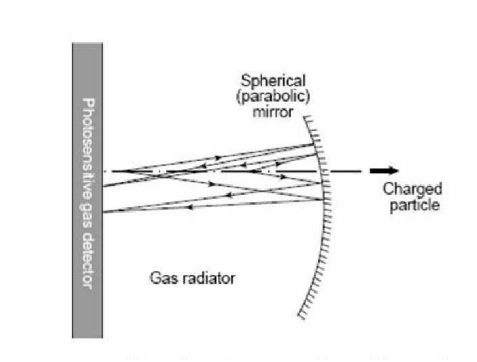

Figure 2.1: Scheme of focusig RICH [4].

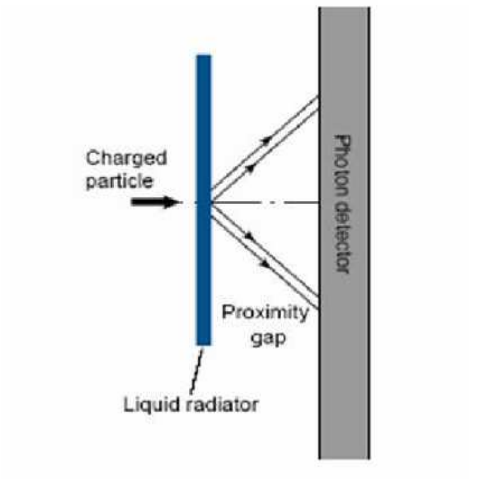

Figure 2.2: Scheme of proximity-focusing RICH [4].

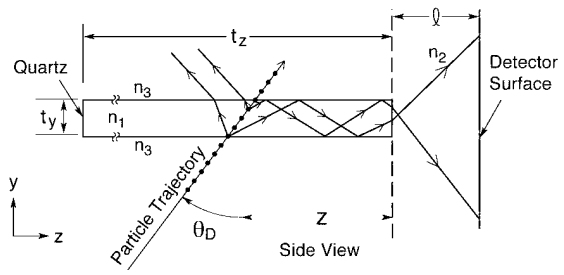

Figure 2.3: Principle scheme of a DIRC [9].

2.3 Single photon detectors for imaging applications

In RICH counters, the photon detectors are a crucial component. The detection is obtained by two steps: the conversion of the photon into a photoelectron and the amplification of the signal to make it detectable. The Cherenkov quanta are low in energy and the only conversion mechanism exploitable for practical purposes is the photoelectric absorption. The property of a material to convert single photons is given in term of its Quantum Efficiency (QE), namely the percentage of photons converted. The photoconverter can be a vapour or a thin layer of material in solid state. A good photon detector must provide the possibility to detect with high efficiency the single photoelectrons. For application in RICH counters, the photon detector must fulfil also other requirements:

- good localisation accuracy, needed for imaging;
- long-term stability;
- fast response, important in particular for high rate experiments;
- low cost, a requirement related to the wide surfaces that often have to be instrumented in RICHes.

Photon detector belong to three families: vacuum-based, solid state and gaseous detectors. So far, only vacuum-based and gaseous ones have been used for Cherenkov imaging applications in experiments.

The **vacuum-based detectors**, namely Photon Multiplier Tubes (PMTs) and the other photon detectors derived from this scheme, are very attractive because of several features. Their sensitivity is in the visible region, sometime extended to the near UV domain, thus converting photons in an extended wavelength range, resulting in a large number of converted photons; moreover, good medium transparency and mirror reflectance are more easily obtained for visible and near UV photons. PMTs offer high rate capability. Since several years, the technology to segment them is well established and

thus they offer segmentation flexibility. They are also compact, robust and have low noise level. The big drawbacks are their sensitivity to the magnetic field and the high cost per channel. PMTs have been used for Cherenkov imaging counters in SELEX [10] at Fermilab, in BABAR [11] at SLAC and in PHENIX [12] at Brookhaven National Laboratory. The MultiAnode PMTs (MAPMTs) are the pixelised version of the PMTs and offer the advantage of many channels with a single common power supply and a compact read-out, even if the cost for a single channel is still relevant. In good quality MAPMTs, as those produced by Hamamatsu[1] (Fig. 2.4), the cross-talk is less than 1% and the gain variation from channel to channel is less than 30% [14]. The MAPMTs have been used in HERA-B RICH [13] and they are currently used for the photon detection in the central part of the RICH in COMPASS [6].

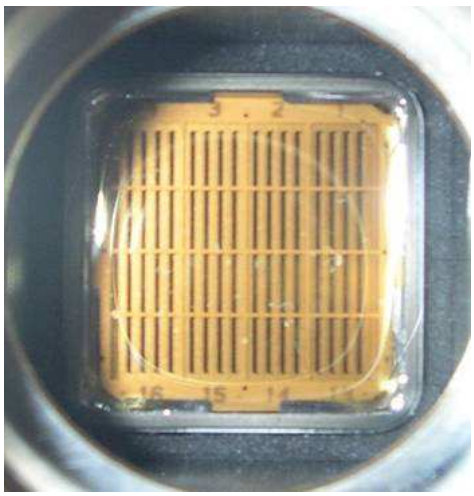

Figure 2.4: Front view of MAPMT, R7600-03-M16, produced by Hamamatsu K.K..

In Hybrid Photon Detectors (HPD) (Fig. 2.5), the photoelectron is accelerated by a strong voltage (several kV) and it hits a **solid state detector**, where the electron kinetic energy is converted in couples electron-hole, which form the signal. If the solid state detector is pixelised and if the electric field between the photocathode and the solid state detector allows to preserve a

[1]Hamamatsu Photonics K.K.

correspondence between the photon conversion point and the photoelectron arrival point at the solid state detector, the HPDs can be pixelised. Custom HPDs are actually used in the LHC-b experiment [15] at CERN.

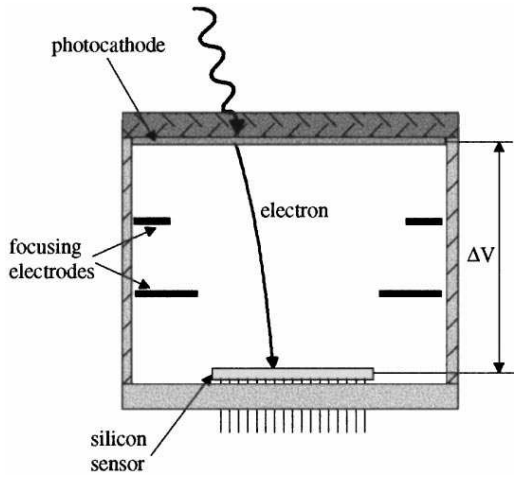

Figure 2.5: The principle of Hybrid Photon Detector [15].

Si-PM are solid state detectors are formed by matrix of microcells read out in parallel; each cell is a diode (Avalanche PhotoDiode, APD) operated in avalanche mode. The device typical size is from 1 mm×1 mm to 3 mm×3 mm; the microcells have typical size from 20 μm×20 μm to 50 μm×50 μm. They operate at low voltage (30÷80 V), they are insensitive to the magnetic field. They offer time resolution below 100 ps. Their major limitation is due to the thermal noise, at the first order proportional to the active surface: this limits the size of the device. Silicon photomultipliers are becoming mature detectors with the first use of a large set in an experiment [16]. In spite of laboratory and test beam studies of Si-PM in Cherenkov imaging applications [17], the detection of single photons remains problematic, due to the large noise rate of the devices (of the order of MHz per device at room temperature), to the non negligible cross-talk and after-pulse probability, and to ageing issues related to limited radiation hardness.

The class of **gaseous photon detectors** includes: MultiWire Proportional Chambers (MWPCs), MultiStep Avalanche Chambers (MSACs) and Drift Chambers (DCs). In the gaseous photon detectors, the mechanism of the detection of the Cherenkov photons is the following: the photoconversion of the Cherenkov radiation takes place in a solid or vapour photoconverter, then the photoelectrons drift guided by the electric field and reach the high field multiplication region, where an avalanche is formed.

The resulting ionisation is so large to be detected by a cathode electrode subdivided into pads and instrumented with sensitive electronic system. The pad address gives an ambiguity-free two-dimensional image, allowing the reconstruction of overlapping rings from a multi-particle event.

In the first generation of these detectors photoconverting vapours as TEA (Triethylamine) and TMAE (Tetrakis Dimethylamine Ethylene) were added to the detector gas mixtures. These photon detectors have given a key contribution in establishing RICH counters as solid and reliable for physics experiments (DELPHI RICHes [18], CRID [19], Omega RICH [20]). The use of both vapours presents several limitations; chemically, they are very reactive and aggressive. TEA converts only photons with wavelength below 180 nm, namely in a very far UV region. TMAE has low vapour pressure at room temperature and the amount of vapour that can be added to the detector gas atmosphere is low; as a consequence, to get good photoconversion rate, either the photon path in the gas must be long or the photon detector must be kept at high temperature.

Due to these limitations, the photoconverting vapours have been progressively abandoned. At present, the CLEO III RICH [21] is the only imaging Cherenkov counter in operation making use of photoconverting vapours.

The second generation of gaseous photon detectors is represented by MultiWire Proportional Chambers (MWPC), where a cathode plane is coated with a Caesium Iodide (CsI) layer, developed by the RD26 collaboration [22]; the other MWPC cathode is formed by parallel wires, so to have large transparency for the incoming photons, that enter the chamber volume via a fused silica plate. This material for the detector window is required because CsI converts photon with wavelength shorter than 200 nm. A technique to

coat photocathode plates with large area, up to 60×60 cm^2, with Caesium Iodide (CsI) was developed. The best CsI QE is obtained by depositing at least 250 nm of CsI onto a PCB with a copper coating, accurately polished by mechanical and chemical treatments, and afterwards, covered with a thick (7 μm) chemically-deposited nickel layer, followed by a thiner (0.5 μm) layer of gold. During the deposition, the pad substrate is held at 50°C. A twelve-hours post-deposition heat treatment at 60°C, under vacuum, is necessary in order to achieve the final CsI QE. Comparing with the previous generation of gaseous photon detectors discussed above, the CsI photon detector has an improved Cherenkov angle resolution, since the photoconversion is achieved in a single layer without parallax error, which is the case in gaseous detectors with photoconverting vapours. MWPC with a thin CsI deposit on the photocathode was the right choice for many experiments as NA44 [23], HADES [24], COMPASS [25], STAR [8], JLab-HallA [26], ALICE [7] and it was a remarkable success of proving that the solid state photoconverters can operate in gaseous atmosphere. Unfortunately these photon detectors suffer because of some performance limitations; ageing, resulting in a severe decrease of quantum efficiency, is reported after a collected charge of the order of some mC/cm^2 [27] and electrical instabilities accompanied by a long recovery time (about 1 day) [25], a fact which imposes to operate at lower voltage, namely at lower gain: the efficiency in single photon detection results reduced. Due to the open geometry of the photon detector, the ions coming from the multiplication avalanche bombard the photocathode, causing the effects mentioned above.

Nevertheless, the use of gaseous photon detectors is still mandatory because they represent the only option of equipping large areas at affordable costs.

2.4 A new generation of gaseous detectors for Cherenkov imaging counters

To overcome the performance limitations of the MWPC with CsI photocathode described in Sec. 2.3, a new generation of photon detectors is being

developed: they are characterised by a structure such that the ions bombardment of the photocathode is reduced, namely by a closed geometry. Recent developments of MicroPattern Gaseous Detectors (MPGD) look encouraging under this aspect. When a multilayer structure of electron multipliers is used, a good fraction of the ions is trapped in the intermediate layers and don't reach the photocathode. In the PHENIX experiment at RHIC, the Hadron Blind Detector (HBD) represents the first application of this idea. It is a windowless threshold Cherenkov detector, operated with pure CF_4, which is also the radiator gas, with a CsI photocathode; the photon detector has a triple GEM structure and a readout anode plane segmented in large pads, which detect several photoelectron per particle (Fig. 2.6) [28]. The total photon detector gain is about 5000.

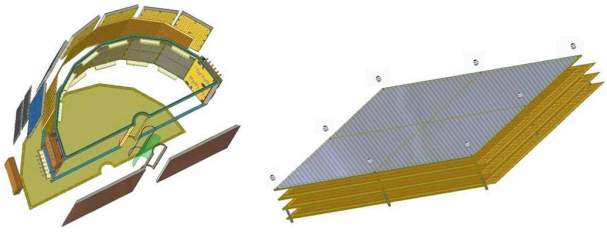

Figure 2.6: Left: exploded view of the HBD detector. One side panel is removed for clarity. Right: a photo-detector module consisting of a three GEMs and a mesh [29].

It is worthwhile to stress that for imaging counters the effective detection of single photons is needed, thus larger gain are required.

The Polya distribution describes the distribution of the amplified signal generated starting from a single electron. Its formal expression is:

$$P(q) = \left(\frac{q(1+\theta)}{\bar{q}}\right)^{\theta} exp\left(\frac{-q(1+\theta)}{\bar{q}}\right) \tag{2.7}$$

where $\bar{q}$ is the mean charge of the avalanche and θ is an empirical parameter related to the amplification mechanism: it depends on the gas properties and on the detector geometry. Examples of Polya distribution are shown in Fig. 2.7. For $\theta = 0$ the Polya distribution coincides with an exponential one. If the multiplication factor does not undergo large variations, the parameter

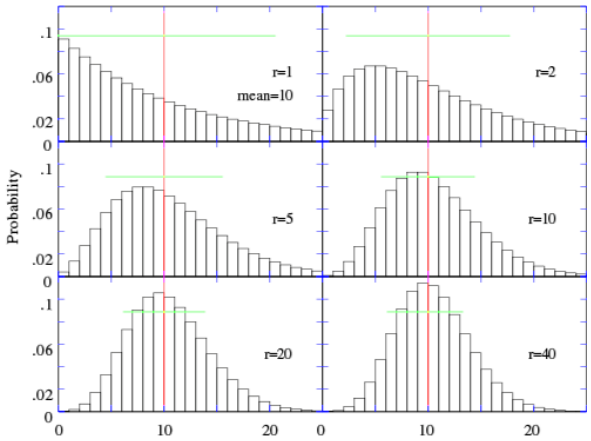

Figure 2.7: Examples of the Polya distribution for $\bar{q}$=1 and for several θ=r-1 values starting for θ=0.

θ is substantially different from 0. In general, θ increases at larger detector gain, even if it can remain very small also at high gain for detectors with non homogeneous gain. Summarising, operating a single photon detector at large gain offers two handles to increase the photon detection efficiency: larger signals are easier to detect, the amplitude distribution can develop from the exponential shape peaked at the origin, into a Polya one, with a peak at larger amplitudes.

This thesis is dedicated to an R&D of gaseous photon detector suitable for Cherenkov imaging applications, based on the THick GEM (THGEM) electron multiplier.

Chapter 3

GEM-based detector of ionising particles

3.1 The gaseous detectors of ionising particles

Ionisation detectors are the first electrical devices developed to detect radiation. These instruments are based on the direct collection of the ionisation electrons and ions produced in a gas by the passing radiation. During the first half of the past century, three basic types of gaseous detectors have been developed: the *ionisation chamber*, the *proportional counter* and the *Geiger-Müller counter* [30]. Gas is the natural medium to use to collect the ionisation charge produced by ionising particles because of the greater mobility of electrons and ions. The three detector types mentioned above are substantially the same device operated in different conditions and exploiting different phenomena. The common working principle is the collection of the electrons released by the atoms of the gas ionised by the charged particle passing through it; the presence of an electric field causes the electron drift; when the field intensity is high enough, the multiplication of the primary charge occurs. The number of the ionised atoms depends on the deposited energy and on the specific gas. The proportionality between the number of ionised atoms and the signal read-out depends on the nature of the multiplication process: different intensities of the electric field and different gasses result in multiplication processes with different characteristics.

In Fig. 3.1 the total charge collected as function of the voltage applied in a single wire gas chamber is shown. At zero voltage no charge is collected as the ion-electron pairs recombine under their own electrical attraction. As the voltage is raised, however, the recombination forces are overcome and the current increases: more and more electron-ion pairs are collected before they can recombine. A plateau is reached when all the pairs created are collected and a further voltage increase do no result in a larger current. A detector working in this region (II in Fig. 3.1) is called *ionisation chamber*. Increasing the voltage much further, the electric field at the wire electrode becomes strong enough to accelerate freed electrons to an energy large enough to ionise the gas molecules. The result is an ionisation avalanche or cascade. It is important to emphasise that the number of electron-ion pairs in the avalanche is directly proportional to the number of primary electrons. A detector working in this region (III in Fig. 3.1) is known as a *proportional chamber*. At larger voltages, the total amount of ionisation created in the multiplication process becomes so large that the space charge distorts the electric field. The proportionality begins to be lost. This region is known as *the region of the limited proportionality*. At even higher voltages, the energy becomes so large that a discharge occurs in the gas: the signal is saturated and any proportionality is lost. Detectors operating in this region are called *Geiger-Müller counters*; in the voltage range of this regime, the current is substantially constant because the signals are saturated. If the voltage is still raised, a continuous breakdown occurs with or without radiation and in these conditions the device can no longer be used as particle detector.

One of the basic requirements of experimental particle physics is the determination of the particle trajectories, measuring coordinates along the particle path. Up until approximately 1970, all tracking devices were providing trajectories via optical images: photographic emulsions, cloud chambers, bubbler chambers, spark chambers and similar ones. The breakthrough occurred in 1968 with the invention of the MultiWire Proportional Chamber (MWPC) by George Charpak, later Nobel Prize laureate. He proved that an array of many closely spaced anode wires included in the same chamber could act as an array of independent proportional counter. Moreover,

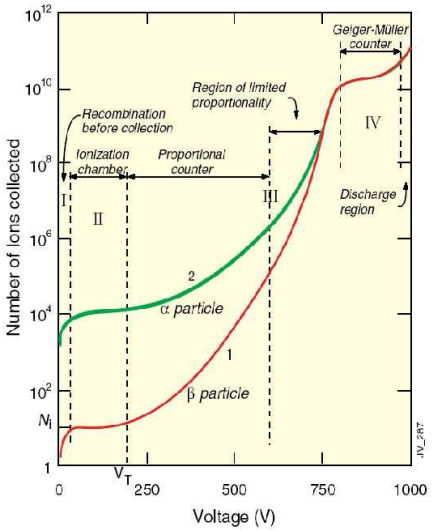

Figure 3.1: Charge collection in a single wire gas chamber versus the applied voltage; the various regimes are described in the text [31].

making used of transistorised electronics, each wire could be equipped with its own amplifier integrated onto the chamber frame: a practical detector for position measurements is so formed. A MWPC consists in a plane of equally spaced anode wires centred between two cathode planes, Fig. 3.2. In such a device, apart from the region very close to the anode wires, the field configuration is like in a planar parallel plate capacitor, the equipotential surfaces are parallel to the planes and the electric field is uniform. Close to each anode wire, the equipontential surfaces are cylindrical, the field is highly non uniform and it increases approaching the wire surface with a hyperbolic behaviour. The electrons and the ions liberated in the constant field region when an ionising particle crosses the detector drift toward the nearest anode wire (electrons) and towards the nearest cathode plane (ions). The electrons, when they reach the high field region, are accelerated and an avalanche is produced. The movement through the electric field of the positive ions liberated in the multiplication process induces a negative signal on the anode wire and, correspondingly a positive one on the cathode electrodes.

Early in the development of the MWPC, it was realised that the spatial information could also be obtained by measuring the drift time of the

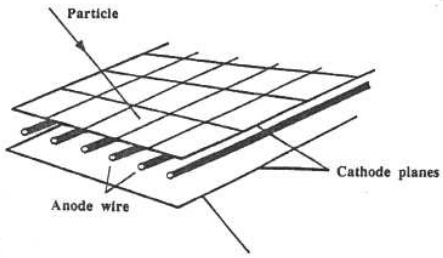

Figure 3.2: Sketch of the MWPC [32].

electrons produced in an ionising event: this is the working principle of the Drift Chamber (DC). An example of DC structure is shown in Fig. 3.3. The anode wires are alternated to cathode wires and the distance between them is pretty large (some cm). The non-uniformity of the field is often cured interleaving field wires between the anode wires. The DCs [33] can be grouped in three types according to their geometrical design: the first type consists in a sensitive area placed across the path of a particle in order to measure one, or perhaps both, coordinates of the point of penetration. The second and the third kind consists in a sensitive volume where the electrons produced along a long portion of the particle trajectory are collected on several sense wires: several coordinates are measured along the track. An example of the second type is an arrangement of a large number of parallel or almost parallel sense wires which span the sensitive volume, usually interleaved with equally parallel field-shaping wires. The third type is characterised by a sensitive volume which is free of wires; the wires are located on one or two surfaces that delimit the drift region. A well-known example of this chamber type are the Time Projection Chambers (TPC), Fig. 3.4. The TPC is a three-dimensional tracking detector measuring many coordinates of a particle track along with information on the specific energy loss of the particle, obtained operating the gas detector in proportional mode. The detector is a large gas-filled vessel, typically cylindrical, with a thin high voltage electrode at the centre. When the voltage is applied, a uniform electric field direct along the cylinder axis is created. Often a magnetic field is also applied, so that, it is possible to measure the particle momenta from the reconstructed curved trajectories.

The ends of the cylinder are covered by arrays of proportional anode wires coupled to a cathode segmented in strips or in pads. When a charged particle crosses the cylinder volume and produces free electrons, they drift towards the end-caps where they are detected by the anode wires as in a MWPC. One coordinate is provided by the position of the firing anode wire while the second one is obtained from the signal induced on the cathode readout elements. Using a centre-of-gravity method, the position of the avalanche along the fired wire is obtained. The third coordinate, along the cylinder axis, is given by the drift time of the electrons. The long drift distance and the diffusion, particularly in the transversal directions, can disturb the reconstruction. The application of a magnetic field confines the electrons to helical trajectories along the drift direction reducing the diffusion. During the TPC standard operation the limiting factor is the accumulation of space charge in the drift volume due to the positive ions from the avalanches drifting back towards the central cathode. To prevent the distortion of the electric field in the drift volume, a grid is placed just in front of the anode wires; it is set at a potential adequate to capture there the positive ions from the avalanche, so preventing them from drifting back into the sensitive volume. Since the charge collected at the end-caps is proportional to the energy loss of the particle, the signal amplitudes from the anode also provide information on the particle energy loss.

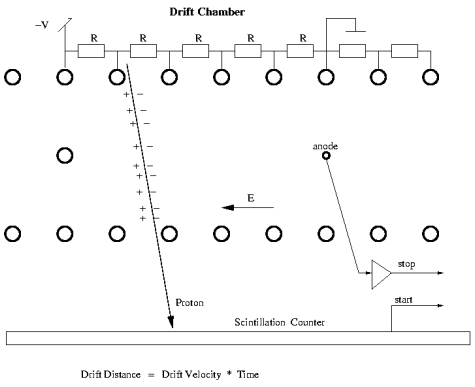

Figure 3.3: Sketch with the working principle of the Drift Chamber [34].

Another type of gas detectors has been exploited, mainly for triggering purposes. The Resistive Plate Chamber (RPC), developed in the early Eight-

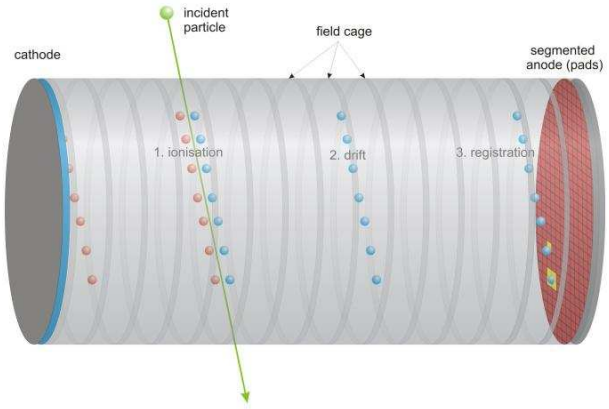

Figure 3.4: Scheme of a TPC [35].

ies [36], consists of two parallel plates, made out of a phenolic resin (Bakelite) with a high bulk resistivity of ($10^{10} \div 10^{12}$ Ωcm), separated by a few mm of gas. The external Bakelite surface is coated with a conductive graphite paint and the two plates form the high voltage and ground electrodes, respectively. The readout is performed by means of aluminium strips separated from the graphite coating by an insulating PolyEthylene Terephthalate (PET) film as shown in Fig. 3.5. The RPC can operate in streamer mode, i.e. the electric field inside the gap is kept high enough to generate limited streamer discharges localised near the crossing place of the ionising particle, entailing a moderate rate capability ($\sim$100 Hz/cm^2), or in avalanche mode, i.e. the electric field over the gap and thus the gas gain are reduced yet affording robust signal amplification at the front-end level. This allows improving by about an order of magnitude the rate capability ($\sim$1 kHz/cm^2) [37]. The RPCs are still largely used in several experiments. I would like to mention that the Large Hadron Collider (LHC) experiments as ATLAS, CMS and ALICE are currently using RPCs for triggering purposes. In ALICE, glass RPCs are used for time-of-flight measurements. The fine time resolution, up to 1 ns for the Multi-gap RPCs (MRPCs) [39], allows to tag the time of the ionising event in less the 25 ns, namely between two bunches crossing.

More and more often, in high energy physics experiments, large surfaces have to be instrumented. The affordable solution, in terms of costs, is offered by the gaseous detectors. Since the future experiments demand improve-

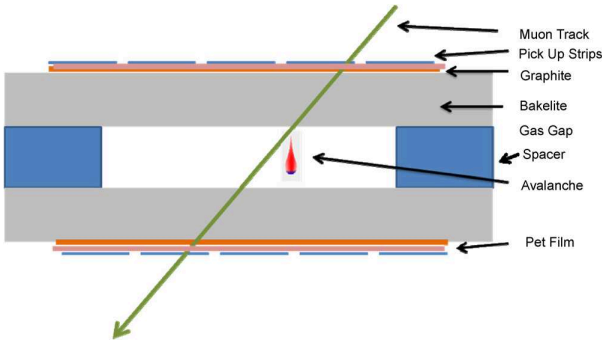

Figure 3.5: Scheme of an RPC [37].

ments in space and time resolution, several efforts are currently made towards more performing gaseous detectors. Modern photo-lithographic technology has enabled a series of inventions of novel MicroPattern Gaseous Detector (MPGD) concepts: the Micro-Strip Gas Chamber (MSGC), the MICRO MEsh GAseous Structure (MICROMEGAS), the GEM and several others. The MSGC, a concept invented in 1988 by A. Oed [38] is the first of the MPGD. Consisting in a set of tiny metal strips laid on a thin insulating substrate, and alternately connected as anodes and cathodes, the MSGC turned out to be easily damaged by discharges induced by heavily ionising particles destroying the fragile electrode structure. The more powerful GEM and MICROMEGAS concepts fulfil the needs of high-luminosity experiments with increased reliability in harsh radiation environments. By using smaller cell size compared to classical gas counters, these detectors offer intrinsic high rate capability, excellent spatial resolution and a single photoelectron time resolution in the 10 ns range. GEM are presented in great detail in the next sections. MICROMEGAS were invented in 1996 [40] and they consist of a thin metal grid stretched at very small distance, 50÷100 μm, above a readout electrode; a second drift electrode is placed further (Fig. 3.6). A very high field is present across the gap between the readout electrode and the grid, typically above 30 kV/cm. Here the electrons released in the upper drift region, namely the region between the drift electrode and the grid, are collected and multiplied. Regularly spaced supports (insulating fibres or pillars) guarantee the uniformity of the gap, at the expense of a small,

localised loss of efficiency. This device exploits the saturating characteristics of the Townsed coefficient at very high field to reduce the dependence of the gain on the gap variations, thus improving the uniformity and stability of the response over a large area. Due to the small gap and the high field, the positive ions are collected very quickly, mostly at the cathode mesh; this prevents space-charge accumulation and induces very fast signals, with a 50÷100 ns duration. Moreover the MICROMEGAS stands high particles flux and the space resolution is typically of a few hundred μm. This gaseous detector was used for the first time in the COMPASS experiment, where the MICROMEGAS planes have an active area of 40×40 cm^2 and they stand a rate up to 450 kHz/cm^2 (Fig. 3.7).

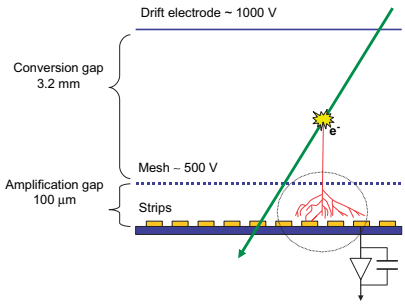

Figure 3.6: Sketch of the operating principle of the MICROMEGAS [48].

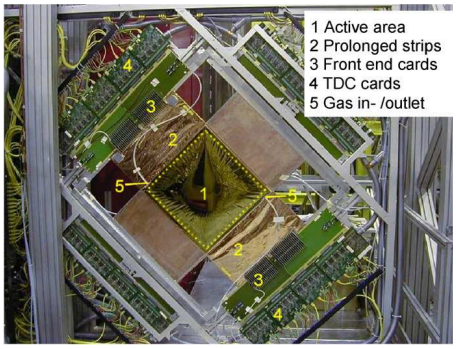

Figure 3.7: Picture of the MICROMEGAS equipped with the readout electronics system, installed at the COMPASS experiment [48].

3.2 The Gas Electron Multiplier (GEM)

The GEM [42] invented by F. Sauli, consists in a thin polymer foil (Kapton[1]), metal-coated on each side, perforated by holes (Fig. 3.8) arranged in a high density hexagonal pattern. Applying a suitable potential between the two sides, each hole acts as an individual proportional counter, multiplying the

[1]Tradename of Du Pont Co., Wilmington, DE, USA

electrons released by the ionising radiation in a gas, which enter the holes. The electrons of the avalanche coming out from the holes can be driven to another GEM foil for further multiplication or be collected by a read-out electrode. In Figs. 3.9 and 3.10, the GEM cross-section is shown. The internal hole diameter is labelled d, the external diameter D, the thickness of the Kapton foil T and the thickness of the copper t. The distance between two hole centres is defined as pitch p. In the GEM standard geometry, the parameters are: t = 5 μm, T = 50 μm, D = 70 μm, d = 50 μm, p = 140 μm.

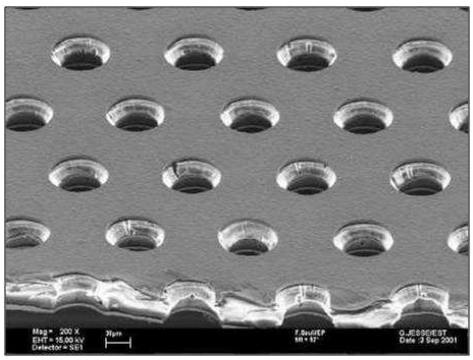

Figure 3.8: Picture of a GEM foil [41].

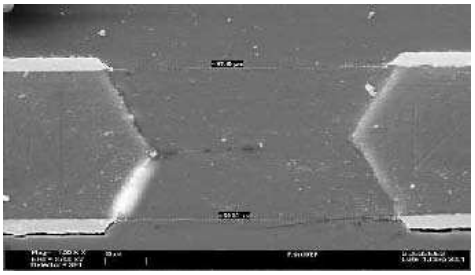

Figure 3.9: Picture of a GEM hole cross-section. The bi-conical profile of the hole is clearly visible [41].

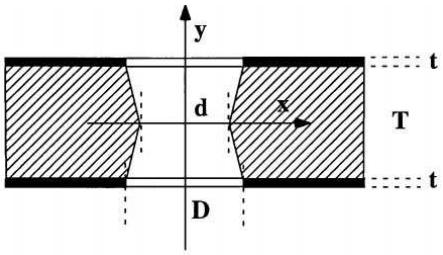

Figure 3.10: Drawing of the GEM cross-section; the geometrical parameters are labelled (reference to the text) [44].

The procedure to obtain a GEM foil is rather delicate. It was invented and optimised at the CERN-EST-DEM workshop[2]. The process starts with

[2]Technology developed by A. Gandi and R. De Oliveira

the production of two identical masks, whose pattern is transferred to the photo-resist foils coated onto the two faces of the metallised Kapton foil, using conventional printed circuit technology, by exposure to the UV light. The precise alignment between the two masks is a crucial parameter, difficult to obtain in particular for large size as 30×30 cm^2. The copper layer is etched according to these masks. Since the patterned copper layer is used as self-mask during the following chemical process of etching through the polymer, any misalignment results in slanted holes; in this case the GEM foils exhibit lower gain and are prone to charge up. The shape of the holes depends on the etching time: double-conical (Fig. 3.9) and cylindrical shapes are obtained for short and long immersion of the foil in the solvent respectively. Then, a second coarser masking and etching removes the conductor around the borders of the useful portion of the GEM foil, leaving offset electrical contact on both sides. A standard passivation treatment employing gold, nickel or chromium can be used to improve the surface smoothness and to protect it from the oxidation. The GEM foils are tested for electrical insulation between the two faces at low voltage in air and at high voltage in dry nitrogen; most show a leakage current below 1 nA at 500V, a threshold value adopted as an acceptance criterion [43]. First the GEMs have been used as booster for other gaseous detectors (for instance MSGC). Stacking two or three GEMs, signals large enough to allow detection are obtained; this is a winning configuration in terms of gain reached and stability respect to discharges. In Fig. 3.11 the scheme of a detector formed using a triple GEM structure is reported. The labelling in the figure is used in the following. The region between the upper electrode, called drift electrode and the top surface of the the first GEM layer is the drift region, where the electrons created by gas ionisation of a charge particle, are driven, due to the electric field present there, into the holes of the first GEM foil. The gaps between the GEM foils are indicated as transfer regions; the transfer field present there allows the electrons coming out from the holes to be led toward the next multiplication stage. The region between the bottom electrode of the last GEM and the readout plane where the signal is created, is the induction region. The resistors chain is used to power the GEM electrodes: it preserves a fixed difference of poten-

tial among the electrodes even during a discharge reducing electrical stresses. The discharge can damage seriously the front-end electronics; segmenting the electrode of the GEM foil limits the amount of charge in a discharge protecting the front-end electronics. This basic detector design is currently used in many GEM detectors operating in running experiments (Sec. 3.4). Among the favourable features of the GEMs, there are the close geometry of the detector and the separation between the multiplication region and the readout plane. This latter aspect offers large freedom in choosing the geometry of the readout elements. Another advantage is the high rate capability due to the high density of holes which allows spreading the charge. The GEM signal is characterised by the fast movement of the electrons almost without contribution from the ion tail. The ions created during the multiplication are collected on the top GEM electrode. The signal generated on the bottom face of the GEM nearest to the readout electrode can be used as signal for a self-triggering system.

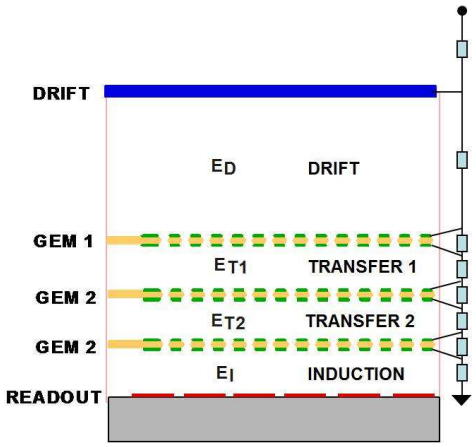

Figure 3.11: Schematic drawing of a triple GEM detectors with segmented readout and a resistors chain to power it [41].

3.3 The GEM characteristics

The GEM detector have been characterised detecting soft X-rays and charged particles, in laboratory and in beam conditions [44]. Several parameters con-

tribute to the optimisation of the GEM performance. Geometrical parameters affect the maximum gain attainable, the collection efficiency and the optical transparency. The applied fields play a role in the electron transparency, in the maximum gain reachable and in the time stability. The electron transparency refers to the amount of primary charge produced by ionisation, which is driven into the holes, while the optical transparency refers to the geometry of the detector. A brief overview about all these properties is reported. First, the characteristics of a single GEM structure are presented, so that the following characterisation of multilayers architectures results clearer.

The ratio between the number of electrons from the multiplication process and the electrons entering into the holes defines the *gain* of the detector. Actually it is not possible to collect at the anode all electrons without losses; it is usual to call *effective gain* of the detector the gain, which is estimated from the anode signal amplitude. The gain and the effective gain depend on the hole diameter, on the voltage and the external fields applied, and on the gas mixture. In this section, the gas mixture considered is Ar/CO_2 (70:30). In Fig. 3.12 an example of the effective gain attainable for a single layer detector at constant radiation flux is shown. Although the maximum gain is affected by the rate, no saturation effect at high gain have been found for rate $<10^5$ mm^2 s^{-1} demonstrating no space charge phenomena: GEMs are high rate devices.

The gain variation versus the hole diameter is reported in Fig. 3.13. The gain is obtained measuring the currents in all the electrodes. At fixed voltages, the gain decreases with the hole diameter because the intensity of the electric field inside the hole decreases. The effective gain decreases for diameter values higher than 70 μm while for smaller ones it is stable. This is due to the fact that, for small hole diameters, the gain reduction increasing the diameter size is compensated by a smaller fraction of electrons collected at the GEM bottom face. The difference between the gain and the effective gain is so pronounced because the induction field applied is not sufficient to collect more than 30% of the electrons at the anode electrode. Increasing the induction field, the amplitude of the anode signal I_S is linearly enhanced

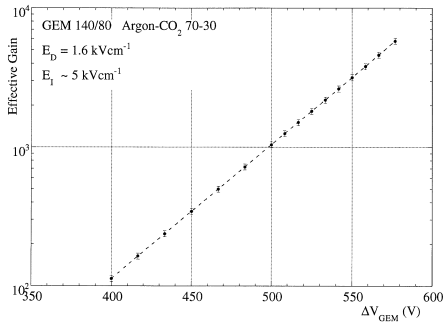

Figure 3.12: Effective gain versus voltage in operating conditions [44].

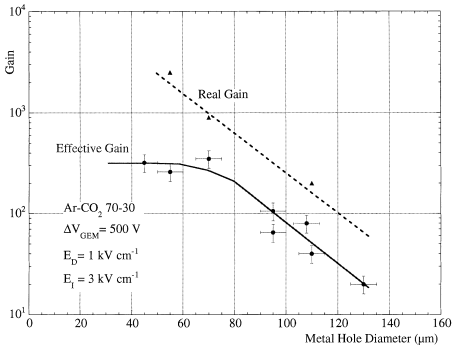

Figure 3.13: Effective and real gain versus the hole diameters [44].

while the current at the bottom GEM electrode I_B decreases (Fig. 3.14). The sum of the two currents, I_{TOT}=I_S+I_B, which represents the gain (dashed line in Fig. 3.14), is affected by the induction field leaking into the holes. The positive current sharing between the top GEM I_T , and the drift electrode I_D depends on the drift field strength. For the standard gas mixture used, applying 8kV/cm in the induction region, the parallel plate multiplication begins, the gain increases and in the bottom GEM electrode a positive current due to the ions appears and overtakes the electron current. This condition is unsafe because a discharge may propagate to the readout electrode. Furthermore the signals detected at the anode develop a characteristic ion tail.

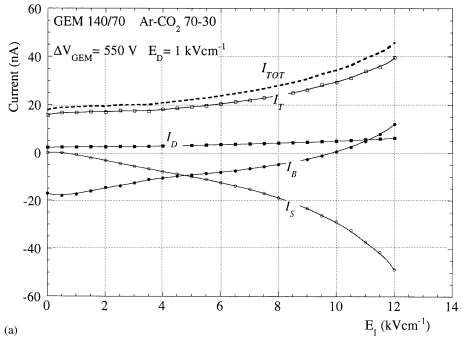

Figure 3.14: Current sharing between electrodes in a single GEM detector, versus the induction field [44].

Ratio P/D	Optical transparency: τ
140/50	0.12
90/60	0.4
140/100	0.46

Table 3.1: Variation of the optical transparency versus the ratio between the pitch and the outer diameter of the GEM holes.

In Fig. 3.15 the variation of the all currents at the electrodes of the GEM detector versus the drift field are reported. The detector is uniformly irradiated. In this plot I_{TOT} indicates the sum of the positive ion currents measured on the top and on the drift GEM electrodes. For a given geometry, the drift field range of efficient electron collection depends on the GEM voltage (Fig. 3.16), but it is almost independent from the induction field. Variations of the GEM geometry can extend the electron transparency (Fig. 3.17 and Table 3.1).

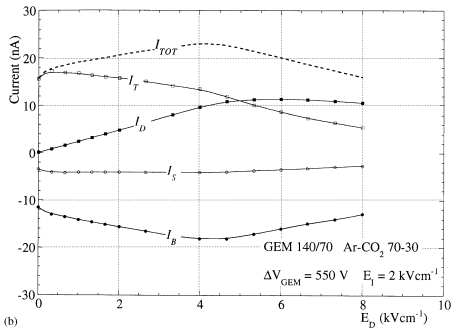

Figure 3.15: Current sharing between electrodes versus the drift field. The X-ray irradiation rate was kept constant at about 10^4 mm^{-2}s^{-1} [44].

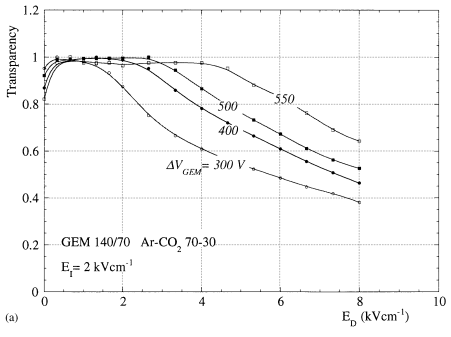

Figure 3.16: Electron collection efficiency (transparency) versus the drift field, for several values of the GEM voltage. The curves are normalised to unity under the implicit assumption of full electron transparency in the plateau region [44].

The fractional ion feedback, defined as the ratio of the drift current to the total current, increases with the drift field and depends on the GEM

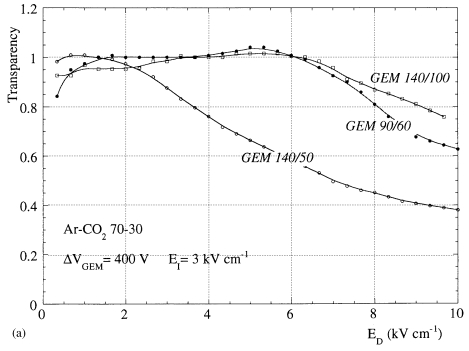

Figure 3.17: Electron collection efficiency (transparency) versus the drift field for three GEMs with different geometry; for each geometry the GEM pitch and external hole diameter is given [44].

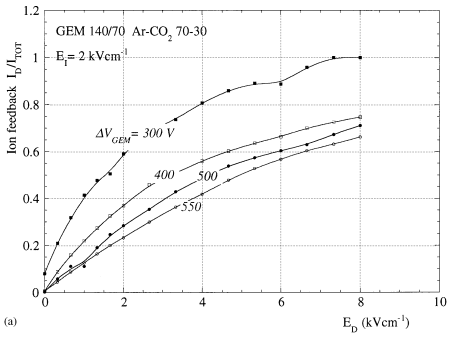

Figure 3.18: Ions feedback ratio versus the drift field for several GEMs voltages [44].

voltage (Fig. 3.18). A more substantial suppression of the ion feedback can be obtained with multiple structures. As discussed in the previous section, the assembly in cascade of two GEM electrodes at close distance permits to reach very high gains and extends the range of the charge tolerable before discharging, a performance exploited to achieve the detection of minimum ionising particles in presence of heavily ionising tracks. The gain of a double structure is, with good approximation, a product of the effective gains of the two elements, obtained at similar values of the external fields, as shown in Fig. 3.19. Furthermore the effective gain is also almost invariant from the sharing of the voltage between the two GEMs, as far as their sum is constant.

Of course, in estimating gains and currents sharing in multilayer structures, one has to take into account that the transfer field for the first GEM is the drift field for the second one, therefore constraining the operation. An example of the currents sharing among the electrodes varying the drift, induction and transfer fields are shown in Figs. 3.20 - 3.21, Figs. 3.22 - 3.23 and Figs. 3.24 - 3.25 respectively. In the table 3.2 the labels of the various currents at the electrodes are listed. The sum of the voltages is constant and the gain is roughly the same. In all cases, the algebraic sum of the currents is close to zero, demonstrating the self-consistency of the measurements. While

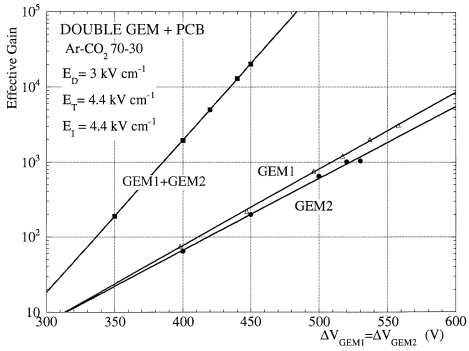

Figure 3.19: Effective gain versus the voltage applied to single and double GEM detectors, operated at similar values of the drift and induction fields [44].

the currents measured at the drift and anode electrodes are solely given by ions and, respectively, by electrons, at the other electrodes the measured value is a composition due to charged particles of both signs.

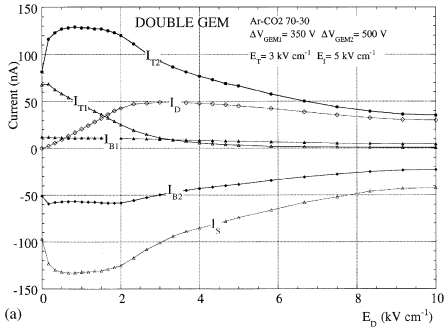

Figure 3.20: Electrode currents in a double GEM detector versus the drift field; GEM voltages: 350 V and 500 V respectively [44].

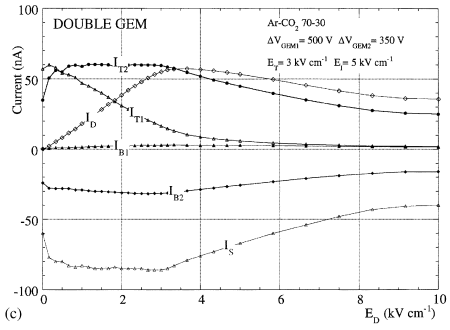

Figure 3.21: Electrode currents in a double GEM detector versus the drift field; GEM voltages: 500 V and 350 V respectively [44].

From the scans reported above, we can infer once more that the dependence of the signal I_s from the induction and transfer fields is almost invariant with the voltage sharing between the two GEMs, at constant sum; this is not the case for the dependence on the drift field, as expected considering the modification of the drift plateau varying the GEM voltage discussed above. As expected, a longer drift plateau is obtained for a higher GEM1 voltage.

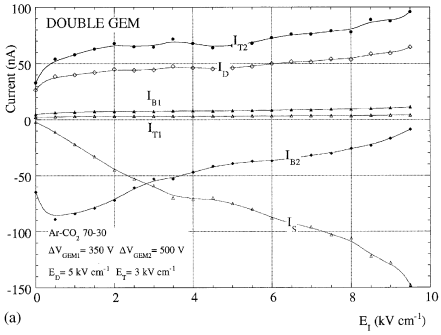

Figure 3.22: Electrode currents in a double GEM detector versus the induction field; GEM voltages: 350 V and 500 V respectively [44].

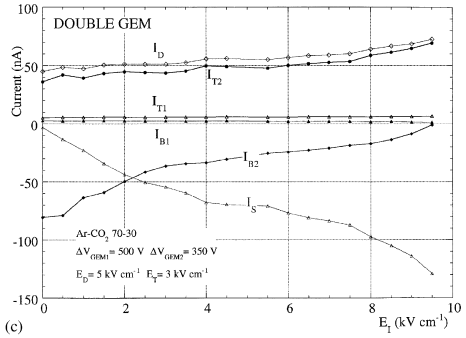

Figure 3.23: Electrode currents in a double GEM detector versus the induction field; GEM voltages: 500 V and 350 V respectively [44].

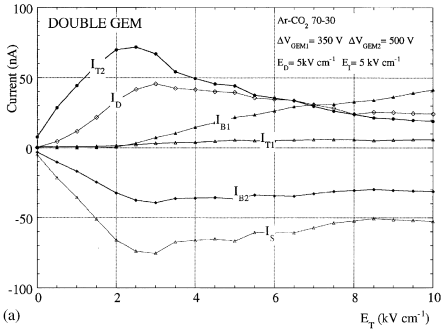

Figure 3.24: Electrode currents in a double GEM detector versus the transfer field; GEM voltages: 350 V and 500 V respectively [44].

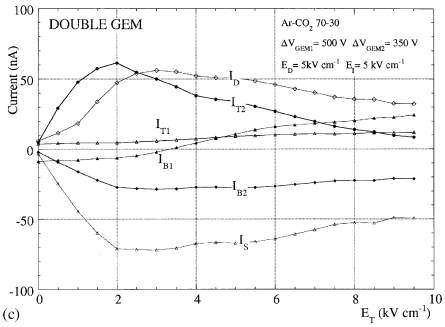

Figure 3.25: Electrode currents in a double GEM detector versus the transfer field; GEM voltages: 500 V and 350 V respectively [44].

Label	Corresponding electrode
I_D	drift
I_{T1}	top GEM 1
I_{B1}	bottom GEM 1
I_{T2}	top GEM 2
I_{B2}	bottom GEM 2
I_S	anode

Table 3.2: Correspondence between currents labelling and electrodes.

An important aspect of the charge transmission through a GEM detector concerns the amount of the positive ions feedback in the transfer and in the drift regions. In Fig. 3.26 a zoomed view of the ions feedback in the low drift field region is compared with the electron collection efficiency measured with the same setup, at the smaller value of the voltage applied on the first GEM (350 V). It is remarkable that at the minimum value of the drift field providing a good transfer of electrons (around 250 V/cm), the ions feedback fraction is only 2%. A low ions feedback is a big issue not only for photon detection applications (Sec. 3.5), but also for the read-out of large drift volumes in a TPC (Sec. 3.4).

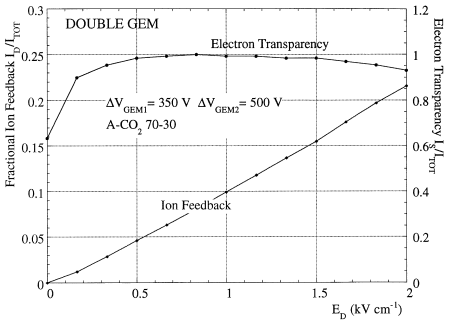

Figure 3.26: The fraction of ions feedback and the electron transparency measured in a double GEM detector versus the drift field [44].

In the context of the brief overview of the experimental studies performed, it is important to mention the studies dedicated to the discharges rate. It was observed that when the detectors operate at gains of about a few thousands and they are exposed to high radiation fluxes, or there is a release of a large amount of charge in the sensitive volume, a breakdown of the gas rigidity may occur. The sequence of events leading to a discharge is initiated when the avalanche size (product of the ionisation and the gain) exceeds a few 10^7 ion-electrons pairs, the so-called Reather's limit. The local field modifications is then large enough to induce a transition of the avalanche to a forward-backward propagating streamer. In the wire chambers the receding streamer is stopped by the decrease of the field far from the wires; this is the mechanism of the limited streamer regime. Owing to the small distances,

in the MPGDs, the streamers become breakdowns causing serious damages. Since the GEM readout plane is electrically separated from the multiplying electrodes and as far as a GEM discharge doesn't propagate all the way to the anode, the breakdown is often just a large but non-destructive signal. Several systematic studies have been carried out [45] and here we report about the main outcomes. First of all the discharge probability is defined as the ratio between the observed frequency of breakdowns and the source rate. To simulate the real running conditions with heavily ionising tracks as in an experiment, an alpha particles emitter, as ^{220}Rn (6.4 MeV) is added to the gas flow of the detector. The method has the advantage of uniformly exposing the sensitive volume of the detector. In Fig. 3.27 the discharge probability is shown as function of effective total gain in single, double and triple GEM detectors exposed to the alpha particle source. For this measurement, the voltage applied to each multiplier was identical (equal gain sharing) and the maximum gain is increased by about an order of magnitude at each structure added. The statistical significance of the zero baseline corresponds to the observation of no discharges during a waiting time of 3000s, or a probability of less than 6×10^{-6}. The maximum gain and discharge probability depend on the charge sharing between the multiplier cascade (Fig. 3.28). The best choice seems to be the asymmetric condition with GEM1 (respectively, GEM3) higher (lower) in voltage by $\sim$10% respect to GEM2.

In parallel to the GEM characterisation studies, calculations of the electric field and simulations of the whole device have been carried out. For field calculations in multi-electrode structures including insulators and to trace the equipotential and fields lines (these latter largely corresponding to the electron drift lines) two interlaced programs have been used: MAXWELL[3], now replaced by ANSYS[4], and GARFIELD [46] [47], respectively. The methods to solve the electromagnetic field configuration are three: the Finite-Difference Method (FDM), the Finite-Element Method (FDM) and the Boundary Element Method (BEM). Since the MPGD geometry is pretty complicated to simulate due to the presence of many electromagnetic singularities, the nearly

[3]MAXWELL, Ansoft Co., Pittsburg, PA, USA
[4]ANSYS, Ansoft Co., Pittsburg, PA, USA, Ansoft Co., Pittsburg, PA, USA

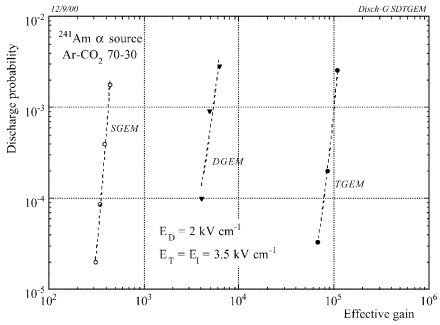

Figure 3.27: Discharge probability versus the total effective gain in a single, double and triple GEM detector [45].

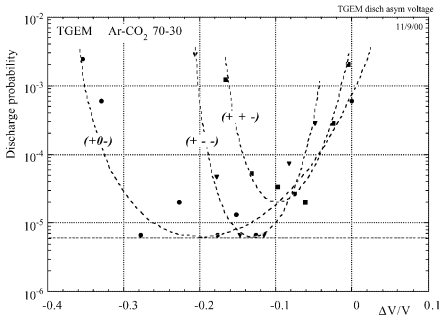

Figure 3.28: Discharge probability in a triple GEM detector versus the asymmetry of the applied voltages; the horizontal scale is the voltage difference between GEM1 and GEM3, divided by the voltage on GEM2; the three curves present equal voltage on GEM1 and GEM2, and lower on GEM3 (indicated as + + -); equal and lower voltage on GEM2 and GEM3 (+ - -) and symmetric offset on GEM1 and GEM3 (+ 0 -) [45].

exact BEM (neBEM) seems more suitable method and investigations in this field are work in progress. Other studies regarding the charges fractions on different detector electrodes (Fig. 3.29) and the estimation of their contributions to the total charges for an accurate estimation of the gain are also in progress. The charging-up is the dynamic physical process contributing to the change of the fields strength at the holes and it is simulated by a heavy iterative process. Nevertheless a simple two-dimensional approach provides the field lines structure in a plane giving a qualitatively idea about the behaviour of the electrons and the ions; Fig. 3.30 is an example of calculation performed taking into account also the magnetic field.

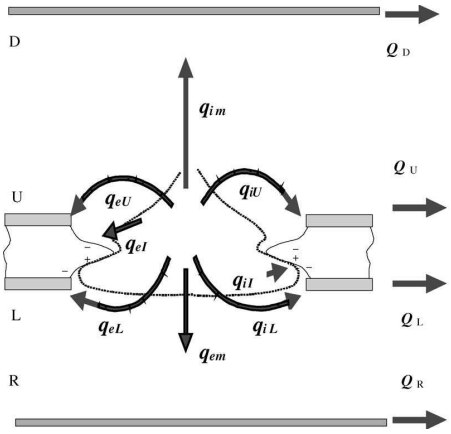

Figure 3.29: Sketch illustrating the distribution of the charge from a multiplication avalanche on the different detector electrodes and the dielectric surface [47].

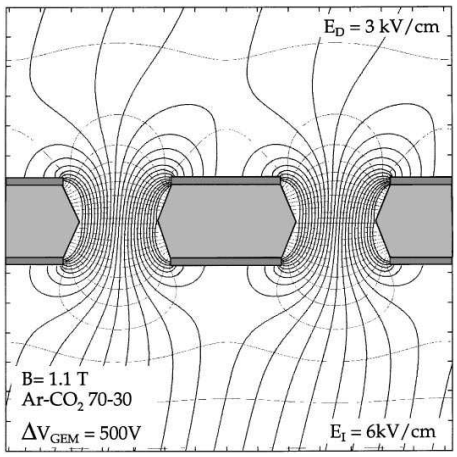

Figure 3.30: Optimised field conditions for the operation of a GEM detector in moderate magnetic field [44].

3.4 GEM-based detectors in experiments

By now the GEM detectors are used in several high energy physics experiments and in the following we present some examples. COMPASS (COmmon Muon and Proton Apparatus for Structure and Spectroscopy) [48] is a two-stage magnetic spectrometer, built for the investigation of the spin structure

of the nucleons and the hadron spectroscopy using high intensity secondary muon and hadron beams at CERN Super Proton Synchrotron (SPS). Operation at high beam rate is required to perform the whole COMPASS physics programme. Thus, the trackers used must be characterised by high rate capability, multi-track resolution capability and radiation hardness, and be equipped with fast, dead-time free readout electronics. Moreover the material budget of the detectors has been kept low in order to reduce the background due to secondary interactions. These requests are fulfilled by GEM detectors and COMPASS is the first experiment in which the GEM technology is used [49]. There are 11 GEM stations along the whole spectrometer, each consisting in two triple GEM detectors mounted back-to-back, rotated by 45° one respect to the other with an active area of 31×31 cm^2 (Fig. 3.31). In the central part of all the stations there is a central zone, 5 cm diameter, which is kept off in standard operation to avoid the detector being overflowed by the primary non-interacting beam. Each detector has two-dimensional Cartesian projective readout strips, 400 μm wide. Since 2008, three more GEM stations have been installed, able to detect particle in the central region, where the beam crosses the detector. The readout structure is modified to allow, in the central region, the effective detection of particle impinging at higher rate: pixelised read-out in the central region and 2-D strip readout in the periphery [50] (Fig. 3.32). The pixel size is 1×1 mm^2, which constitutes a compromise between the spatial resolution achievable and the number of readout channels to be implemented. The active area is reduced to 10×10 cm^2. This detector is called *PixelGEM*.

Specific to the COMPASS GEM detectors are the 2 mm thick spacers between the GEM foils, the foil segmentation pattern and the asymmetric gain sharing among the foils, to guarantee a safer and more stable operation without electrical discharges in the high-intensity particles environment. The detectors operate in an Ar/CO_2 (70:30) gas mixture, chosen for its large drift velocity, low diffusion, non-flammability and non-polymerising properties.

The signal are read out using the APV25 front-end chip [52] and the strips are wire-bonded to the front-end PCB housing three frontend chips. Since this chip lacks proper protection against overcurrents from potential

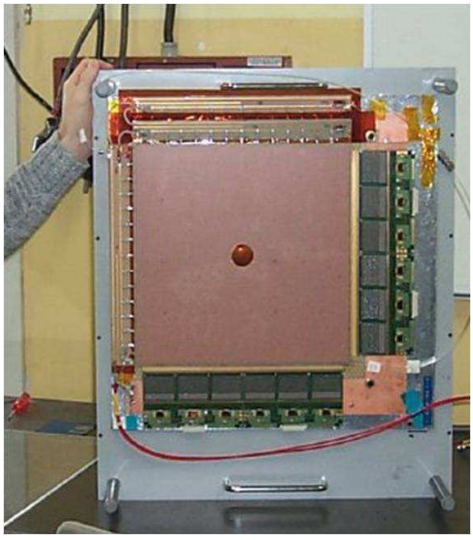

Figure 3.31: A picture of a COMPASS GEM detector equipped with the electronics readout system [51].

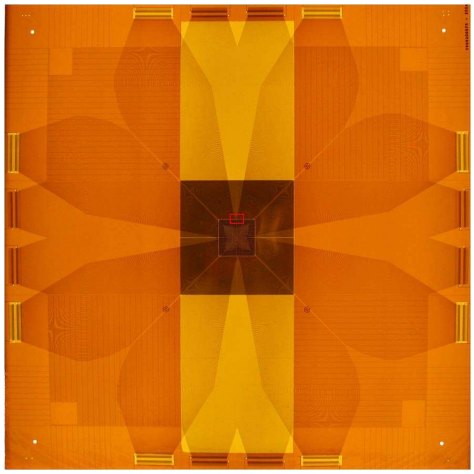

Figure 3.32: Picture of the readout plane of PixelGEM; in transparency the layout of the readout elements (pads and strips) is visible [50].

discharges, an external protection consisting of double-diode and coupled capacitor is added in front of each input channel. The efficiency to detect a particle trajectory in at least one of the two projections is on average 97.2% with variations at percent level among the different detectors. An offline algorithm combines hits from adjacent strips to yield an improved value for the position of a particle trajectory. The spatial resolution is found to be distributed around an average of 70 μm and slightly larger for the PixelGEMs, mostly due to the pile-up of off-time tracks. The time resolution is $\sim$10 ns for both GEM and PixelGEM.

The TOTEM (Total Cross Section, Elastic Scattering and Diffraction Dissociation at the LHC) experiment [53] is designed to measure the total pp cross-section and to study diffractive scattering at the LHC. One of the TOTEM tracking telescopes is equipped with 40 GEM detectors having a semi-circular shape, with a inner radius matching the beam pipe size, Fig. 3.33. The GEM technology has been adopted because of its characteristics: large active area, good position and time resolution, excellent rate capability and radiation hardness. The GEM foils used are the standard ones and the foil stacking is similar to the COMPASS structure. The active area of each detector has an azimuthal coverage of about 192° and a radial extension between 42.5 and 144.5 mm. The two-dimensional readout PCB is characterised by four sectors of 128 strips each and 13 sectors of 120 pads each. The expected spatial resolution for the strips is 100 μm and for the resolution in the azimuthal angle is about 1°.

Another LHC experiment, the Large Hadron Collider beauty (LHC-b) experiment [55], is currently using the GEM technology, Fig. 3.34 [56] exploiting an optimised time resolution. The innermost region of the first muon station of LHC-b is equipped with 12 stations each formed by two triple-GEM detectors with pad readout. This technology has been selected because of the low material budget, space constraints, rate capability and radiation hardness requirements. Since the time performance is a specific issue of the experiment the time resolution has been optimised so that these chambers can contribute to the first level trigger. An extensive R&D activity has allowed to obtain a time resolution of 5 ns using as gas mixture of $Ar/CO_2/CF_4$ (45:15:40)

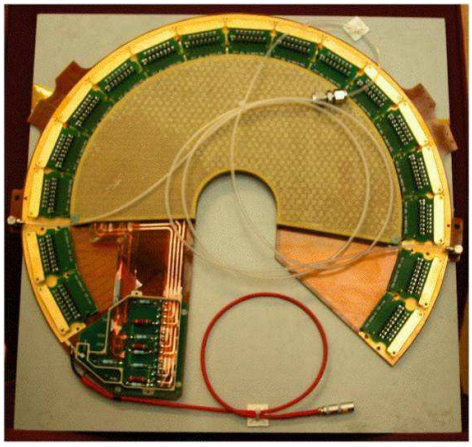

Figure 3.33: One of the 40 triple GEM detectors of used in TOTEM [41].

and slightly modifying the detector geometry: the gaps between the detector layers have been reduced preserving full efficiency of the charge collection in the drift region and the spread of the charge to avoid an increased discharge probability. The GEM foils are standard. The sensitive area of the detector is 20.2×24.2 cm^2. Since the chambers are placed in a very harsh radiation environment and the gas mixture is unusual, an ageing test was performed reproducing the integrated charge of 10 years of running and the results demonstrated that the detectors performance are unchanged.

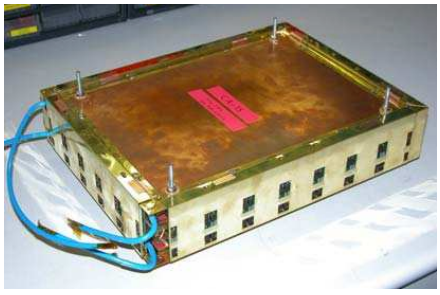

Figure 3.34: An LHC-b GEM chamber fully assembled with the 24 Front-End electronics boards [55].

Other projects involving the MPGD are under the way; we mention some of them very briefly. A TPC is under designing for the International Linear Collider TPC (ILC-TPC) Collaboration [57]. Two options are considered

as gas multiplication device because of their features (negligible E×B track distortions effects, narrow pad response function and intrinsic ions feedback suppression): GEM detectors or MICROMEGAS. For the Pbar ANnihilations at DArmstadt (PANDA) experiment at the Facility for Antiproton and Ion Research (FAIR) at GSI, Darmstadt (Germany) two proposals are considered for the tracking detectors in the solenoid field: straw tubes or a TPC with GEM readout. Employing GEM detectors, it is possible to build an ungated TPC and the ions back-drift into the drift volume can be suppressed [58].

GEM detectors are considered for other fields as fast-neutron detection [59] and medical applications [60]. GEM detectors can also operate at cryogenic temperature in detectors where noble liquid are used, as for coherent neutrino-nucleus scattering [61], solar neutrino experiments [62], dark matter searches [63], Positron Emission Tomography (PET) [64] and digital radiography [65]. The working principle of a cryogenic two-phase detector equipped with GEM readout is sketched in Fig. 3.35. The ionisation produced in the noble liquid by the radiation is extracted from the liquid into the gas phase by an electric field; then it is detected with the help of a multilayer GEM architecture operating at cryogenic temperatures, in the saturated vapour above the liquid phase. It has been demonstrated that a triple-GEM device can detect both the ionisation signal, extracted from the liquid and the scintillation signal, generated in the noble liquid by the particle [66]. The latter is achieved by depositing a thin photoconverter layer of CsI on top of the first GEM (Fig. 3.35). The ionisation signal is used to measure the position and energy while the scintillation signal would provide both the trigger to readout the ionisation signal and the time reference to measure the position in depth, like in TPCs.

3.5 GEM-based photon detectors

The main requests for photon detectors concern the detection efficiency, particularly important when single photons are detected, the localisation accuracy and the time stability. In GEM detectors with CsI photocathode,

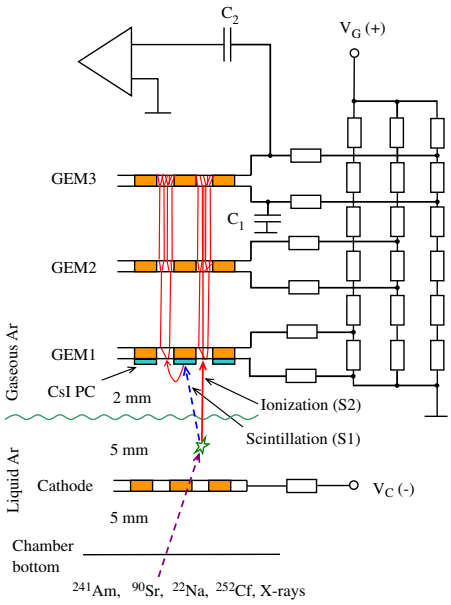

Figure 3.35: Schematic view of the experimental setup to study the performance of a two-phase Ar avalanche detector with CsI photo cathode (not to scale) [66].

thanks to the shadowing effect provided by the GEM itself, the avalanche-induced photon and ions feedback, that spoils the performance and limits the gain and the detector lifetime, has been reduced (Sec. 2.4). In 2004, F. Sauli and collaborators, in view of Cherenkov imaging applications, characterised a triple GEM device with the first multiplier coated with CsI [67]. They used a collimated beam of UV light. The tested detector was a medium-size triple-GEM with 10×10 cm^2 of active area and a projective one-dimensional strip readout. The transfer and induction gaps are 2 mm thick, the drift gap is 3 mm thick; UV photons could reach the central portion of the detector via a fused silica window and a thin mesh drift detector. The UV light source employed was a flash lamp namely a glass vessel containing two close electrodes in a low-pressure hydrogen atmosphere; the electrodes discharge at a certain voltage. A capacitive pickup provides the discharge time used for the measurements in coincidence; a collimator and a set of filters controlled the size and the intensity of the light beam. The detector is powered via a standard resistive divider, with equal potentials across the three GEMs,

and equal fields in the transfer and in the induction region. The drift potential is equal or slightly lower than the one applied to the photocathode. Methane is used as detector gas. Examples of charge distributions in single photoelectron mode are shown in Fig. 3.36. For avalanches generated by a single photon, the space distribution has a FWHM of 600 μm: it is as an indirect proof of the possibility to disentangle two hits about 1 mm apart. The accuracy of the single photon localisation using the distribution of the centre of gravity is about 55 μm (Fig. 3.37).

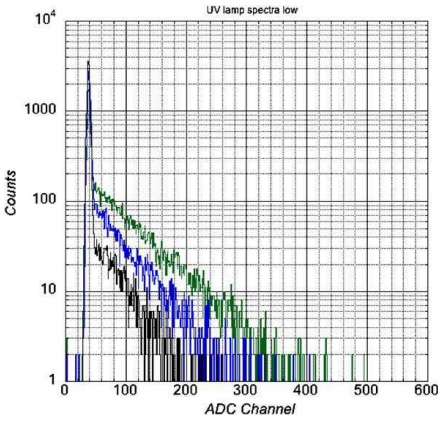

Figure 3.36: Charge distributions in single photoelectron mode [67].

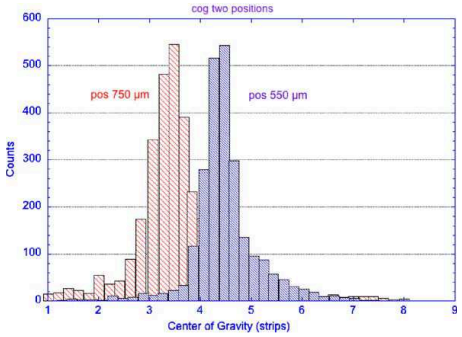

Figure 3.37: Position distributions obtained applying a centre of gravity algorithm, for two different positions of the collimated photon source [67].

For the upgrade the PHENIX experiment at BNL, a threshold Cherenkov counter, the Hadron Blind Detector (HBD) [68][69] (Sec. 2.4) has been developed, using CF_4 as radiator gas. The Cherenkov read-out detectors are triple GEM counters equipped with a CsI photocathode. They are operated in CF_4, the radiator gas itself: no window separates the radiator volume and the photon detectors. The particles cross the GEM detectors and the signal generated by the particle ionisation is superimposed to the photoelectron signals. Nevertheless, the detector is characterised by its insensitivity

to hadron, i.e. by a large hadron rejection factor, while it keeps a high detection efficiency of the photoelectrons. The hadron blindness, namely the insensitivity to the ionisation charge, is obtained by reversing the direction of the drift field, thereby pushing most of the ionisation charges towards the drift electrode. The electron-positron pairs emit UV photons in the radiator by Cherenkov effect and the Cherenkov radiation impinges on the CsI surface producing photoelectrons effectively collected into the GEM holes. Cherenkov photon blobs are detected in the GEM detector pad plane with a pad size dictated by the blob size ($\sim$10 cm^2). This results in a low granularity detector. The charge in the blob can be distributed over at most three pads, thus a primary charge of at least ten photoelectrons per pad is expected, allowing to operate the detector at low gain ($\sim 5\times10^3$) .

Another R&D study is the GEM PhotoMultiplier Tube (GPMT) [70], which consists in a solid photocathode (CsI) coupled to a cascade of GEMs (Fig. 3.38). It can operate at high avalanche multiplication, $10^5 \div 10^6$, with mixtures of pure or almost pure noble gases. It provides short anode pulses, down to $\sim$10 ns, observed in some gas mixtures, and it has a submillimetric spatial resolution. It is insensitive to the magnetic field. At high anode current densities, above 10 pA mm^{-2}, some charging-up effects are reported caused by the ions feedback. Another consequence of the ions feedback is a limitation in the maximum gain attainable. The possibility to operate with noble gas atmospheres, allows studying the extension of the sensitivity to the near-UV-to-visible light range. It is known that the visible-sensitive photocathodes are chemically very reactive and thus vulnerable to gas impurities or outgasing of the detector components, even if the contamination is at the sub-ppm level. A photocathode coating with a thin alkalihalide dielectric films as protection is demonstrated to be operational, but the big drawback is the reduction of the QE of about a factor five, making the device useful only for applications with copious photon yield. Further studies show that bialkali photocathodes are extremely sensitive to the ions feedback due to their very efficient secondary emission; this forces to lower the gain of the first GEM limiting the total GPMT gain and performance. For a particular Ar/CH_4 gas mixture, the ions feedback isn't observed and this effect is

currently under study [71].

Another proposal to couple CsI and GEM, at the moment under characterisation, is the use of resistive electrodes manufactured employing a screen printing technology instead of the metallic one [72]. This implies that the discharge energy in case of sparking is rather small due to the high resistivity of the electrodes. The structure of this new micropattern electrode, called Strip Resistive Electrodes GEM (S-RETGEM) [73], is shown in Fig. 3.39. It is a double-layered micropattern electrode with the inner layer consisting of thin metallic strips and an outer layer including a resistive grid on the top of these metallic strips. Since with one stage and with an appropriate choice of the gas, this device is sensitive to single photoelectrons and it has modest spatial resolution, 1 mm, it is suggested to use it for RICH counters and noble liquid dark matter detectors.

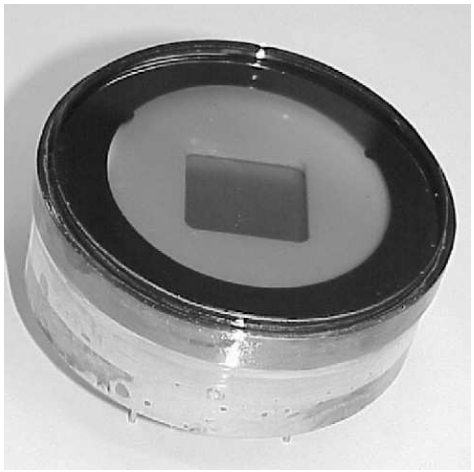

Figure 3.38: Argon-sealed GPMT with semitransparent K-Cs-Sb photocathode and a cascade of GEMs [71].

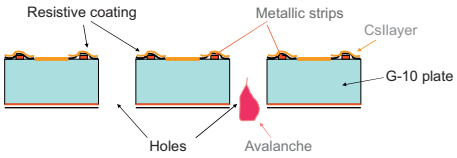

Figure 3.39: A schematic drawing of the cross-section of a photosensitive (CsI coated) S-RETGEM [73].

Chapter 4

A GEM-derived electron multiplier: the THick GEM

4.1 THick Gas Electron Multiplier: THGEM

THGEMs are electron multipliers derived from the GEM design, scaling the geometrical parameters and changing the production technology. The Cu-coated kapton foil of the GEM multipliers is replaced by standard Printed Circuit Boards (PCB) and the holes are produced by drilling. The conical shape of the GEM holes that gives origin to the uncoated polyamide rings around the holes themselves is replaced by a clearance ring, the rim, surrounding the hole and obtained by Cu etching. Typical values of the geometrical parameters are PCB thickness $t = 0.4 \div 1$ mm, hole diameter d ranging between 0.3 and 1 mm, hole pitch p of $0.7 \div 1.2$ mm and rim width between 0 and 0.1 mm (Fig. 4.1).

The THGEM device has been proposed independently by Amos Breskin and his collaborators [74] and Vladimir Peskov [75]. As a result of the initial studies, large gains have been reported for detectors with single or double THGEM layers, as well as good rate capabilities. Other fundamental characteristics of the devices are the intrinsic mechanical stiffness and the robustness against damages produced by electrical discharges. Due to the technology used, it is expected that THGEMs can be produced by industrial processes in large series and large size with standard PCB technology, in spite of the requirement for a large number of holes: some millions per

square meter (Chapter 6). The material budget of THGEM-based detectors is not particularly reduced and they cannot offer space resolution as pushed as GEM-based detectors. These basic characteristics suggest the application fields of the devices. The features of THGEM-based detectors match very well the requirements of photon detectors for Cherenkov imaging applications; the large gain, the robustness, the production technique and the mechanical characteristics are advantages, while the material budget and resolution aspects do not represent a limit. Moreover, thanks to the reduced gaps between the multiplication stages, these detectors can be successfully used in magnetic field. Our studies and this thesis are devoted to this application. THGEM-based detectors can be envisaged also for other applications: they can be used as the active elements in hadron sampling calorimetry [76], muon tracking [77] and readout elements in liquid noble gas detectors [78]; in all these applications, large surfaces have to be instrumented, while space resolution in the mm range is fully adequate.

This chapter is devoted to an overview of the literature dedicated to the THGEM devices to summarise the investigations by various experimental groups.

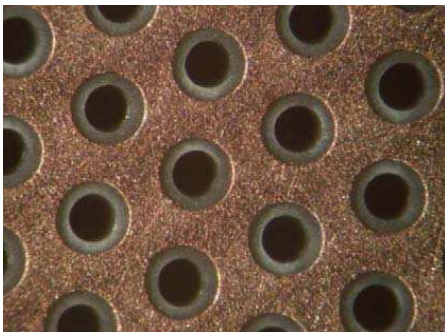

Figure 4.1: Picture of THGEM with d= 0.3 mm, p= 0.7 mm, t= 0.4 mm and rim= 0.1 mm.

4.1.1 THGEM dictionary

A THGEM-based detector is formed by one or more THGEM layers. For each THGEM, we indicate as **top and bottom faces** respectively, the surface at

the hole entrance and hole exit, where entrance and exit refer to the electron path. Above the first THGEM, a **drift electrode**, namely a wire plane or a grid, defines the electric field above the first electron multiplier; the field established in this region is indicated as **drift field**, $\mathbf{E}_{drift}$ and, in general, it points towards the THGEM top surface. When the field is pointing towards the electron drift, this electric configuration is indicated as reversed field. The voltage applied between the two THGEM faces is called dipole field, ΔV_{THGEM}. The field present in the THGEM holes is called E_{hole}. The field between two THGEM layers is called **transfer field**, $\mathbf{E}_{trans}$. The field between the bottom face of the last THGEM and the anode electrode is the **induction field**, $\mathbf{E}_{ind}$. In the standard detector configuration, the read-out element is the anode itself. As anticipated in the previous section, the THGEM geometrical parameters are referred to as **t** (**PCB thickness**), **p** (**hole pitch**), **d** (**hole diameter**) and **rim** (**the clearance ring around the hole**). When a **photocathode** is present, two possible schemes can be implemented: the **SemiTransparent** (**ST**) and the **Reflective** (**Ref**) ones: in the ST case, the photoconverter layer is place above the THGEM layers and it is obtained coating with a CsI film an UV transparent window; in the Ref configuration, the CsI film is deposited on the top surface of the first THGEM layer.

4.2 MAXWELL and GARFIELD simulations

The MAXWELL[1] and GARFIELD [79] software packages have been used to simulate the response of single and double THGEM detector in order to complement the information coming from the experimental data, both at atmospheric pressure [80] and low pressure [81]. In particular, MAXWELL is used for electric-field calculations, while GARFIELD simulates the electron-transportation and the avalanche development. Configurations with or without a photoconverter layer have been studied. In the following we summarise the main indications obtained from the simulations at atmospheric pressure.

In Fig. 4.2 a GARFIELD simulation illustrating the THGEM operation

[1]MAXWELL 3D, ANSOFT Co. Pittsburg, PA, USA.

principle is shown. The simulations indicate that, **even at low THGEM gain** ($\sim$ 30), **the electrons** produced by an ionising particle in the gas ionisation process or from a photon conversion at the photocathode layer (ST or Ref configuration) and guided towards the THGEM by a suitable electric field E_{drift}, **are focused into the holes by the dipole field obtained polarising the two THGEM faces**. Here they are multiplied thanks to the field into the hole. Depending on the direction of the E_{trans}, the electric field present between the first THGEM multiplier and either a second multiplier or a read-out plane, the avalanche electrons are transferred to the second multiplier or the readout electrode, or collected at the THGEM bottom electrode, as depicted in Fig. 4.2 where a reversed E_{trans} is present.

In Fig. 4.3 the comparison between the field inside the hole for a standard GEM at $\Delta V = 0.5$ kV and a THGEM at a difference of potential $\Delta V = 2$ kV, in Ar/CO_2 (70:30) gas mixture, is presented. The voltages applied represent in both cases the maximum voltage that can be applied preserving stable operation. The z axis is direct along the THGEM thickness and the zero of the axis is the centre of the hole. For the THGEM, MAXWELL calculation shows high field values, greater than 15 kV, already outside of the hole, indicating that the **avalanche extends out of hole**. Further calculations [82] reported a well confined avalanche within the hole for lower voltage applied to the THGEM (ΔV=1.3 kV). A similar effect of overflowing avalanche from the hole is not standard for GEM operation; nevertheless, it was noticed operating a GEM multiplier in noble gases [83].

The simulation studies indicate that **the THGEM geometry affects directly the field inside the hole**. Figure 4.4 presents a MAXWELL calculation of E_{hole} versus the hole diameter for fixed thickness (0.4 mm) and at fixed voltage (2 kV).

Another insight into the THGEM operation mechanism, in particular important for multiple THGEM configurations, is reported in Fig. 4.5: **the field near the edge of the hole is modified by the transfer field** and, of course, this modification affects the multiplier gain. The effect is expected to be more significant at higher ΔV_{THGEM} values, where the avalanche further extends out of the hole.

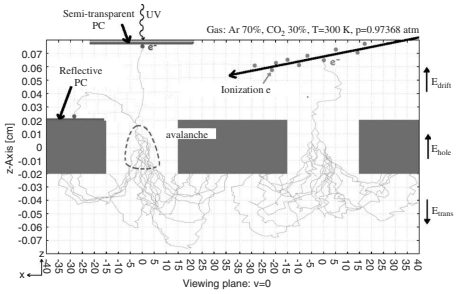

Figure 4.2: The THGEM operation principle demonstrated by GARFIELD simulation [80].

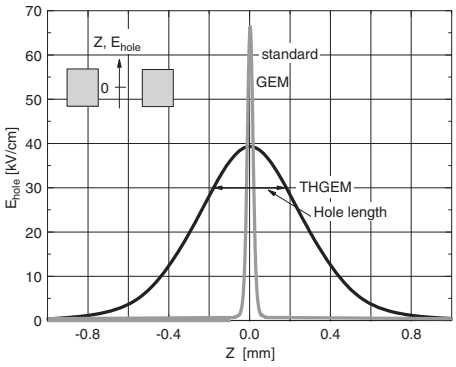

Figure 4.3: E_{hole}, the electric field along the central hole axis, calculated by MAXWELL, in a standard GEM and in a THGEM (d= 0.3 mm, pitch= 0.7 mm, t= 0.4 mm, rim= 0.1 mm) for maximal operation voltage in Ar/CO_2 (70:30) (details in the text) [80].

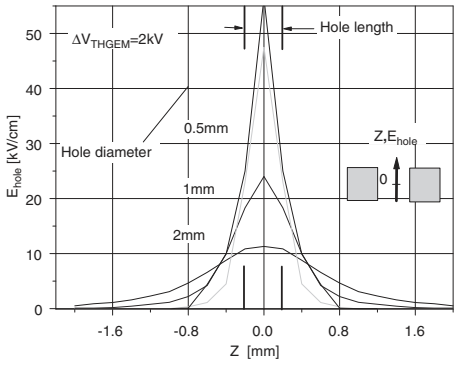

Figure 4.4: The electric field strength along the central hole axis, calculated by MAXWELL, for a fixed THGEM thickness, t=0.4 mm and and applied voltage, 2 kV and different hole diameters [80].

The electric field at the surface of the THGEM along the line interconnecting two adjacent hole centres, for various ΔV_{THGEM} is shown in Fig. 4.6, for a THGEM with geometrical parameters: d= 0.3 mm, p= 0.7mm, t= 0.4 mm and rim= 0.1 mm . For $\Delta V_{THGEM} > 800V$ the field exceeds 3 kV/cm all over the surface. This relatively high electric field is important for photon detection applications in Ref configuration: in fact, it allows an efficient extraction of the photoelectrons [84].

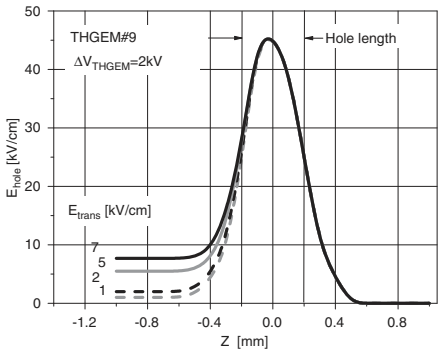

Figure 4.5: The effect of E_{trans} on the E_{hole} along the hole axis, calculated by MAWXELL [80].

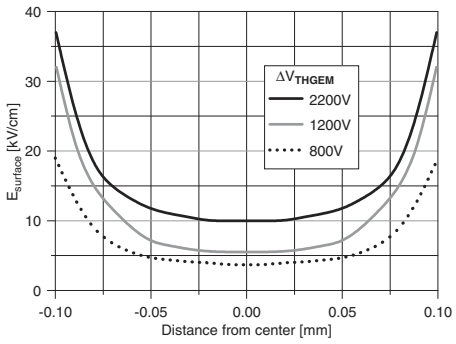

Figure 4.6: Maxwell calculation of the electric field $E_{surface}$ at the THGEM top surface along the line interconnecting two hole centres; THGEM geometry: d=0.3 mm, pitch=0.7 mm, t=0.4 mm, rim=0.1 mm [80].

Concluding this section, it is important to give the general status of the simulation studies of THGEM devices. Even if the simulation exercises are relevant to guide the interpretation of the experimental data and to suggest an appropriate path for the laboratory work, they provide mainly relative indications. For THGEMs, the limits of this approach are related to two sources of difficulties. The first one is related to the strong relevance that the microscopic details of the electric field have in describing correctly the multiplication process. When the field exhibits major changes within small zones, as it is the case at the edges of a THGEM hole, a detailed description of the field is intrinsically imperfect using finite element calculations. In fact, a different mathematical approach based on solving boundary integral equa-

tions [85] has been proposed and, in the next future, the proper interfaces to use it in synergy with GARFIELD will become available [86]. A second complication is due to the presence of a dielectric surface, in particular the rim surface, but also the hole internal surface. This feature imposes to include in the simulation the charge (ions and electrons) deposited on these surfaces. In principle, iterative exercises accompanied by phenomenological input, allow to determine realistically the amount of the deposited charge [87], but the calculation procedure is so heavy to result unpractical for repeated exercises. To a large extent, several of these comments apply also to the simulation studies of GEM devices and other micropattern gas detectors.

4.3 Experimental results

4.3.1 Methodology: THGEM characterisation

The following quantities have to be measured to characterise the THGEM performance:

- The *effective gain*: it is the product of the absolute gain obtained in the holes and the Electron Transfer Efficiency (ETE) (defined below). In case of multilayer architectures, the effective gain represents the product of the absolute gains in all the THGEM layers, the ETE above the first THGEM, and the ETEs in all the intermediate layers. The effective gain does or doesn't include the charge transfer efficiency to the readout anode, according to the definition by the different authors.

- The *rate capability*: it is the dependence of the gain versus the event rate.

- The *energy resolution*.

- The *Electron Transfer Efficiency (ETE)*: it is the probability to focus the electron from its creation point into a hole. For an electron produced by gas ionisation, the ETE includes only the transport of the electron, while for a photoelectron emitted from a photocathode, the ETE includes also the extraction efficiency from the photocathode into

the gas, which is a function of the electric field at the photocathode surface. In general, the ETE is a function of the gas mixture and of the electric field.

- The *Ion Back Flow fraction (IBF)*: this parameter is relevant for photon detection applications, and it is the fraction of ions created in the final avalanche that flow back to the photocathode.

4.3.2 Methodology: measurements setup used by the Weizmann group

In this section, the measurement techniques used by the Weizmann group in their THGEM characterisation studies are described [80][81]. The results obtained are summarised in the following section. Except for the energy resolution, which was measured employing an X-ray source, all the other measurements have been carried out with photoelectrons emitted from CsI photocathodes, irradiated with UV light from a continuous Ar(Hg) lamp or from a spontaneously discharging H_2 lamp. The currents from all the electrodes included in the detectors under study were recorded for all measurements. The principle of the measurement of the effective gain is depicted in Fig. 4.7, both for detector configurations with reflective and semitransparent photocathode and for a double THGEM. This measurement is performed in two steps: in the normalisation step (1), no ΔV_{THGEM} is applied between the two faces of the THGEM, so there is no gain and the photocurrent can be determined measuring the current at the THGEM top face; in the gain measurement step (2), a ΔV is applied and the current is measured at the bottom THGEM face, providing the total electrons current collected at the THGEM bottom, thanks to a slightly reversed E_{trans} field that forces all the electrons to the bottom THGEM face.

For ETE measurements before the first multiplication stage, the pulse counting mode is preferred to the current measurements, because this method allows disentangling the effect of the multiplication from the ETE effect. In fact, in case of electron transfer inefficiency, the inefficiency directly translates into a counting rate deficiency. With the setup depicted in Fig. 4.8,

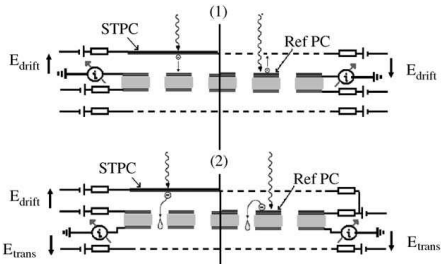

Figure 4.7: Scheme of the setup for the effective gain measurement of a single THGEM, illustrating the two steps of the procedure: (1) normalisation measurement; (2) gain measurement (details are given in the text); left: using an ST configuration; right: using a Ref configuration [81].

the ETE for a Ref photocathode configuration has been measured. Also this measurement is performed in two steps. The first step consists in multiplying and collecting in the MWPC formed by the wire planes M1 and MW_{nor} all the photoelectrons originating on the reflective photocathode. To guarantee a good photoelectron extraction the electric field between the photocathode and the electrode M1 is set at E_{drift}= 3 kV/cm. The full electron transfer through M1 is provided applying a high field, 6 kV/cm, between the M1 and MW_{nor}. No ΔV is applied to the THGEM. In this configuration ETE is assumed to be 1. For the second step, E_{drift} is set to 0 and keeping fixed the total gain of the cascade THGEM and MW_{trans} is set to the same gain previously provided by MW_{nor}, so that the same electronics setting used before can be employed. The photoelectrons originating from the photocathode and then driven into the holes are multiplied through the two stages structure. The ratio of the events rate (n_{trans}/n_{nor}) gives the ETE of the THGEM. The reliability of the measurement is based on the assumption that: the single photoelectron pulse height distribution is exponential, following the Polya relation without saturation, and the multiplication process is not strongly affected by secondary or quenching processes. Therefore, it is important to adjust the total gain in both measurement steps to be identical, by comparing the slopes of the exponential distributions. In Fig. 4.9 an example of the single photoelectron spectra obtained in both measurement steps are reported. The event rates are measured in the selected window, set in the

middle of the pulse height distribution, above the noise and below the tail, to avoid counting secondary or pile-up pulses.

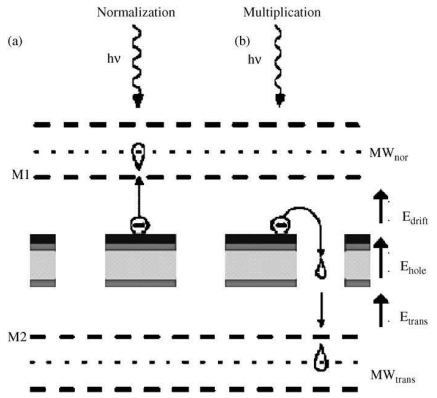

Figure 4.8: Scheme of the experimental setup for the ETE measurement, Ref photocathode configuration (details are given in the text) [80].

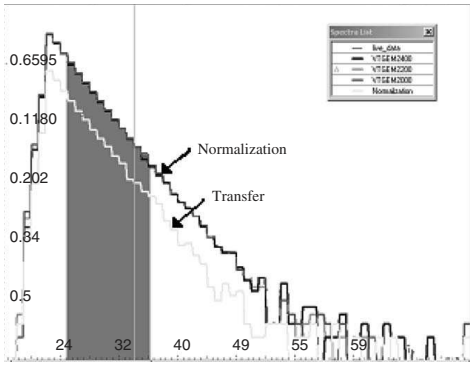

Figure 4.9: Single photoelectron spectra of the normalisation and electron transfer measuring steps, recorded on MW$_{nor}$ and MW$_{trans}$ respectively [80].

4.3.3 THGEM characterisation results obtained by the Weizmann group

A summary of the studies performed concerning the influence of the THGEM geometrical parameters variations and the gas mixtures employed on the THGEM performance is reported [80][81][88][89][90].

First, the experimental results at atmospheric pressure are presented including those with the noble gas mixtures. Then the studies at different pressures are discussed. The detector gain is a fundamental measurement for any kind of application. In Fig. 4.10 the effective gain is plotted as a function of the potential applied to various different THGEM used to detect a UV light. This curve refers to a single THGEM detector; a gas mixture Ar/CH_4 (95:5) is employed; the THGEMs geometrical parameters are listed in Table 4.1. The maximum gain achievable is also shown. In Fig. 4.11 a similar gain plot is shown; it is obtained detecting 5.9 KeV X-rays and using pure Ar; the THGEM geometrical parameters are reported in table 4.2.

THGEM #	Diam (mm)	Pitch (mm)	Thickness (mm)	Rim (mm)
7	0.5	1	0.4	0.1
8	0.5	1	0.8	0.1
9	0.3	0.7	0.4	0.1
11	1	1.5	2.2	0.1

Table 4.1: Geometrical parameters of the THGEMs in Fig. 4.10.

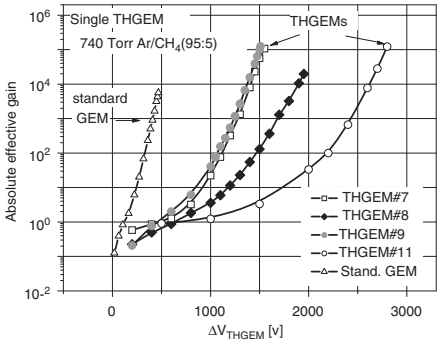

Figure 4.10: Gain measurement versus ΔV_{THGEM} for detectors based on THGEMs with different geometries (Table 4.1); gas mixture: Ar/CH_4 (95:5). UV photons are detected [80].

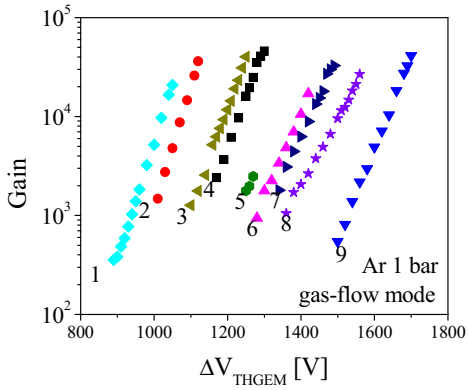

Figure 4.11: Gain measurements versus ΔV_{THGEM} for detectors based on THGEMs with different geometries (Table 4.2); gas used: pure Ar; X-ray from a ^{55}Fe source are detected [89].

Curve #	Diam (mm)	Pitch (mm)	Thickness (mm)	Rim (mm)
1	0.3	0.7	0.4	0.1
2	0.3	0.8	0.4	0.1
3	0.5	0.9	0.4	0.1
4	0.6	1.2	0.4	0.1
5	0.8	1.3	0.4	0.1
6	0.4	0.9	0.8	0.1
7	0.6	1.2	0.8	0.1
8	0.8	1.3	0.8	0.1
9	0.6	1	0.8	0.1

Table 4.2: Geometrical parameters of the THGEMs of Fig. 4.11.

The gain obtained is maximum when the ratio between the THGEM thickness and the hole diameter is ∼1, a result also predicted by the simulations.

Figure 4.12 shows the effective gain measured employing the same THGEM and different gas mixtures in detecting photoelectrons from the conversion of UV photons from an UV light source. As expected considering the gas mixture properties, the same gain values are reached at different voltages for the different gasses. The maximum gain that can be obtained keeping the detectors electrically stable is lower for those gasses that require higher voltages, indicating that there is an overall role played by the voltage applied. In Fig. 4.13 measurements obtained detecting UV photons and soft X-rays with UV light source are compared; the same THGEMs, arranged in single or double structure and operated in a pure Neon atmosphere, is employed. The gain values are pretty similar applying the same voltage, but the maximum gain that can be obtained is higher detecting UV photons; in this case, for each detection event, the initial charge is a single electron, while the initial charge is some hundred electrons when X-rays are measured, indicating that the charge density in the multiplication regions (in the holes and immediately below the holes) is determining the maximum gain obtainable.

Also the rim contributes to the maximum gain attainable; in Fig. 4.14 the gain versus the rim size is shown. The detector is a double THGEM one, with THGEM parameters: d= 0.3 mm, p= 1 mm, t= 0.4 mm and different rim size. The gain clearly increases with the rim size. These data are understood in terms of two effects: an electrostatic effect and a charge density effect. The electrostatic effect is related to the presence and the size of the rim, that increases the distance between the top and bottom THGEM electrodes. The electric field configuration in the hole region is different according to the presence and size of the rim: the multiplication region has different extension and the maximum charge density (Raether's limit) is obtained at different gains.

In Fig. 4.15 the gain response of a single THGEM detector (d=0.3 mm, p=1 mm, t=0.4 mm, rim=0.1 mm) in Ref photocathode configuration versus rate is presented; UV photons are detected; the gas used is with a reflective

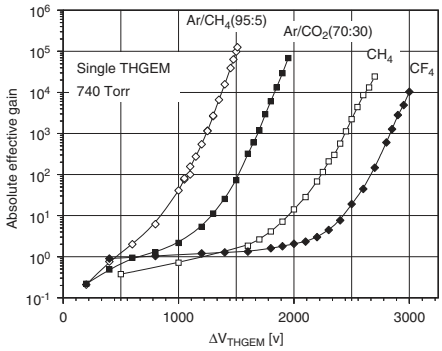

Figure 4.12: Gain measurement for a THGEM (d= 0.5 mm, p= 0.9 mm, t= 0.4 mm, rim= 0.1 mm.) employing different gas mixtures [80].

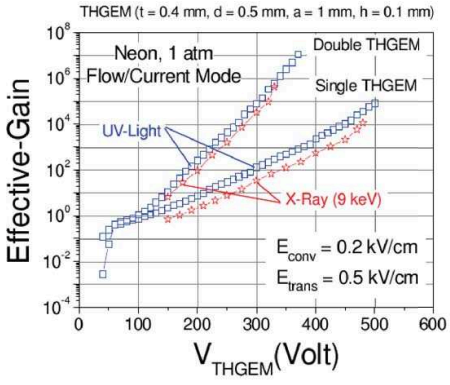

Figure 4.13: Comparison of the gain measurements obtained employing the same THGEMs (d= 0.5 mm, p= 1mm, t= 0.4 mm, rim= 0.1 mm), arranged in single or double structure, detecting UV photons and soft X-rays [88].

PC Ar/CO_2 (70:30); two different voltages are applied. For an effective gain of 2×10^4 at low rates, a gain drop starts only at $\sim10^7$ electron/mm^2 sec. Clearly, THGEM are devices adequate for high rate counting.

An example of the pulse height spectrum with an energy resolution of 18.8% measured using a single THGEM detector (d=0.5 mm, p=0.9 mm, t=0.4, rim=0.1 mm) at a gain of $\sim10^4$ is shown in Fig. 4.16. The energy resolution depends on how well the primary electrons are focused to the THGEM holes; this depends both on the applied voltage and the drift field: their combined effects determine the electron diffusion.

The ETE in the region above the THGEM and its dependence on the THGEM voltage have been studied. Figure 4.17 reports the ETE values for THGEM with geometrical parameters: d= 0.3 mm, p=0.7 mm, t=0.4 mm and rim=0.1 mm and with a Ref photocathode versus ΔV_{THGEM} in various gasses. The drift field above the top THGEM surface, where the photoconverter is deposited, is set to zero. In Fig. 4.18 the ETE measurement, still for the same detector, is shown as a function of the E_{drift} and for a THGEM gain about 10^3 in the gas mixture Ar/CH_4 (95:5). The ETE measurements

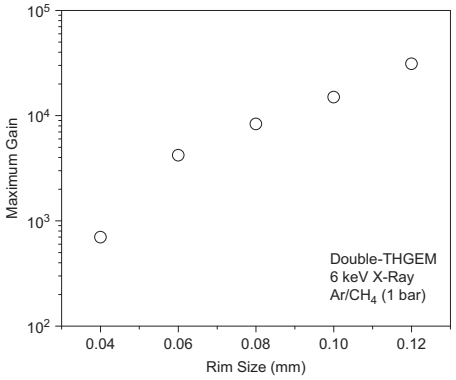

Figure 4.14: Maximum gain attainable for different rim size in a double THGEM detector, with THGEM parameters: d= 0.3 mm, p= 1 mm, t= 0.4 mm and different rim size [81].

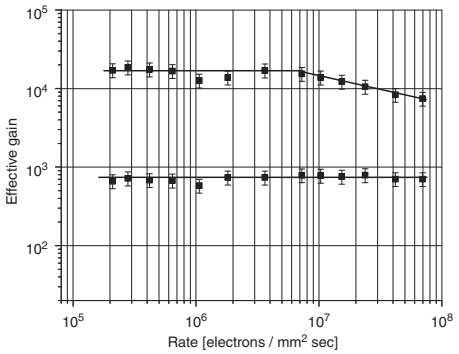

Figure 4.15: Rate capability for a single THGEM (d=0.3 mm, p= 1 mm, t= 0.4 mm, rim=0.1 mm) with a reflective photocathode in Ar/CO_2 (70:30) [80].

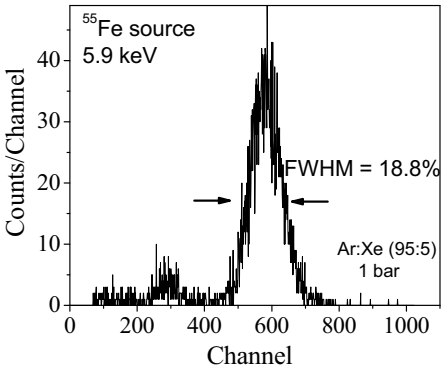

Figure 4.16: Pulse height spectrum for a double THGEM detector in Ar/Xe (95:5) irradiated with ^{55}Fe 5.9 KeV X-rays [89].

require to be complemented with information concerning the photoelectron extraction efficiency, ϵ_{Ex} defined as:

$$\epsilon_{Ex}(E_{drift}) = \frac{I_{gas}(E_{drift})}{I_{vac}} \tag{4.1}$$

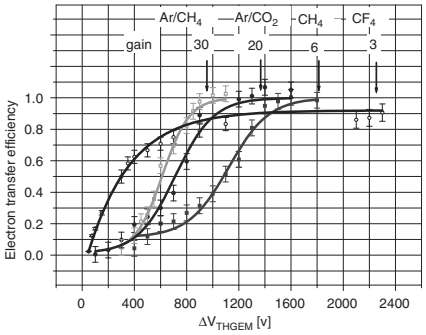

Figure 4.17: Electron Transfer Efficiency versus ΔV_{THGEM} in a Ref photocathode detector, in several gases for a THGEM with geometrical parameters: d= 0.3 mm, p=0.7 mm, t=0.4 mm and rim=0.1 mm [80].

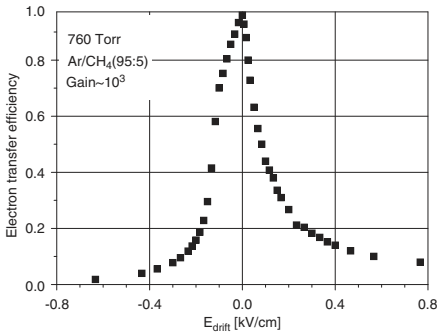

Figure 4.18: ETE measurement for a single THGEM detector with geometrical parameters: d= 0.3 mm, p=0.7 mm, t=0.4 mm and rim=0.1 mm, at gain $\sim 10^3$ in Ar/CH_4 (95:5) as a function of the drift field, E_{drift} [80].

where I_{vac} is the extraction in vacuum, I_{gas} is the extraction in the gas and E_{drift} is the field at the photocathode; Figs. 4.19 and 4.20 shows ϵ_{Ex} as function of the drift field for several gasses. The measurement was performed in parallel plate mode (no voltage applied across the THGEM). The data are normalised to the extraction in vacuum. These data indicate how critical the gas choice is for a photon detector with solid state photocathode.

THGEM-based detectors have been studies not only at atmospheric pressure, but also at low pressures: operating at these pressures is interesting for the development of novel detectors, having high sensitivity to rare events, with low radioactive background, low energy threshold and a large active surface at a low cost. In Fig. 4.21 gain measurements for a THGEM detector (d=1 mm, p=1.5 mm, t=1.6, rim=0.1 mm) with an ST photocathode in isobutane is shown for different gas pressures. The highest gain is obtained around at 10-20 Torr. Figure 4.22 shows similar measurements for single and

double THGEM detectors in isobutane gas coupled to an ST photocathode: the THGEM parameters are different: d= 1 mm, p= 1.5 mm, t= 2.2 mm, rim= 0.1 mm. To get at low pressure, stable detector operation employing the double THGEM structure, the gaps between the single element have been increased. This is required because the multiplication region expands well outside the mere hole region, as the multiplication takes place at much reduced field values.

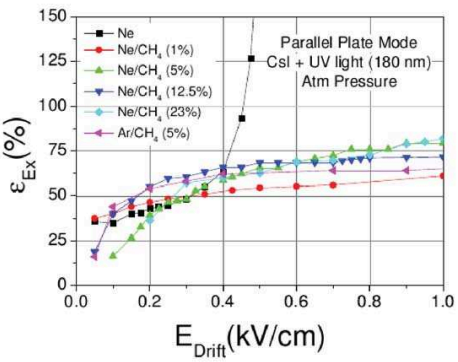

Figure 4.19: Photoelectron extraction efficiency, $\epsilon_{Ex}(E_{drift})$, from the CsI PC, as a function of the drift field [88].

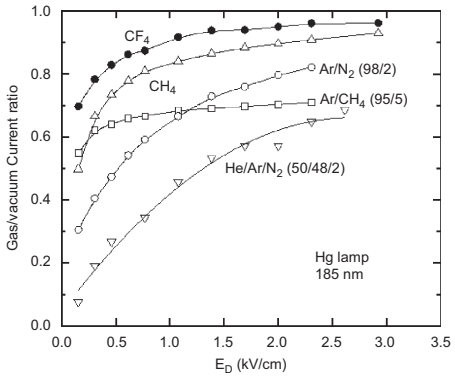

Figure 4.20: Photoelectron collection efficiency measurement for different gasses as a function of drift field, E_{drift} [90] .

Also high pressure studies have been performed. A gain variation scan for a double THGEM detector (d=0.5 mm, p=0.9 mm, t=0.4, rim=0.1 mm) in Ar/Xe (95:5) was performed spanning a pressure range from 0.1 bar to 2 bar (Fig. 4.23). The measurement was done using a 5.9 keV X-ray source. The energy resolution dependence from the pressure is illustrate in Fig. 4.24. The geometry of the detector and the gas mixture used are the same as for Fig. 4.23. The gain of the detector was set to $\sim 10^4$ with E_{drift} = 100 V/cm.

4.3.4 THGEM time resolution

The setup used for assessing the THGEM time resolution [91] consists of a double THGEM architecture, active area 28×28 mm^2, kept under a continuous flow of Ar/CH_4 (95:5), applying a reversed induction field, namely an

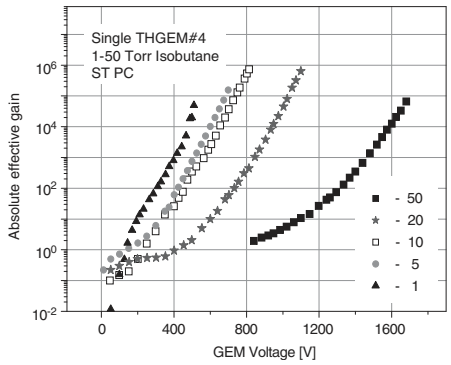

Figure 4.21: Gain versus ΔV_{THGEM} for a THGEM (d=1 mm, p=4 mm, t=1.6 mm, rim=0.1 mm) coupled to a ST photocathode at different isobutane pressure [81].

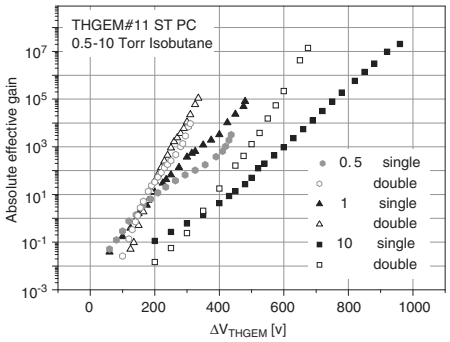

Figure 4.22: Gain measurement for a single and double THGEM detectors (d=1 mm, p=1.5 mm, t=2.2 mm, rim=0.1 mm) coupled to a ST photocathode [81].

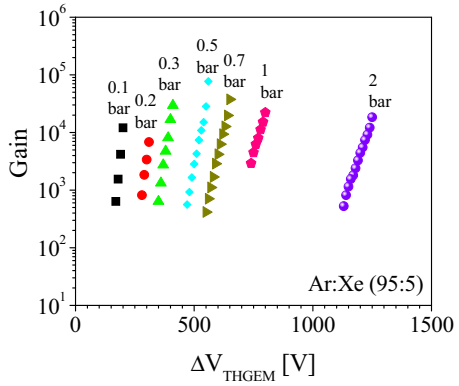

Figure 4.23: Gain versus ΔV_{THGEM} for a double THGEM detector in Ar/Xe(95:5) at different pressures [89].

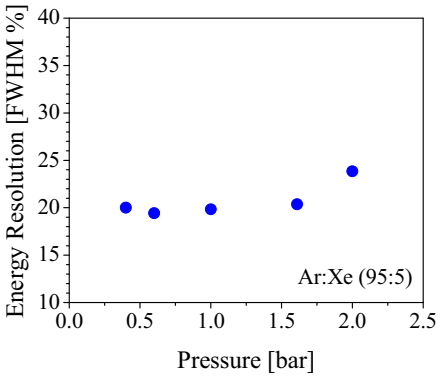

Figure 4.24: Energy resolution versus pressure in a double THGEM detector in Ar/Xe(95:5) with a gain at $\sim 10^4$ [89].

electric field pointing to the bottom face of the second THGEM, so to collect all the electrons there, and reading out the signal of this electrode. The setup is schematically presented in Fig. 4.25 for the Ref photocathode configuration. The ST configuration has been studied with a similar setup, with the ST photocathode placed 3 mm above the first THGEM layer. The UV light source employed is a spontaneously discharging hydrogen lamp; the amount of light is tuned down to the intensity of at most a single photon per pulse inserting absorbers between the lamp and the detector window. The pulse width is ∼2 ns. When several photons per pulse are detected the pulse width has almost no influence on the measured time resolution, because it is always the first detected photoelectron in a pulse that defines the detector timing; when a single photon per pulse is detected, the pulse width represents a time jitter added to the detector resolution.

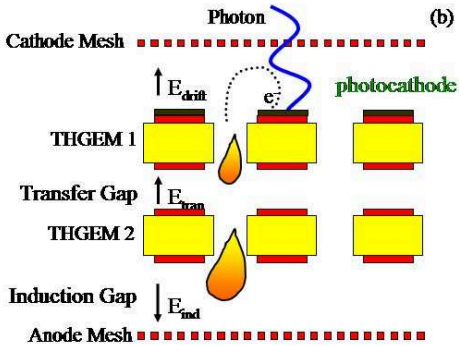

Figure 4.25: Schematic view of the setup used for time resolution measurements, Ref configuration [91].

The experimental results, measured with a detector gain of $\sim 10^4$ are shown in Fig. 4.26 for both the photocathode configurations. The σ-value plotted is the standard deviation of the distribution of the time difference between the detector and the trigger signals. The number of the photoelectrons per pulse is determined from the fit of the pulse height spectrum, making use of the measured exponential pulse height distribution for single photoelectron and keeping the operation conditions of the detector unchanged (Figs. 4.27 and 4.28) [92].

The best time resolution obtained, 0.54 ns r.m.s., has been measured for

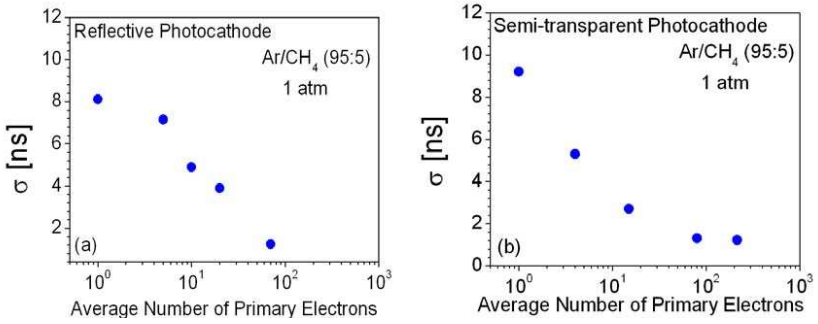

Figure 4.26: Time resolution versus the average number of detected photoelectrons per pulse, measurements obtained with the experimental setup described in the text; (a) Ref photocathode; (b) ST photocathode [91].

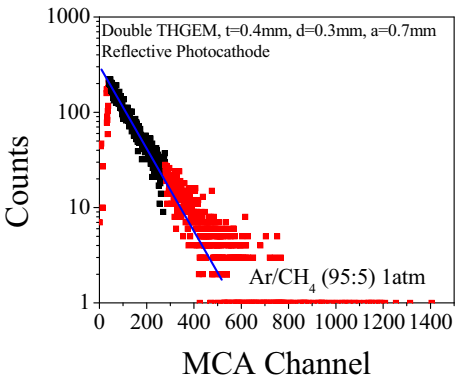

Figure 4.27: Single photoelectron pulse height; the result of the exponential best fit is superimposed. The red data points are excluded from the fitting procedure. The detector gain is set to $\sim 10^4$ [92].

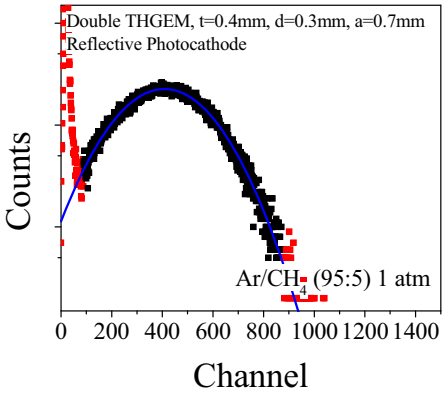

Figure 4.28: Pulse height spectrum for multiple photoelectrons; the result of the Gaussian best fit is superimposed. The red data points are excluded from the fitting procedure [92].

the Ref configuration with 2000 photoelectrons, at a detector gain $\sim 10^3$. In case of the ST photocathode, the variations of the drift field in the region between the photocathode and the first THGEM affect the electron's drift velocity and the diffusion, worsening the time resolution. The relevance of the drift field is demonstrated in Fig. 4.29, where the experimental and calculated time resolution values for single photoelectron versus the drift field applied are reported. Similarly, in Fig. 4.30, the dependence from the transfer field applied between the two THGEM layers is shown: there is practically no dependence in the plotted range (0.5 - 3 kV/cm).

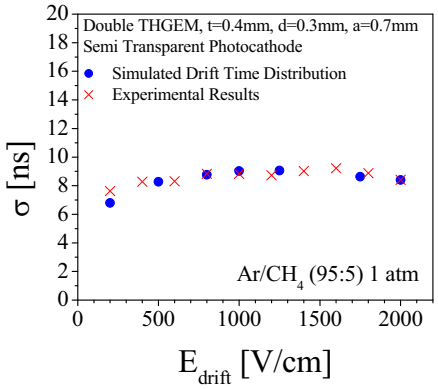

Figure 4.29: Experimental and calculated time resolution values per single photoelectron versus the drift field applied; the detector is described in the text [91].

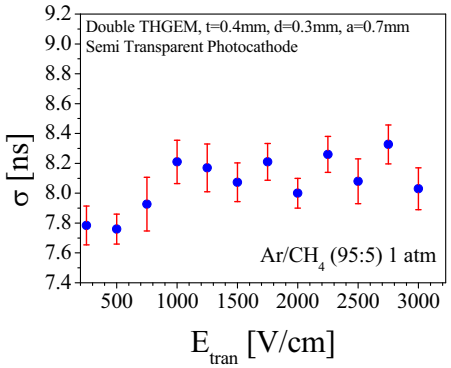

Figure 4.30: Single electron time resolution versus the transfer field applied between the two THGEM layers; the detector is described in the text [92].

The time resolution of the double THGEM was investigated also using a ^{106}Ru source. The trigger was provided by a 4.7 mm thick plastic scintillating counter placed behind the detector; a 1.5 mm thick fiberglass plate was interposed between the THGEM detector and the scintillating counter to select the most energetic electrons in the ^{106}Ru spectrum. Measurements varying the drift and the transfer fields, similar to those performed detecting single photoelectron, were carried out. In spite the fact the β-electrons from the source produce along their path in the conversion gap multiple ionisation electrons, the measured time resolution was of the same order of magnitude as the one measured with single photoelectrons. The results are shown in

Fig. 4.31; the drift field is kept constant at 0.5 kV/cm during the transfer scan while the transfer field is kept at 3 kV/cm during the drift scan.

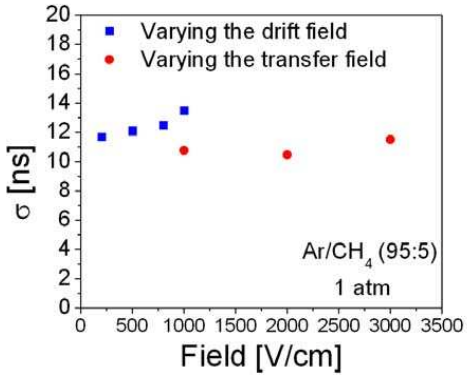

Figure 4.31: Time resolution versus drift and transfer field applied between the two THGEM layers obtained detecting ionising particles from a ^{106}Ru source;the detectors is described in the text [91].

These measurements indicate that the practical time resolution of a THGEM-based detector in around 10 ns, both for the detection of single or a few photoelectrons and for the detection of ionising particles.

4.4 Applications oriented studies

In view of many possible potential applications of THGEM-based imaging detectors, a study has been performed [93] about the localisation properties and quality of imaging with a 2D 10×10 cm^2 multilayers THGEM structure, operating in Ar/CH_4 (95:5) at atmospheric pressure and room temperature. Localisation resolutions of about 0.7 mm (FWHM) have been obtained with soft X-rays. Energy resolution of 21% FWHM for 5.9 keV with a detector gain of 6×10^3 is measured; the gain uniformity is within ∼10% over the sensitive area.

A new THGEM type, application oriented, is the Resistive Electrode Thick GEMs (RETGEM). It can be produced either coating the THGEM electrodes with a resistive layer [94] or replacing the PCB fiberglass with a resistive material [95]. The goal of these developments is the protection of

the detector itself and the associated read-out electronic system against the electrical discharges. The working principle of a RETGEM is the following: when high voltage is applied to the copper frames, running along the perimeter of the active area (Fig. 4.32), the resistive electrodes are charged up to a potential equal to that of the respective copper frames and begin to act as equipotential layers and the electric field configuration is the same as in the case of the THGEM with the metallic electrodes. At low counting rates, the device operates as a conventional THGEM; at high counting rates and in case of discharges, the detector behaviour is more similar to that of a resistive plate chambers. Detailed results concerning the RETGEM performance comparing with the THGEM are reported in [96][97].

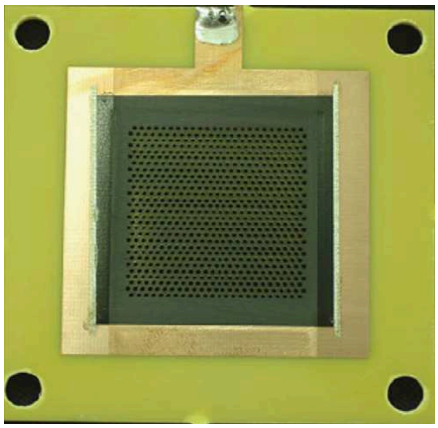

Figure 4.32: Picture of a RETGEM formed by a single resistive layer [94].

As it is the case for GEM-based detectors, the THGEM-based detectors are considered suitable for the detection of UV light and primary electrons produced by recoils in noble liquid detectors for rare event experiments. The operation at cryogenic temperature of the THGEM coated with CsI has been demonstrated by several groups [97].

The gain stability versus time is the main issue for this kind of detectors; in Fig. 4.33, the gain stability for a THGEM made of Kapton and operate in Neon at 77 K versus time is shown.

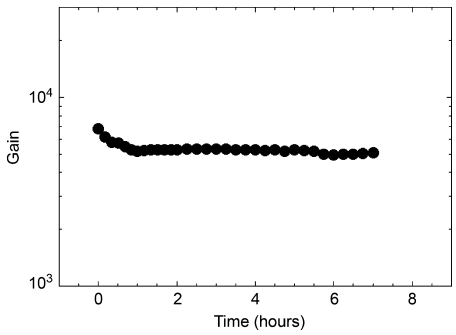

Figure 4.33: Gain stability versus time of a detector formed by a double RETGEM by Kapton in Neon at 77 K [97].

Chapter 5

Setups, instrumentation and tools used for the laboratory studies

5.1 Laboratories

Our systematic studies dedicated to the THGEMs were carried out in a complementary way and in parallel in two laboratories: at the laboratories of the Sezione di Trieste of the Istituto Nazionale di Fisica Nucleare (INFN), in Trieste (Italy) and at the MPGD laboratory at CERN (Switzerland). During my period as Ph.D. student, I spent two years at this latter laboratory. The majority of the studies described in chapters 7, 8 and 9 have been performed at CERN, while the construction of the dedicated instrumentations, the simulation studies and the tests described in chapter 6 have been done at the INFN Trieste laboratory. Some measurements have been repeated in both laboratories in order to cross check the consistency of the measurements using two partially different setups.

5.2 THGEM-based detectors

The THGEMs used for the characterisation studies have an active surface of 30×30 mm^2 and single layer detectors are formed. The sketch of a single THGEM detector is shown in Fig. 5.1. The THGEM is located between the cathode electrode, also called drift electrode, and the anode electrode. For

the characterisation studies, performed detecting soft X-rays, both the anode and the cathode are formed by metallic foils. For light detection, the drift electrode is formed by a wires plane with 2 mm pitch and 50 μm diameter. For specific studies, the anode plane is segmented in pads. Two different pad size are used in our studies: 8 mm×8 mm or 6.2 mm×6.2 mm. For other studies, multilayer architectures have been assembled, as the example shown in Fig. 5.2.

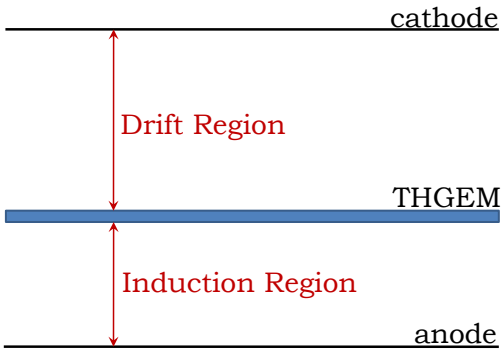

Figure 5.1: Sketch of the single THGEM detector used for the THGEM characterisation studies.

The chamber body is machined from an unique aluminium block, Fig. 5.3. Part of the groove created in order to position the o-ring which guarantees the gas tightness of the chambers is visible in the picture. Particular care is dedicated to the electrical components of the chamber. For the HV connectors, besides gas tightness, it is required that it can operate at least up to 10 kV, that the leak current is well below 1 pA and that there is no charging up effect; connectors LEMO[1] ERA 3S type hermetic sealed connectors have been selected. The electrical cables from the THGEMs to the connectors are carefully insulated, as well as all the welding points inside the detector,

[1] www.lemo.com

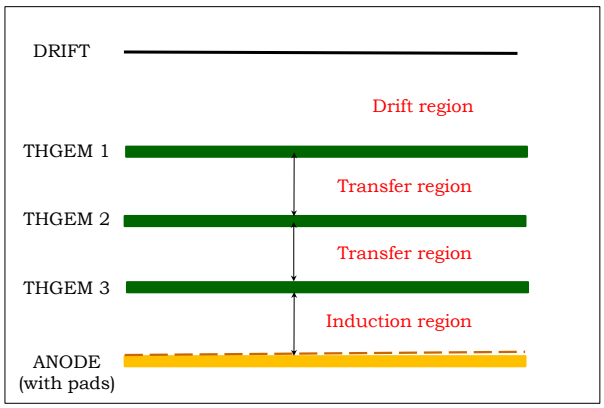

Figure 5.2: Sketch of a three layer THGEM detector.

which are protected by layers of epoxidic glue. Inside the chamber, the spacers between the electrodes are made by nylon or by peek [98]. A window having the same size as the active THGEM area is glued on the chamber cover. Different materials are used for the window: mylar or kapton when soft X-ray are detected and fused silica for light detection, Fig. 5.4.

5.3 X-ray sources

For the THGEM characterisation two soft X-ray sources were used: a ^{55}Fe source (main line at 5.9 KeV X-ray) and an X-ray generator with copper target (main line at 8.9 KeV X-ray). The ^{55}Fe source used has an activity about 185 MBq and the X-rays are collimated so to illuminate either a 2 mm or a 10 mm diameter surface. The X-ray generator is mounted on an optical bench and it can be moved in the transverse plane. The beam intensity can be tuned varying by a factor 100 the filament current. The beam collimation is provided by diaphragms with different diameters; in the majority of our characterisation measurements the collimator used has a 1 mm diameter. In order to attenuate the beam intensity to obtain very low intensities a thin,

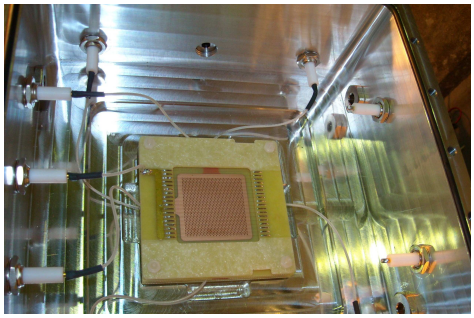

Figure 5.3: Internal view of the detector where 30×30 mm^2 THGEM have been tested. Single or multiple THGEM configuration can be tested inside this chamber.

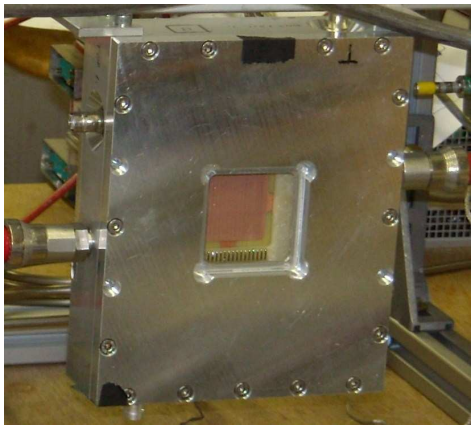

Figure 5.4: External view of the detector where 30×30 mm^2 THGEM have been tested. The cover shown in the picture includes a fused silica window.

100 μm, copper absorber is used; its thickness guarantees that the X-ray spectrum is almost unchanged. The maximum rate used is ∼110 kHz/mm^2.

5.4 Picoammeters

The measurement of the currents driven by all the THGEM detector electrodes is a powerful tool to understand the detector behaviour. The currents range depends on the event rate; anyway our working range is between 10^{-12}A up to 10^{-9}A.

Two kinds of picoammeters are used: a Keithley[2] 6517A and a set of home-made picoammeters. The Keithley 6517A picoammiter has very good current resolution, down to 0.1 pA [99], but it can be used only to read the current of grounded electrodes. Picoammeters that can be connect to electrodes at HV potential are commercially available, but they are pretty expensive and we would need several pieces for our studies. This is way we have developed home-made picoammeters, battery powered, suitable to work up to ∼ 8 kV. The scheme is shown in Fig. 5.5. The feedback resistor

[2]Keithley instrumentation; www.keithley.com

defines the current resolution while the 10 MΩ resistor protects the components from possible THGEMs discharges. The operational amplifier used is a CMOS Operational Amplifier AD 8607[3]. The voltmeter equipped with a four digit digital display is OEM44 made by Anders[4]. The power is provided by four 1.5 V batteries. The batteries, the circuit and the display are supported by structure by peek in order to reduce the leakage currents (Fig. 5.6). The picoammeters are inserted between the power supply channels and the THGEM electrodes. A set of picoammiters arranged in a compact housing is shown in Fig. 5.7. The current values are acquired by imaging acquisition. A dedicated Lumenera photocamera type Lu275 [100] is positioned in front of the picoammeters; a picture is taken every few seconds and stored via an USB connection. A clock is included in the collected picture, so that the current behaviour versus time can be studied. The data are processed off-line via a MATLAB®[5]-based application to perform pattern recognition and numerical data analysis. This image read-out has been selected because other approaches, for example data transfer via optical cables, require important power absorption from the batteries, preventing long (several days) data taking periods.

5.5 Measurements of amplitude spectra

Amplitude spectra have been recorded by two setups. A read-out system is formed by an ORTEC[6] preamplifier model 142, an ORTEC amplifier model 450 and an Analog Digital Converter (ADC) LeCroy[7] mod. 2259, readout by a CAMAC controller model C111 by CAEN[8].

The other setup is composed of a CREMAT[9] CR-111 charge sensitive preamplifier, a CREMAT CR-200 shaping amplifier and the MultiChannel

[3] AD, Analog Devices; www.analog.com
[4] http://www.anders.co.uk/
[5] www.mathworks.com
[6] www.ortec-online.com
[7] www.lecroy.com
[8] www.caen.it
[9] www.cremat.com

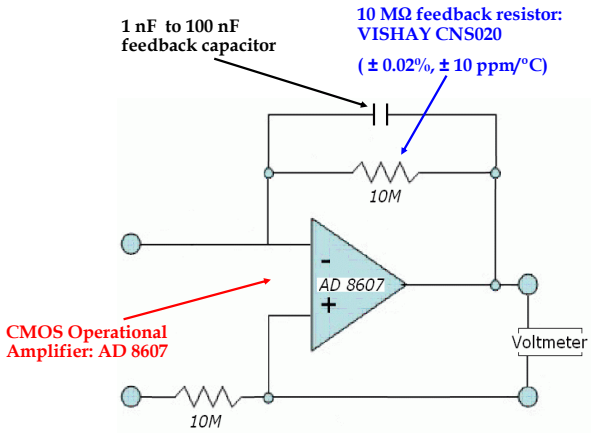

Figure 5.5: Electric scheme of the home-made picoammeters.

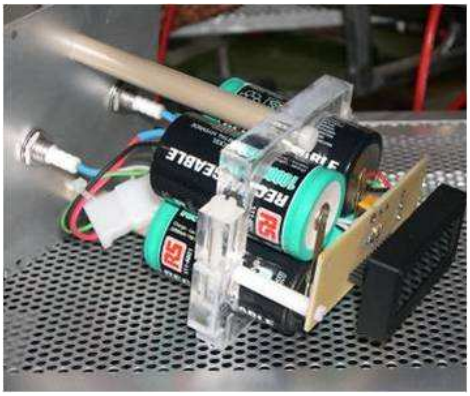

Figure 5.6: Assembly arrangement of the home-made picoammeters; housing removed.

Figure 5.7: Compact arrangement of a set of home-made picoammeters.

Analyser (MCA) model 800A by Amptek[10]. In order to protect the CREMAT preamplifier from the possible discharges in the chamber, a simple circuit was built formed by two diodes in parallel opposite oriented. In general, the signal read-out is the anodic one.

[10] www.amptek.com

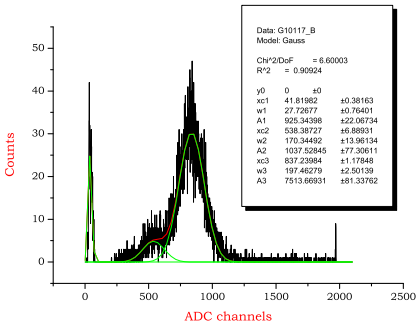

Figure 5.8: Example of a spectrum from a single THGEM detector irradiated by the copper X-ray generator and acquired with the LeCroy ADC.

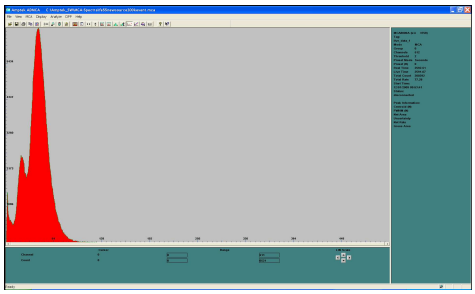

Figure 5.9: Example of the spectrum collected with a double THGEM detector irradiated by the X-rays from a ^{55}Fe source and read-out using the Amptek MCA.

5.6 Digital electronic chain for time resolution measurements

To perform time resolution measurements and to detect Cherenkov light in a test beam, the digital read-out electronics used for the upgrade of the COMPASS RICH-1 detector [101] has been used. Here we summarise its main features. The digital read-out system is based on the MAD4 preamplifier-discriminator [102] and the high resolution dead-time free F1 TDC [103], with 108.3 ps time unit. All read-out electronics are mounted in a very compact setup as close as possible to the detector. The read-out system is free from cable connections to minimise the electrical noise, and to obtain a very robust setup. The system includes the following components (Fig. 5.10): the front-end MAD4 boards, the service Roof boards, the DREISAM read-out boards, the HOT-CMC receiver board, the CATCH boards, the electronics cooling system and the mechanical structure to support the components of the read-out, which also guarantees good electrical contact between the different boards. The front-end MAD4 boards, housing the MAD4 preamplifier-discriminators, are plugged directly into the connectors place at the anode plane rear side.

The Roof boards provide services to the MAD4 boards: power, the DAC

for threshold setting, and input/output data transfer from and to the digital board. The DREISAM read-out boards host eight F1 TDC chips each, for the read-out of the RICH-1 detector. The data transfer between DREISAM boards and CATCH boards is done via two optical links, to avoid ground loops. At the CATCH board, the optical connections are provided by the HOT-CMC mezzanine board. In CATCH boards, the data are formatted and sent via optical S-LINK links to the PCs of the COMPASS data acquisition [48].

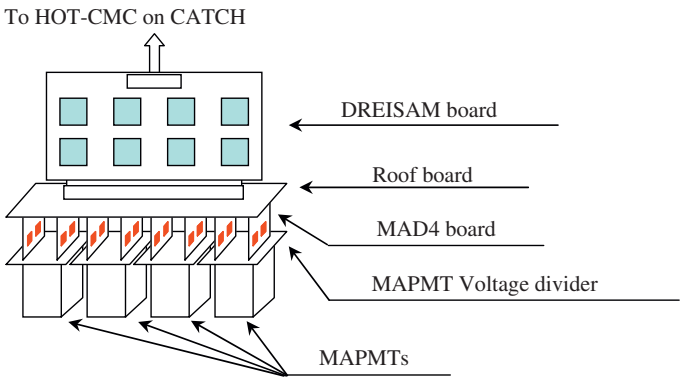

Figure 5.10: Scheme of the readout system.

5.7 UV light sources

For the measurements three different UV light sources are used:

1. a deuterium lamp, the AvaLight-D(H)-S-DUV produced by Avantes[11] working in continuous emission. The lamp is coupled to a fibre ended by an optical collimator in order to obtain a well collimated spot. The spectral output of the lamp is reported in Fig. 5.11: it is cut around

[11] http://www.avantes.com/Chemistry/AvaLight-DH-S-Deuterium-Halogen-Light-Sources/Detailed-product-flyer.html

200 nm by the fibre. The light intensity is fixed, but it can be reduced introducing neutral filters. The attenuation factor is from 0.1 up to 10^{-3}.

2. a UV LED[12] with 255 nm central wavelength and spectrum width of 10 nm, driven both in continuous and pulsed mode (Fig. 5.12);

3. A UV LED PLS 265-10 with 265 nm central wavelength driven by the Pulsed Diode Laser (PDL model 800B) by PicoQuant[13] (Fig. 5.12); the use of this controller makes it possible to have extremely short light pulses with a length of ∼600 ps; the repetition rate can vary between 2.5 and 40 MHz.

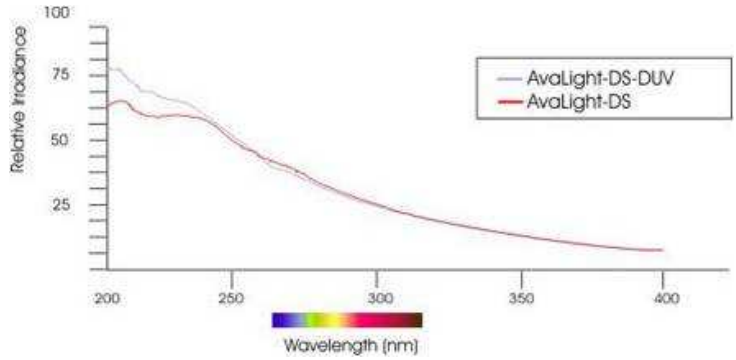

Figure 5.11: Spectrum of the light from the AvaLight-D(H)-S-DUV deuterium lamp coupled to the optical fibre.

The spectra showed in Fig. 5.12 have been obtained using the spectrophotometer AvaSpec-2048[14].

For the pulsed light source, the single photoelectron configuration, namely at most a detected photoelectron per pulse, is obtained tuning the light intensity and checking the amplitude spectra. At low detector gain, an exponential spectrum is expected. If the single photoelectron condition is correctly

[12]Seoul Optodevice Co. Ltd, Seoul Korea (Sud)
[13]PicoQuant GmbH, Berlin Germany
[14]www.avantes.com

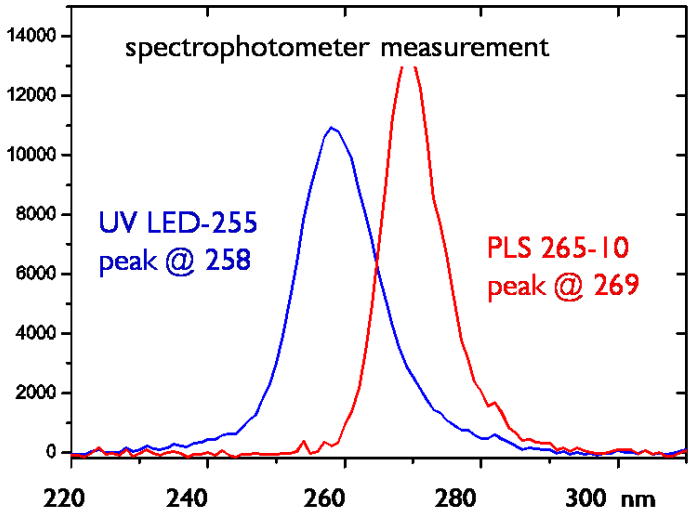

Figure 5.12: LED spectra; the blue curve is obtained for the Seoul Optodevice LED while the red curve corresponds to LED driven by the PDL 800B controller.

established, small variation of the light intensity should provide exponential spectra exhibiting the same slope, even if a different number of entries (Fig. 5.13).

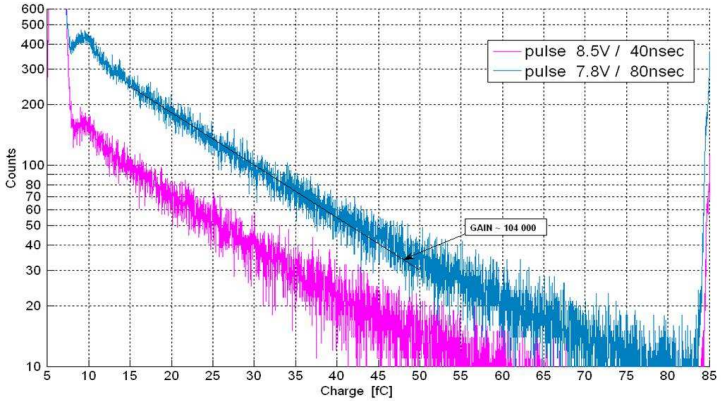

Figure 5.13: Amplitude spectra collected in single photoelectron mode at two two different light intensities.

5.8 Devices for complementary studies

Two additional chamber types were built for specific exercises, namely to perform (i) high voltage studies of various THGEMs and (ii) measurement of the effective CsI quantum efficiency in different gas atmospheres.

Chambers type (i) are shown in Fig. 5.14. These plastic boxes are equipped with two quick connectors for the connection to the gas line and two BNC connectors to apply the the voltage to the THGEM faces. The THGEM is fixed by four nylon screws on four nylon pillars, in order to obtained good insulation and prevent leakage currents.

Chamber (ii), Figs. 5.15 and 5.16, is machined from a unique aluminium block, it is equipped with three quick connectors gas flow and connection to a vacuum pump, and three HV connectors. A fused silica window is arranged on the chamber cover, to let the light from the deuterium lamp, guided via on optical fibre enter the chamber.

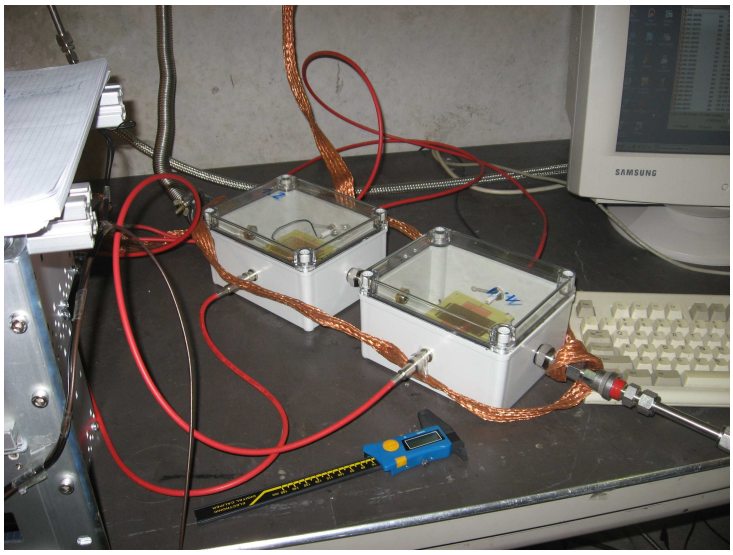

Figure 5.14: Two chambers used to perform THGEM high voltage studies.

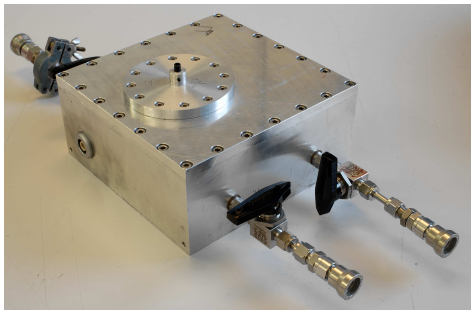

Figure 5.15: External view of the chamber used to measure the effective CsI quantum efficiency in different gas atmospheres.

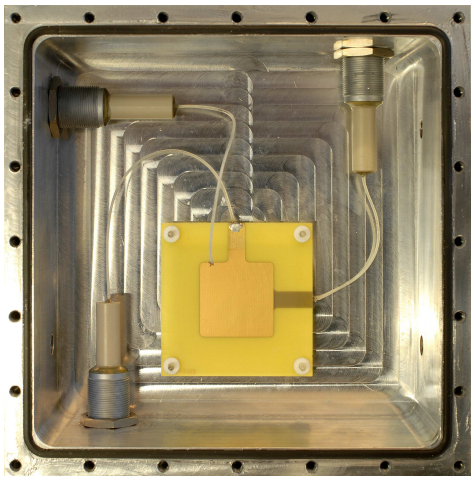

Figure 5.16: Inner view of the chamber shown in Fig. 5.15.

5.9 Test Beam 2009

The setup described in this section has been used for test beam measurements performed in October 2009 (Sec. 9.3). The aim of this test is to study the performance of the THGEM-based photon detector in an experimental environment and to detect Cherenkov photons generated by the beam particle in a fused silica radiator. The setup is pretty complex and compact, Fig. 5.17. Two triple THGEM structures having 30×30 mm^2 and 100×100 mm^2 active surface respectively, are housed in two aluminium chambers. Both chambers are equipped with quartz radiator and the digital read-out system mentioned in Sec. 5.6. The scintillation counters defining the incoming beam and the fused silica radiator have been optically aligned. The chamber, housing the THGEMs 30×30 mm^2, has a trapezoidal cover allowing to illuminate the photocathode either by the UV LED driven by the PDL 800B through a fused silica window, or by the Cherenkov photons generated in the fused silica radiator by the beam particles, Fig. 5.18. Figure 5.19 shows the chamber equipped with the electronic system directly plugged on the anode electrode.

The position of the radiator along the beam axis is adjustable so that different portions of the CsI photocathode present on the THGEM top face can be illuminated by the Cherenkov photons. The HV is supplied to the detector electrodes by a resistive divider.

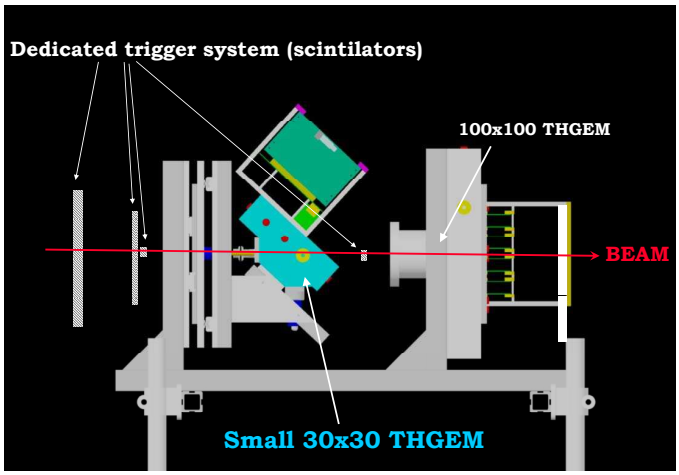

Figure 5.17: CAD drawing of the October 2009 test beam setup.

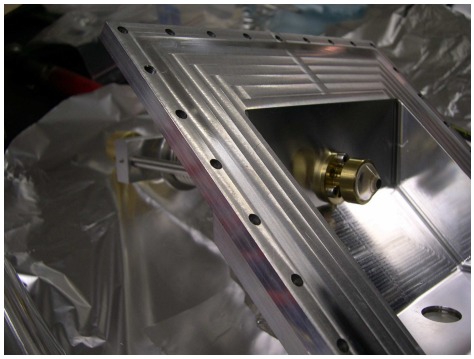

Figure 5.18: October 2009 test beam setup; cover of the 30×30 mm^2 chamber housing the fused silica radiator; the circular fused silica window used to illuminate the photocathode with the light from the UV LED is also visible.

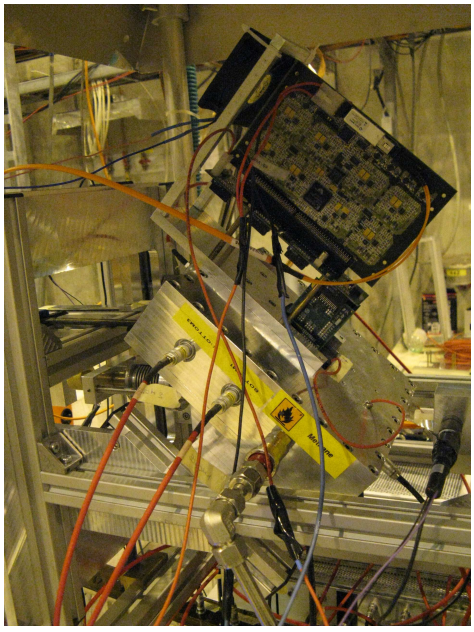

Figure 5.19: October 2009 test beam setup; the 30×30 mm^2 chamber mounted in the test setup, equipped with the front end electronic.

Chapter 6

THGEM production aspects

6.1 THGEM production processes

One of the attractive aspects of the THGEMs is the production process, based on standard PCB technologies. THGEMs can be produced by the industry, and, up to a large extent, they do not require to develop a custom production process and the related tools. Nevertheless, the production procedure, even if industrial, has to be optimised to satisfy the specific requirements concerning THGEM-based ionising particle detectors.

The THGEM samples used in our studies and, in particular, those characterised in our systematic campaign (Chapter 7) were produced either at the CERN EN ICE production facility or by ELTOS[1].

The THGEM holes are produced mechanically, by drilling the fiberglass by a milling tool mounted on a Computer Numerical Control (CNC) machine. The quality of the hole shape depends on the characteristics of the CNC machine, on the frequency of the tool replacement, and on the cleaning protocol applied after drilling.

In case of production of a large series, most of the THGEM cost arises from the drilling, depending on the number of mills used and the occupancy time of the CNC. Also the surface treatment chosen, e.g. coating with Nickel/Gold, has a relevance in determining the cost. High technology industry can offer drilling costs of about 1 Euro per 1000 holes. As an example, the total number of holes for our prototype 600×600 mm^2 is about

[1]ELTOS S.p.A., loc. S. Zeno Strada E44, 52100 Arezzo, Italy.

600,000 and the pure drilling cost is of 600 Euros.

A good example of cleaning procedure is the protocol used at CERN EN ICE; it involves three steps:

1. an ultra-sonic bath employing meta-silicate sodium solved in water (10 g/l);

2. an ultra-sonic rinsing phase with the demineralised water;

3. a spray of ethanol followed by a baking cycle to dry the PCB.

The aim of the cleaning procedure is to remove the manufacture residuals in order to avoid sparks due to point effect. A similar cleaning procedure is performed by ELTOS. It has to be stressed that a relevant by-product due to rim etching is the smoothing of the copper edges at the THGEM electrode surfaces.

In the following, the five different techniques for rim production are discussed [104][105]: one developed at the Weizmann Institute, one by R. de Oliveira at CERN EN ICE and three by ELTOS in contact with our research group. A brief description of the procedures follows:

1. *Weizmann procedure*: the standard PCB lithographic image transfer followed by standard etching is applied to the Cu-clad fiberglass plate; then the holes are produced via mechanical drilling. This procedure results in off-centre rims (Fig. 6.1). In Fig. 6.2 the procedure is schematically described.

2. *De Oliveira procedure*: a photoresistive layer is applied before drilling, but there is no image transfer; after drilling, etching attacks the copper unprotected surface, namely that at the hole edges created by drilling: a rim with uniform width around the hole is created. Then the photoresistive layer is stripped away. In Fig. 6.3 and Fig. 6.4 the picture of a microscopic cross section of a THGEM obtained by this procedure and the procedure scheme are shown.

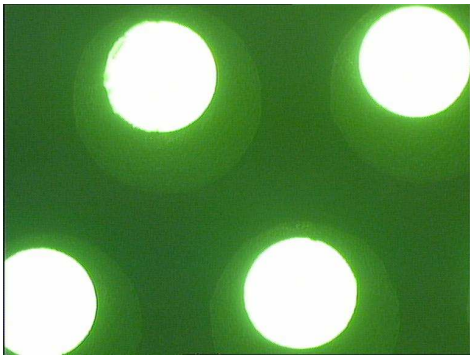

Figure 6.1: THGEM with 0.1 μm rim, manufactured employing the Weizmann procedure.

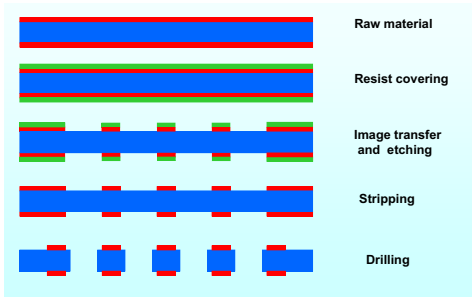

Figure 6.2: Sketch of the various steps of the Weizmann procedure for THGEM production.

Figure 6.3: Picture of the cross section of a THGEM obtained by the De Oliveira procedure.

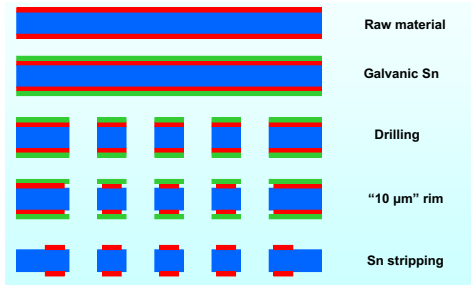

Figure 6.4: Sketch illustrating the De Oliveira procedure for THGEM production.

3. *ELTOS chemical etching*: the photoresistive layer is applied after drilling; the image transfer follows using the holes position as reference so that the resulting rim are well centred (Fig. 6.5). Figure 6.6 gives the schematic presentation of the procedure.

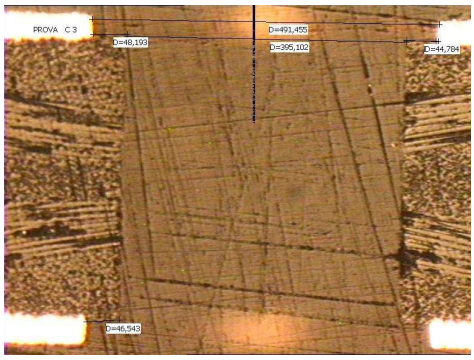

Figure 6.5: Picture of the cross section of a THGEM obtained by the ELTOS chemical etching procedure.

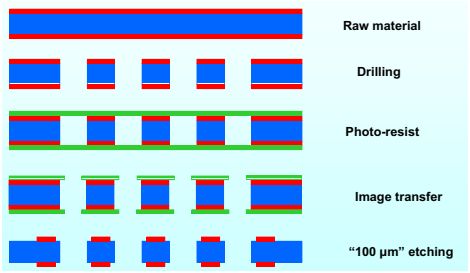

Figure 6.6: Scheme of the ELTOS chemical procedure.

4. *ELTOS global etching*: no photoresistive layer is used; after drilling, etching attacks the copper at the hole edges and at the plate surface. This technique is suitable to obtain small rims, typically ∼10 μm (Fig. 6.7). Figure 6.8 summarises the procedure. The extension of this procedure to the production of large area THGEMs presents difficulties because of the control of the etching velocity uniformity over large surfaces. Standard etching can be replaced by the micro etching technique (>5 μm), where different etching compounds are used: the reduced reaction velocity is compatible with the production of large PCBs with uniform characteristics.

5. *ELTOS pure mechanical procedure*: it is a triple drilling procedure; the rim is obtained using a milling tool with diameter larger than that used to drill the hole. The rim on the second face is obtained by reversing the plate. The rim surface is inclined by 120 degrees respect to the PCB surface (Fig. 6.9).

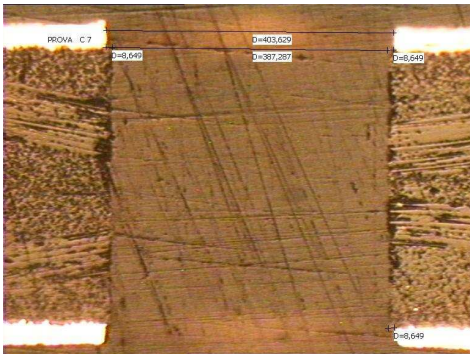

Figure 6.7: Picture of the cross section of a THGEM obtained by the ELTOS global etching procedure.

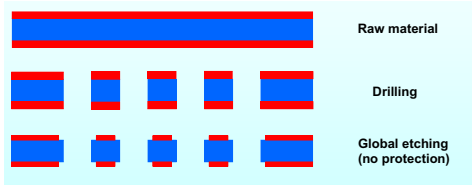

Figure 6.8: Scheme of the ELTOS global etching procedure.

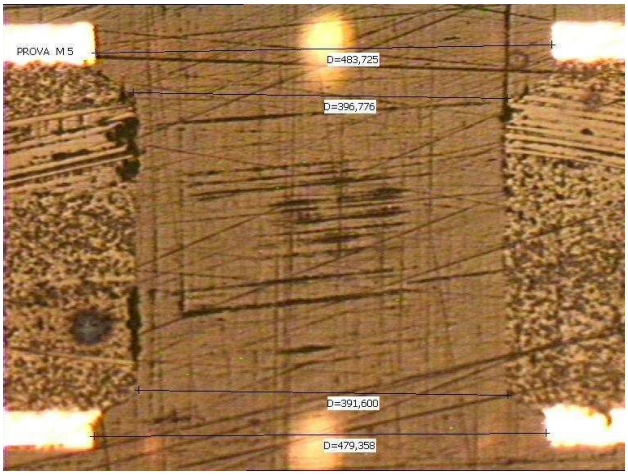

Figure 6.9: Picture of the cross section of a THGEM obtained by the ELTOS pure mechanical procedure.

A procedure considered, even if not applied so far, is to perform image transfer activating the photoresistive layer by a laser beam: this approach can offer good image precision, without precision losses even for large PCBs.

For our studies, the THGEM produced have two different sizes: 30×30 mm^2 samples, mainly used for the characterisation and the photon detection tests, and 100×100 mm^2 samples (Fig. 6.10), employed both for characterisation studies and to attack engineering aspects, as they represent an intermediate step between the small and large size THGEM.

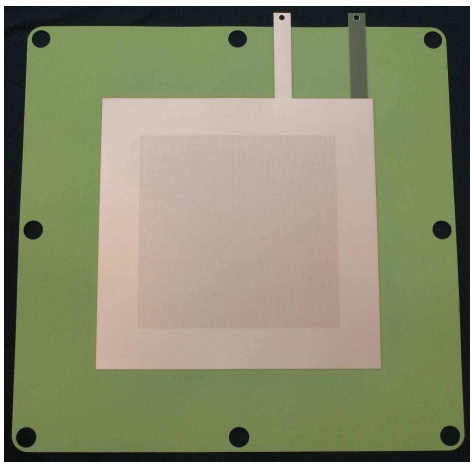

Figure 6.10: Picture with 100×100 mm^2 active area THGEM.

In table 6.1, the geometry and the treatment of most of the THGEMs tested are listed.

Name	Diameter (mm)	Pitch (mm)	Thickness (mm)	Rim (μm)	Treatment	Material
F_0_rim	0.3	0.7	0.4	0	none	Isola[a]
F_10_rim	0.3	0.7	0.4	10	chemical	Isola
F_100_rim	0.3	0.7	0.4	100	none	Isola
F_0/100_rim	0.3	0.7	0.4	0/100	none	Isola
K_10_rim	0.3	0.7	0.4	10	none	kapton[b]
F_plate_1	0.3	0.7	0.6	0	none	Isola
F_plate_2	0.3	0.6	0.6	0	none	Isola
F_plate_3	0.3	0.5	0.6	0	none	Isola
F_plate_5	0.4	0.7	0.6	0	none	Isola
F_plate_9	0.5	0.7	0.6	0	none	Isola
M1	0.4	0.8	0.4	0	none	Panasonic[c]
M2	0.4	0.8	0.4	0/25	mech. drilling	Panasonic
M3	0.4	0.8	0.4	0/50	mech. drilling	Panasonic
M4	0.4	0.8	0.4	0/100	mech. drilling	Panasonic
M5	0.4	0.8	0.4	50	mech. drilling	Panasonic
C1	0.4	0.8	0.4	10	chem.etching	Panasonic
C2	0.4	0.8	0.4	25	chem.etching	Panasonic
C3	0.4	0.8	0.4	50	chem.etching	Panasonic
C3I	0.4	0.8	0.4	50	chem.etching	Isola
C4	0.4	0.8	0.4	100	chem.etching	Panasonic
C5	0.4	0.8	0.4	10	laser+chem. etching	Panasonic
C6	0.4	0.8	0.4	50	laser+chem. etching	Panasonic
C7	0.4	0.8	0.4	10	global etching	Panasonic
M2.6	0.4	1	0.6	0	global etching	Panasonic
M2.7	0.3	1	0.6	0	global etching	Panasonic
M2.10	0.4	0.8	0.8	0	global etching	Panasonic
M2.11	0.3	0.8	0.8	0	global etching	Panasonic
M2.12	0.4	1	0.8	0	global etching	Panasonic
M2.13	0.3	1	0.8	0	global etching	Panasonic
C2.1	0.3	1	0.6	2	global etching	Panasonic
C2.2	0.3	1	0.6	5	global etching	Panasonic

List of the THGEMs used in the tests; their geometrical parameters, the material used and the treatments applied are indicated.

[a] DE-156 Halogen free, www.isola-group.com

[b] APICAL® AV Kaneka Corporation Pasadena, USA, http://www.kanekahightech.com

[c] Halogenfree FR4, http://www.panasonic-electronic-materials.com/peweme/en/downloads/R-1566W_R-1551W.pdf

6.2 A preliminary test of the produced THGEM: HV response

The maximum voltage that can be applied between the two THGEM faces in nitrogen atmosphere without exposure to radiation sources, gives indications about the characteristics and quality of the produced pieces and information about the role played by geometrical parameters in limiting the maximum voltage which the THGEM can stand. The setup used for these measurements is shown in Fig. 6.11; it consists in a plastic box similar to the one already described in Sec. 5.8.

A constant gas flow flushes in the box. The THGEM PCB under test is electrically well insulated. Currents are read via picoammeters (Sec. 5.4).

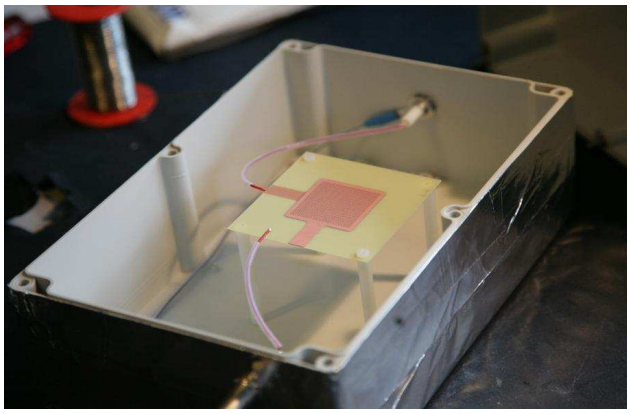

Figure 6.11: Setup used to measure the maximum voltage that a THGEM sample can stand.

The definition of the maximum bias that can be applied is the following: the maximum applied voltage for which there are no discharges for at least three minutes. The results are summarised in Fig. 6.12. The list of the THGEMs tested with their characteristics is provided in Table 6.1. Higher maximum voltage can be obtained for small rim THGEMs produced by either chemical or global etching respect to the THGEMs without rims.

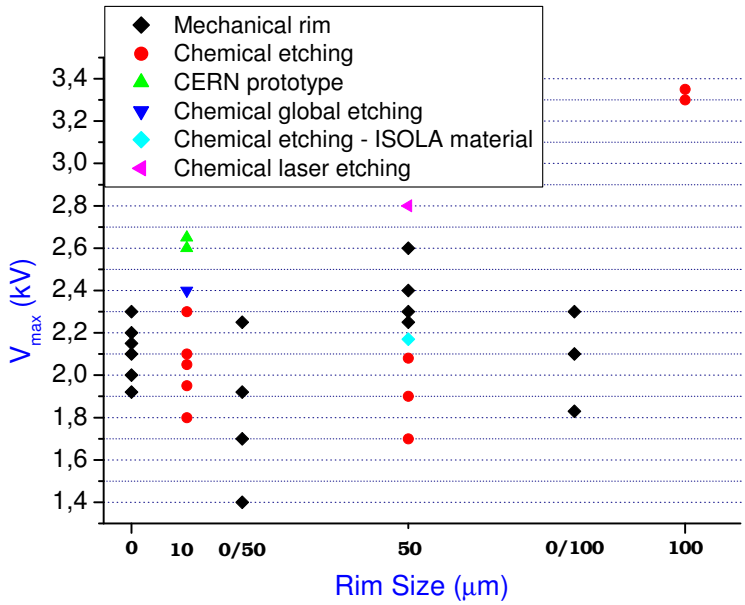

Figure 6.12: Results of the maximum voltage measurements (details in the text and in Table 6.1).

Name	Diameter (mm)	Pitch (mm)	Thickness (mm)	Rim (μm)	Treatment	Material
C1	0.4	0.8	0.4	10	chem.etching	Panasonic
C3	0.4	0.8	0.4	50	chem.etching	Panasonic
C4	0.4	0.8	0.4	100	chem.etching	Panasonic
C6	0.4	0.8	0.4	50	laser+chem. etching	Panasonic
C7	0.4	0.8	0.4	10	global etching	Panasonic
F_100_rim	0.3	0.7	0.4	100	none	Isola
M1	0.4	0.8	0.4	0	none	Panasonic
M3	0.4	0.8	0.4	0/50	mech. drilling	Panasonic
M4	0.4	0.8	0.4	0/100	mech. drilling	Panasonic
M5	0.4	0.8	0.4	50	mech. drilling	Panasonic

Table 6.1: List of the THGEMs used for the maximum voltage measurement; their geometrical parameters, the material used and the treatments applied are indicated.

6.3 Production of large size THGEMs

Three large size THGEMs with active area 576×576 mm^2 (Fig. 6.13) have been produced by ELTOS.

The geometrical parameters are: diameter: 0.4 mm, pitch: 0.8mm, thickness: 0.6 mm and rim: 5 μm. The pieces were produced by the micro etching procedure. The drilling procedure took 30 hours per piece.

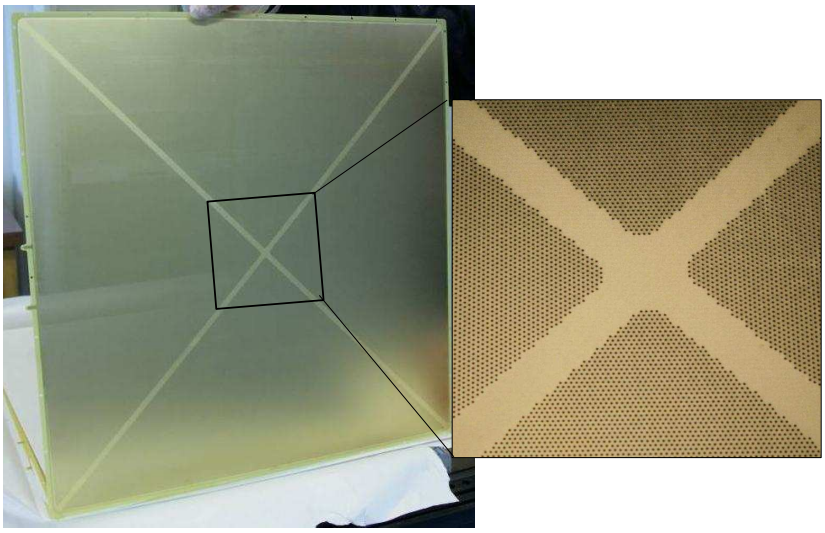

Figure 6.13: Picture of a large size THGEM prototype with active area of 576×576 mm^2 and a zoom of the central portion.

Chapter 7

Characterisation of the THGEM for applications in ionising particle detectors

7.1 The characterisation studies

In spite of the rich literature about the THGEM devices (Chapter 4), a systematic characterisation taking into account the geometrical parameters and the production aspects is missing. This has been the goal of our initial THGEM studies and more than 30 different THGEMs have been characterised.

7.2 THGEM characterisation protocol

The THGEM characterisation is performed assembling detectors that include a single THGEM layer (Sec. 5.2) and irradiating the chambers with soft X-rays (Sec. 5.3). The protocol for the THGEM characterisation has been defined after a set a preliminary measurements, that have allowed us to gain some experience in dealing with these devices. The protocol includes eight steps, as reported:

1. The THGEM is kept in an oven at 40-50 °C, before mounting it in the detector to remove the humidity.

2. The detector is flushed at a rate of 5 l/h for 2-3 hours with the proper

gas mixture $Ar/C0_2$ (70:30) before starting the measurements, to assure the correct internal atmosphere.

3. The dipole voltage for the following steps is selected: no drift and induction fields are applied and the dipole voltage is increased to determine the maximum voltage that the detector can stand; the voltage setting is this maximum value decreased by 200 V.

4. A long (some days) measurement is performed with constant voltage and irradiation and reasonable choices for the fields above and below the THGEM device, namely $E_{induction}$ ($\sim$3.5 kV/cm) and E_{drift} ($\sim$1.5 kV/cm). The purpose of this procedure is to reach stable conditions concerning the material charging-up effects and the dielectric polarisation (Sec. 7.3). Amplitude spectra are collected at regular time intervals.

5. An induction scan is performed varying the induction field and keeping fixed the voltage applied to the THGEM and the drift field.

6. A drift scan is performed varying the drift field and keeping fixed the voltage applied to the THGEM and the induction field.

7. A dipole voltage ΔV scan is performed varying the dipole voltage and keeping fixed the induction and the drift field.

8. A gain measurement for a specific voltage setting, with field settings near to the optimal configuration as indicated by the previous steps, is performed measuring the anode current varying the irradiation rate.

7.3 The long term stability of THGEM-based detectors

We discuss here the data collected applying step n. 4 of the protocol procedure described in Sec. 7.2. In Figs. 7.1 and 7.2, the measurements relative to 4 THGEMs with identical geometrical parameters (d=0.3 mm, p= 0.7 mm and t=0.4 mm.) except the rim, ranging from 0 to 0.1 mm are shown. The

conditions for the measurements are summarised in Table 7.1. During the first minutes of this long measurements, some discharges inside the detector can occur, but, in general, this phenomenon is limited to the very initial part of the measurement. These discharges are visible in the plots because they corrupt the amplitude measurements and they appear as spikes. This initial instability is due to the charging up dynamic process affecting the gain. From the plots in Figs. 7.1 and 7.2, a fast gain decrease is observed during the first minutes of the detector operation. Under irradiation, some charge settles on the THGEM insulator surfaces, namely the walls of the THGEM hole and the rim, which screens the field inside the hole. At the beginning of the process no charge is deposited and the gain is so large to induce discharges in the detector.

Rim (μm)	ΔV (kV)	$E_{induction}$ (kV/cm)	E_{drift} (kV/cm)	*Rate* (kHz/mm^2)
0	1.35	3.5	1.5	0.84
10	1.45	3.5	1.5	0.84
100	1.77	3.5	1.5	0.62
asymmetric*	1.55	3.5	1.5	0.92

Table 7.1: Detector conditions for the long term gain measurements of different THGEMs, with identical geometrical parameters (d= 0.3 mm, p= 0.7 mm and t 0.4 mm.) except the rim. (*) The THGEM with asymmetric rim has no rim on a face and 0.1 mm rim on the other face.

It is important to remark that the large size THGEM (0.1 mm) has a unique behaviour: the initial drop is common to all of them, but in the case of the 0.1 mm rim, there is a slower gain increase that modifies the gain by a factor of 2 and more. Another relevant comment concerns the different time needed to reach a stable gain; in particular for the THGEM with 0.1 mm rim the stabilisation time is longer than twenty-four hours. This behaviour is a serious source of concern: for applications in an experiment it is problematic to use a device, which exhibits so relevant time dependence. Moreover, THGEMs with small or no rim show similar gain versus time behaviour; after the initial gain drops that takes place within a few minutes, the gain is pretty stable.

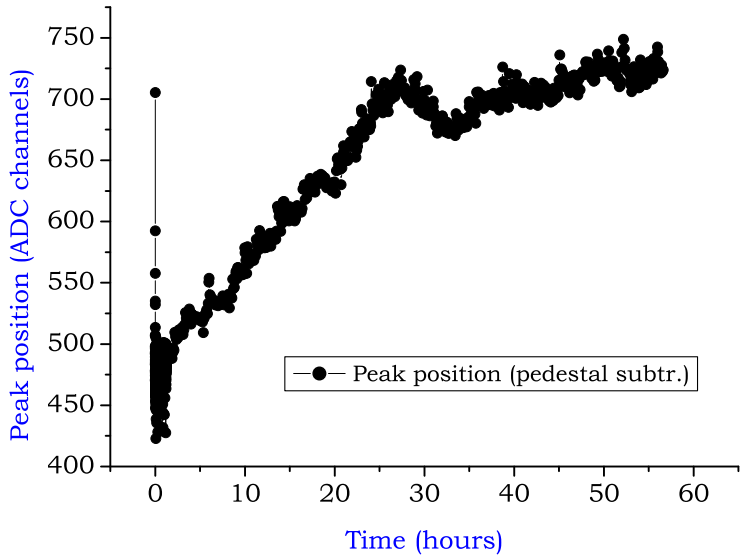

Figure 7.1: Long term gain measurement for a THGEM with 100 μm rim.

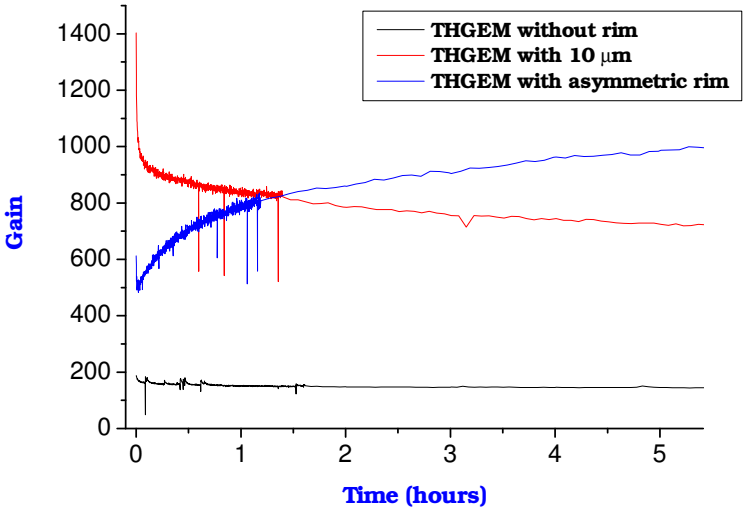

Figure 7.2: The long term gain measurements for THGEMs with the same geometrical parameters except the rim size (Table 7.1).

About the asymmetric rim configuration, it is expected to have different

gain behaviours depending on the side facing the drift electrode. Actually, in our measurements, no significant variation between the two orientations was noticed. A summary of the gain attainable employing different rim size is given in Fig. 7.3.

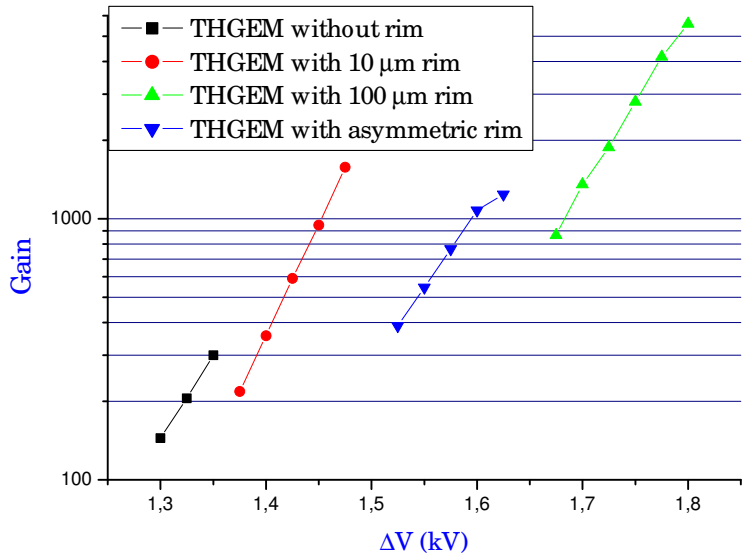

Figure 7.3: Gain versus dipole voltage obtained using the same THGEMs of Figs. 7.1 and 7.2.

The effects of the other geometrical parameters has been investigated as well, comparing the behaviour of THGEMs with identical geometrical parameters apart from the hole diameter or apart from the pitch (Table 7.2, Figs. 7.4 and 7.5). The long term gain measurements are presented in Fig. 7.6: the gain versus time shows a behaviour similar to the one obtained for other THGEMs with zero rim. The measurement conditions are given in table 7.3; they have been kept as similar as possible to make it possible an accurate comparison. An increase of the gain is observed decreasing the hole diameter and decreasing the pitch, Fig. 7.7.

Other long term gain measurement have been performed recording the currents relative to all the detectors electrodes instead of the amplitude spectra; an example is shown in Fig. 7.8. The data have been obtained using two

Name	*Diameter (mm)*	*Pitch (mm)*	*Thick (mm)*	*Rim (μm)*
THGEM #1	0.3	0.7	0.6	0
THGEM #2	0.3	0.6	0.6	0
THGEM #3	0.3	0.5	0.6	0
THGEM #5	0.4	0.7	0.6	0
THGEM #9	0.5	0.7	0.6	0

Table 7.2: Geometrical parameters of the THGEM used to study the performance dependence on the hole diameter and the pitch.

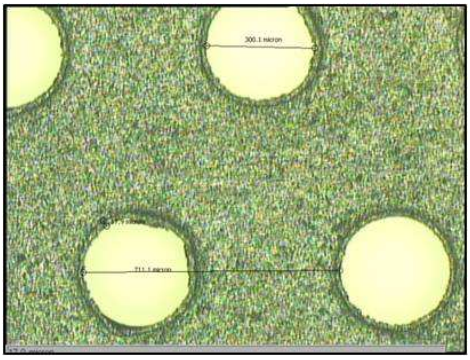

Figure 7.4: Picture of THGEM # 1: d=0.3 mm, p=0.7, t=0.6 mm, rim=0.

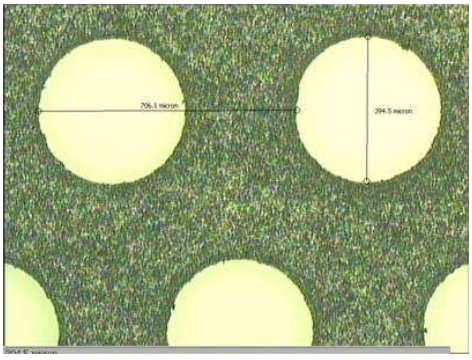

Figure 7.5: Picture of THGEM # 2: d=0.4 mm, p=0.7 t=0.6 mm, rim=0.

Name	ΔV *(kV)*	$E_{induction}$ *(kV/cm)*	E_{drift} *(kV/cm)*	*Rate* *(kHz/mm^2)*
THGEM #1	1.75	3.5	1	0.9
THGEM #2	1.77	3.5	1.5	0.8
THGEM #3	1.75	3.5	1	0.76
THGEM #5	1.77	3.5	1	0.8
THGEM #9	1.8	3.5	1	0.8

Table 7.3: Detector conditions for the long term gain measurements of the THGEMs of Table 7.2.

different THGEMs described in Table 7.4, while the detector conditions are given in Table 7.5.

The detector response also depends on the irradiation history of the THGEM. This is illustrated in Figs. 7.9 and 7.10, where data relative to

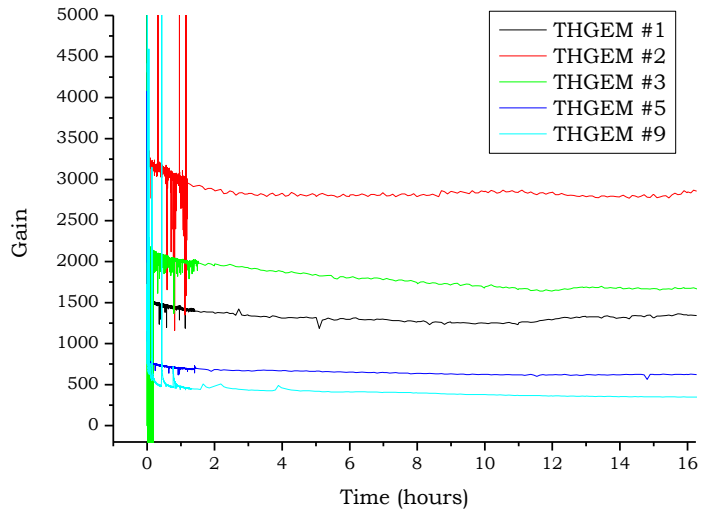

Figure 7.6: Long term gain measurements for the THGEMs of Table 7.2.

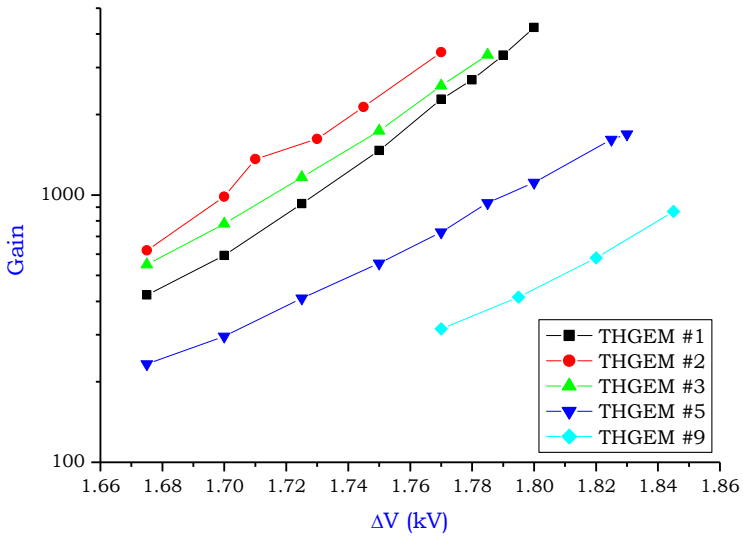

Figure 7.7: Gain versus dipole voltage obtained using the THGEMs described in Table 7.2.

the THGEMs described in Table 7.4 are shown: M1 for Fig. 7.9 and C4 for Fig. 7.10. The two sets of data presented in each figure correspond to two

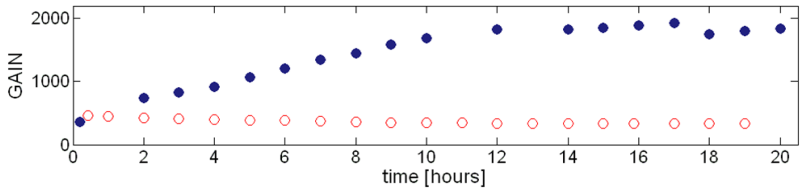

Figure 7.8: Long term gain measurement for THGEM type C4 (closed circles) and for THGEM type M1 (open circles); THGEM descriptions are given in Table 7.4, detector conditions in Table 7.5.

Name	*Diameter (mm)*	*Pitch (mm)*	*Thick (mm)*	*Rim (μ m)*
C4 ●	0.4	0.8	0.4	100
M1 ○	0.4	0.8	0.4	0

Table 7.4: Geometrical parameters of the THGEMs C4 and M1.

Name	ΔV *(kV)*	$E_{induction}$ *(kV/cm)*	E_{drift} *(kV/cm)*
C4 ●	1.75	4	2.5
M1 ○	1.33	4	2.5

Table 7.5: Detector conditions for the long term gain measurements of the THGEMs of Table 7.4.

different irradiation histories: irradiation is started at detector switching on (triangles), and irradiation is started after the detector is kept on for 10 hours (squares). Using the large rim THGEM, large gain variations are observed for different irradiation histories. This huge effect is absent employing the THGEM without rim.

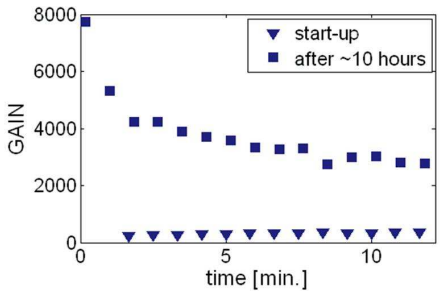

Figure 7.9: Gain versus time after starting the detector irradiation, detector formed using THGEM M1 (Table 7.4); irradiation starts at detector switch on (triangles); irradiation starts 10 hours after switching on (squares).

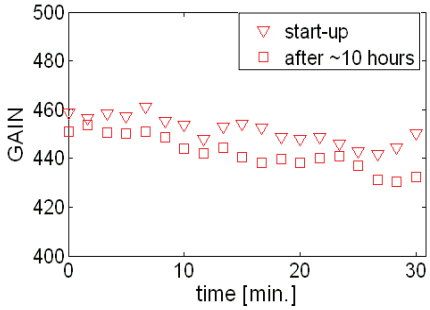

Figure 7.10: Gain versus time after starting the detector irradiation, detector formed using THGEM C4 (Table 7.4); irradiation starts at detector switch on (triangles); irradiation starts 10 hours after switching on (squares).

7.4 The performance of the THGEM-based detectors versus the drift field

Some drift scan studies are shown in Figs. 7.11, 7.12 and 7.13. The gain is obtained from the measured amplitude spectra. The primary charge collection depends on the intensity of the drift field; when the drift field is too low, the ionisation charge is not driven into the holes and part of the primary charge is lost; when the drift field is too high, part of field lines in the drift region end at the top THGEM surface instead of guiding the electrons in the holes and part of the primary electrons are lost. Between these extreme cases, there is a plateau region, where the whole primary charge is effectively collected into the THGEM holes. This is illustrated for example by the black curve in Fig. 7.12. For other THGEM geometries, a plateau is never reach up to drift fields as high as 3 kV/cm. In particular, as illustrated by the various plots, this is the case for large rim THGEMs, while a plateau is obtained for no rim or small rim THGEMs.

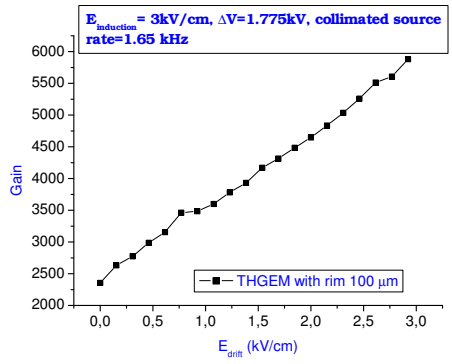

Figure 7.11: Drift scan using a THGEM with 100 μm rim; d=0.3 mm, p=0.7 mm, t=0.4 mm.

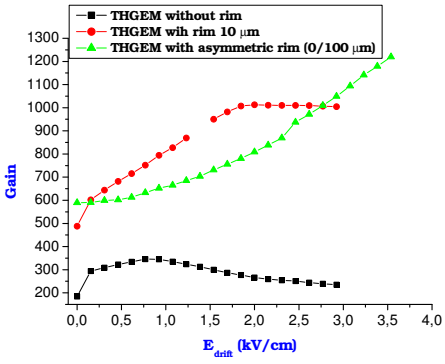

Figure 7.12: Drift scan using a THGEM with different rim sizes: d=0.3 mm, p=0.7 mm, t=0.4 mm.

The energy resolution is related to the efficiency of the primary charge collection; in the THGEM it depends on the optimisation of the drift field. The *Energy Resolution* is calculated as follows:

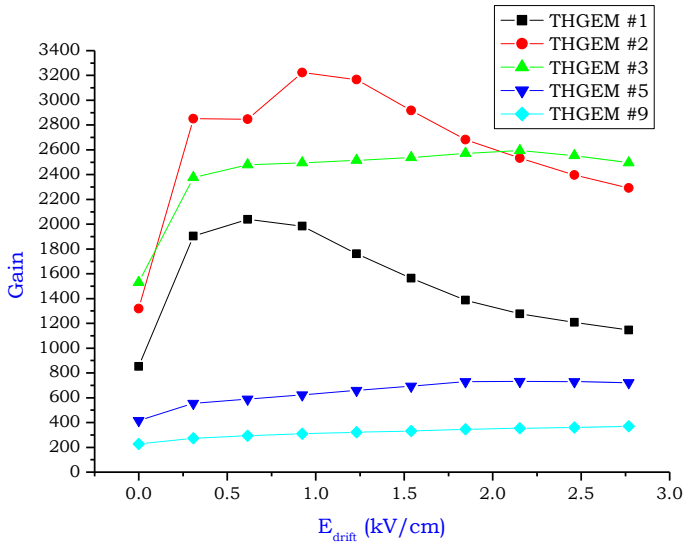

Figure 7.13: Drift scan obtained using THGEMs described in table 7.2.

$$Energy\ Resolution = \frac{FWHM}{Energy} \tag{7.1}$$

Figs. 7.14 and 7.15 provide examples of the energy resolution measured versus the drift field. The data sets in Fig. 7.14 correspond to the drift field scan given in Figs. 7.11 and 7.12, those in Fig. 7.15 correspond to the drift field scan in Fig. 7.13. The information provided by the two sets of curves matches pretty well: good energy resolution is obtained when a plateau is established in the drift curve.

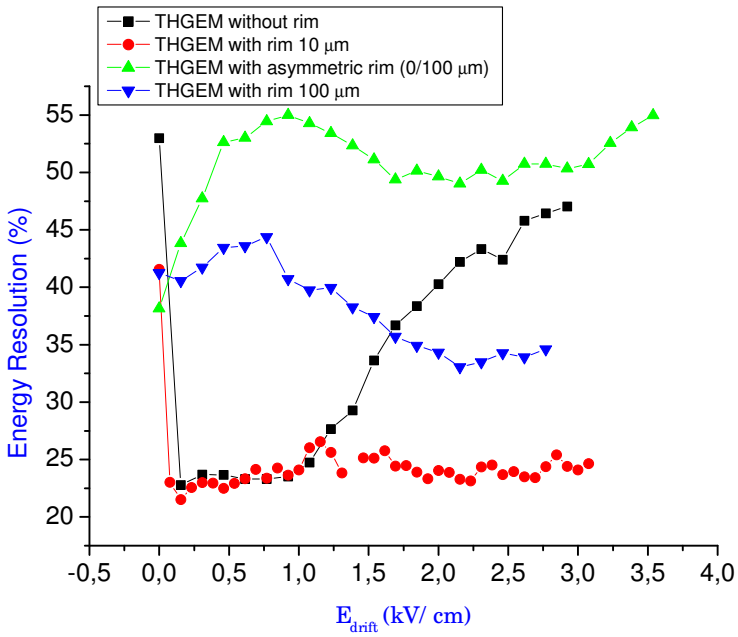

Figure 7.14: Energy resolution versus drift field for various THGEMs; d=0.3 mm, p=0.7 mm, t=0.4 mm and different rim sizes: no rim (black curve), rim=10 μm (red curve), asymmetric rim (green curve) and rim=100 μm (blue curve).

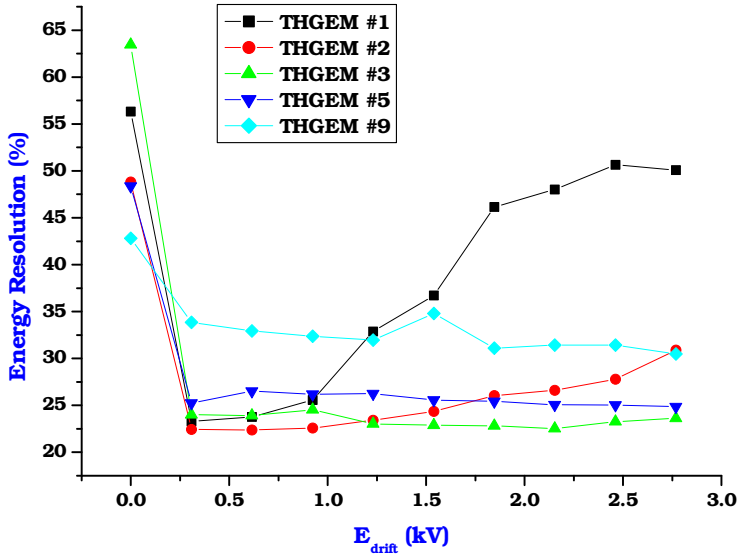

Figure 7.15: Energy resolution versus drift field obtained with the THGEMs described in Table 7.2.

7.5 The performance of the THGEM-based detectors versus the induction field

The induction field drives the avalanche electrons towards the anode. Up to a large extend, the field configuration between the bottom THGEM electrode and the anode one is the same present in a parallel plate: beyond a certain field value discharges appear. For the gas mixture of the THGEM characterisation, this value is around 8 kV/cm. In our tests we have not exceeded 6 kV/cm . The plots in Figs. 7.16, 7.17 and 7.18, where several induction scan are shown, confirm the expected behaviour, namely that the anode signal amplitude, namely the effective gain, increases linearly with the induction field.

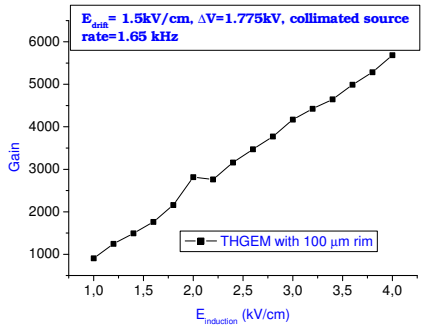

Figure 7.16: Effective gain versus the induction field; THGEM with 100 μm rim size, d=0.3 mm, p=0.7 mm, t=0.4 mm.

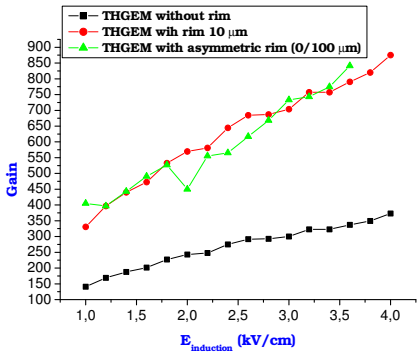

Figure 7.17: Effective gain versus the induction field; THGEMs with different rim sizes, d=0.3 mm, p=0.7 mm, t=0.4 mm.

Figure 7.19 shows the sharing of the current among the various electrodes in a THGEM detector versus the induction field. In particular, while the sum of the currents in the THGEM bottom electrode and in the anode is constant, the sharing between the two electrodes depends on the induction field.

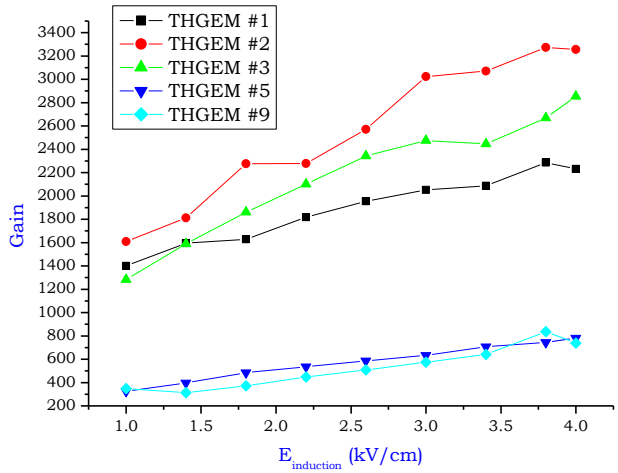

Figure 7.18: The induction scans for the THGEMs described in Table 7.2.

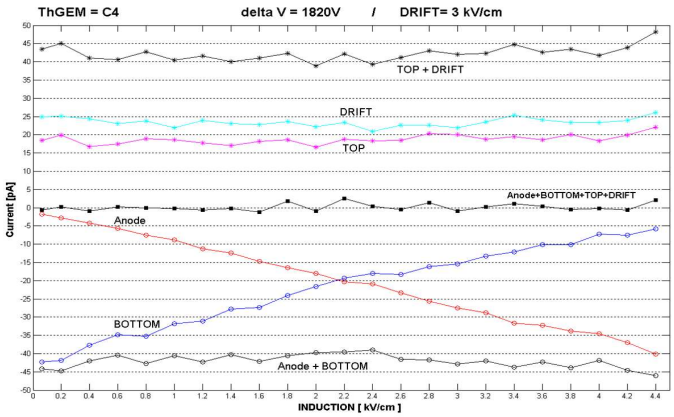

Figure 7.19: Currents relative to all the detector electrodes versus the induction field; THGEM type *C4* (Table 7.4).

7.6 The performance of the THGEM-based detectors versus the rate of ionising particles

The detector gain versus ionising particle rate has been studied determining the gain either (i) from the amplitude spectrum, after a proper calibration of the ADC used, or (ii) from the current on the anode electrode. Method (i) is preferred at low rate where there are no event overlap and the amplitude measurement is clean, while (ii) is used at high rates: currents are higher and the current measurement can be precise. At intermediate rates both measurements are performed to cross-check the outcome of the two approaches. Examples of rate measurements are presented in Figs. 7.20 and 7.21. The rate variation spans three order of magnitude, up to 10^5 Hz/mm^2. In particular, the gain variations in Fig. 7.21 are less than 15 %. The number of primary electrons is about 300; this is equivalent to a single electron rate of about 30 MHz/mm^2.

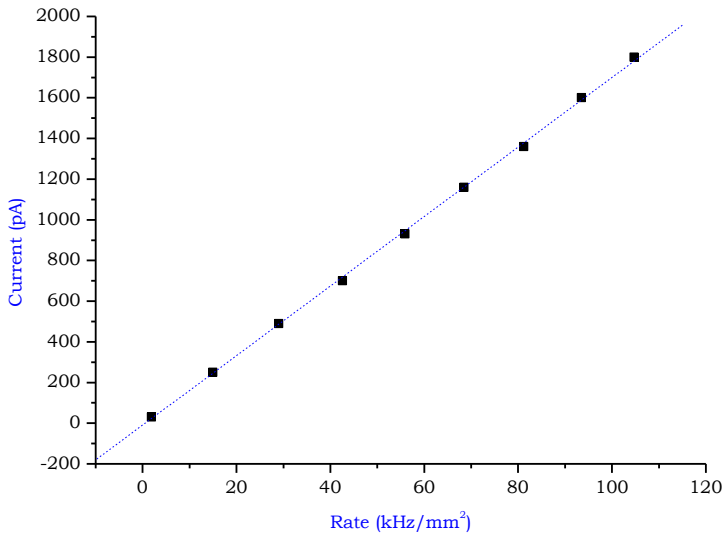

Figure 7.20: Current on the anode electrode versus rate, THGEM geometrical parameters: d=0.3 mm, p=0.7 mm, t=0.4 mm and rim=0.

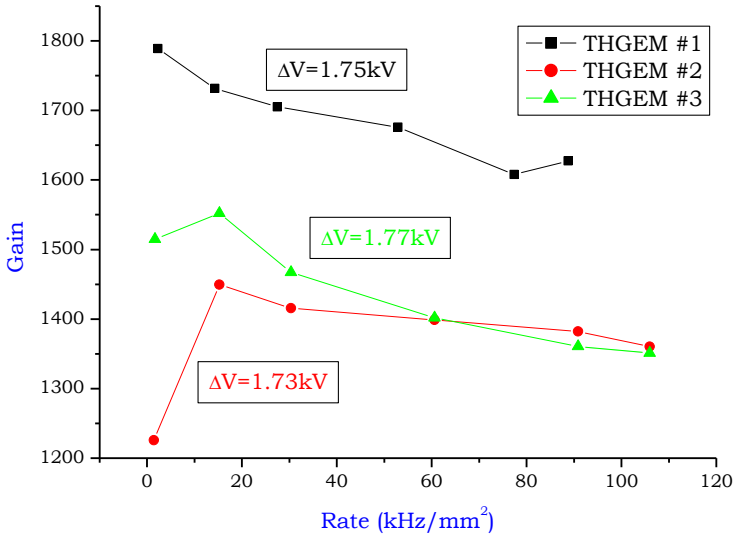

Figure 7.21: Gain versus rate obtained using three THGEMs (Table 7.2).

7.7 The Blind THGEM

To collect all the electrons produced in the multiplication process, that, in a standard THGEM-based detector are shared between the bottom THGEM electrode and the anode (Sec. 7.5), a so called Blind THGEM has been designed (Figs. 7.22 and 7.23).

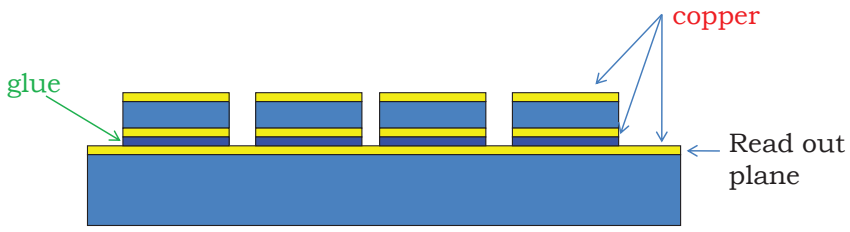

Figure 7.22: Schematic architecture of a detector based on the use of a Blind THGEM.

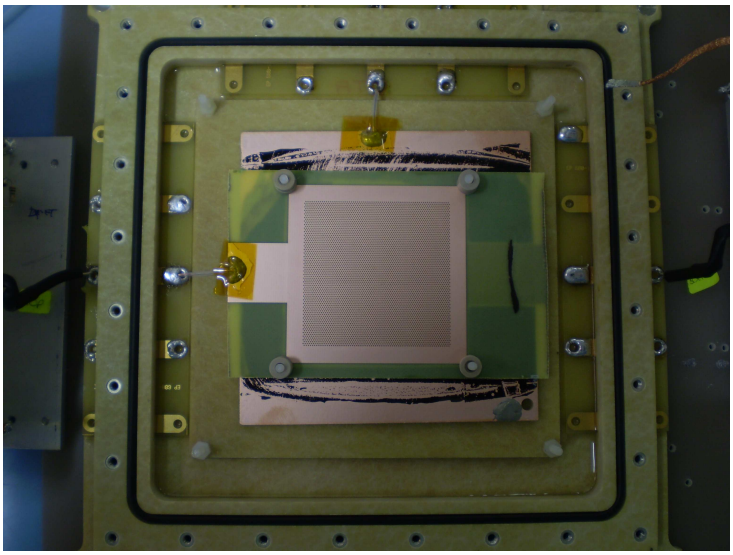

Figure 7.23: Picture of a detector including a Blind THGEM.

The Blind THGEM is built as follows. A THGEM , in particular the THGEM #5 (Table 7.2), is glued onto a fiberglass plate coated with a Cu

layer on one side (the face in front of the THGEM) employing a resistive glue. We call this plate support. This step is followed by an accurate cleaning procedure to remove glue residuals in the THGEM holes. The signal is readout from the electrode on the support. The detector is formed as the previous ones, apart from the anode which is no longer required: the support replaces it.

The signal acquired with the scope is shown in Fig. 7.24. The fast and narrow signal due to the electron motion is accompanied by the long tail due to the movement of the ions, which is prevalent. This feature is different respect to the signal formation in GEM and THGEM detectors, where the signal is mainly due to the electron motion. In the Blind THGEM the electron path in is minimum: this is why their contribution to the signal is depressed. As a consequence, while GEM and THGEM based detectors are fast, the Blind THGEM is a slow detector.

The long term gain measurement was performed in optimised drift field configuration, Fig. 7.25. In a couple of hours stable working conditions were reached.

Since the signal is largely due to the ion motion, it is expected that its development depends on the drift field, as confirmed in Fig. 7.26 where the currents of all electrodes are plotted.

The performance obtained with the Blind THGEM and THGEM #5 (Table 7.2) have been compared. The measured gains are compared, Fig. 7.27. The peculiarity of the Blind THGEM is the high gain attainable. As for the typical induction field applied to the THGEM #5 detector there is an approximately equal sharing of the electrons between the bottom THGEM and the anode electrodes, a gain increase of about a factor of two is expected using the Blind THGEM. Actually the field modification inside the holes due to the coupling of the dipole and drift field is such that the gain is increased by about a factor three.

The rate capability is shown in Fig. 7.28. The curve is obtained merging two measurements (Sec. 7.6). The gain variation over the whole rate range (three orders of magnitude) is $\sim$20 %. For completeness, we mention that in [106] a characterisation study of a Blind THGEM-like device is reported.

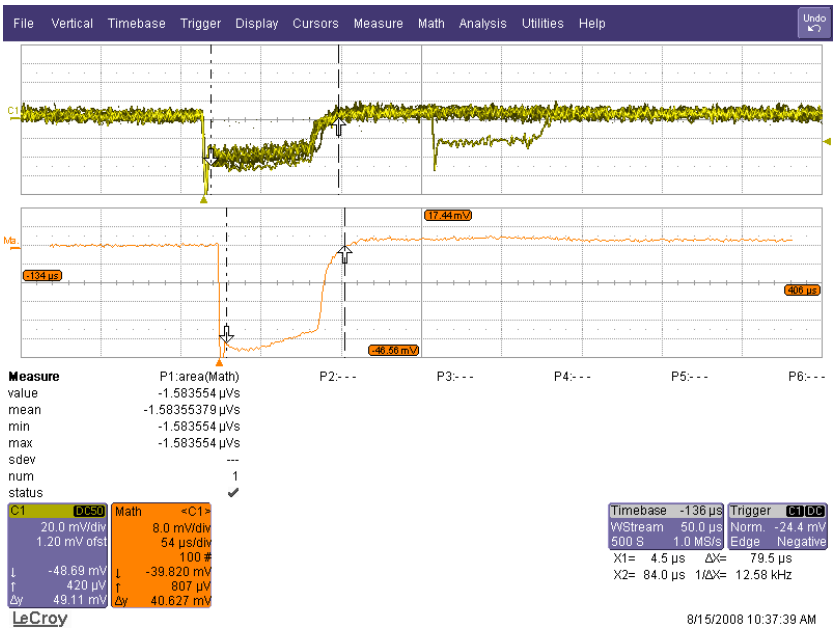

Figure 7.24: Scope image, signal obtained with the Blind THGEM (yellow line); the orange line is the mathematical average of 100 signals; time scale 50 μs per division.

This study is fully independent from our exercise.

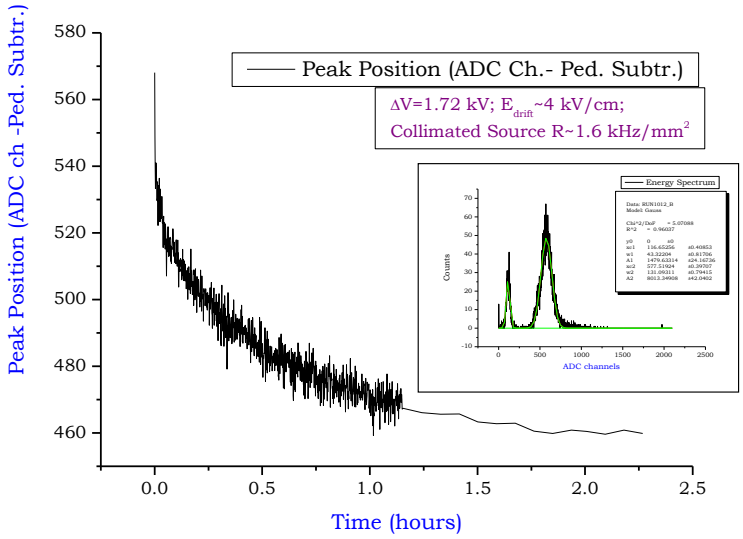

Figure 7.25: Gain versus time obtained with the Blind THGEM detector; the peak position of the amplitude spectra collected at different times is plotted; very frequent and short measurements are performed at the beginning; longer and less frequent later. An example of the amplitude spectra collected is also shown.

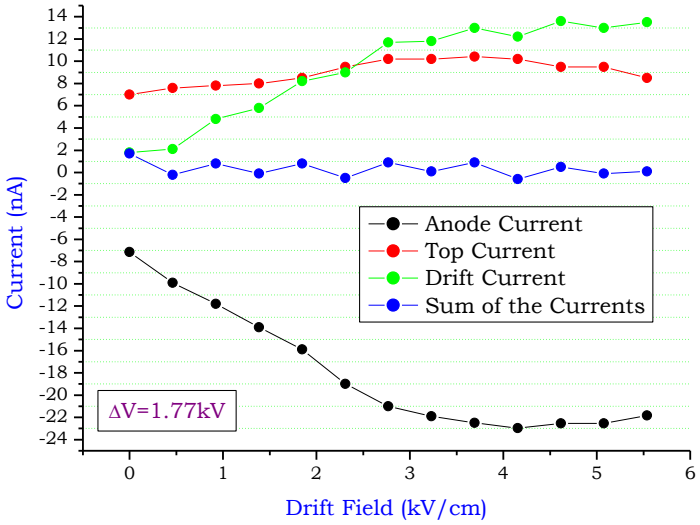

Figure 7.26: Currents on all the Blind THGEM electrodes versus the drift field applied.

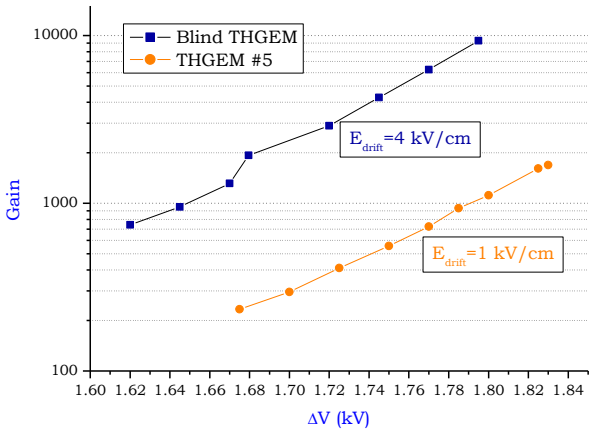

Figure 7.27: Gain versus ΔV, Blind THGEM and THGEM #5 (Table 7.2).

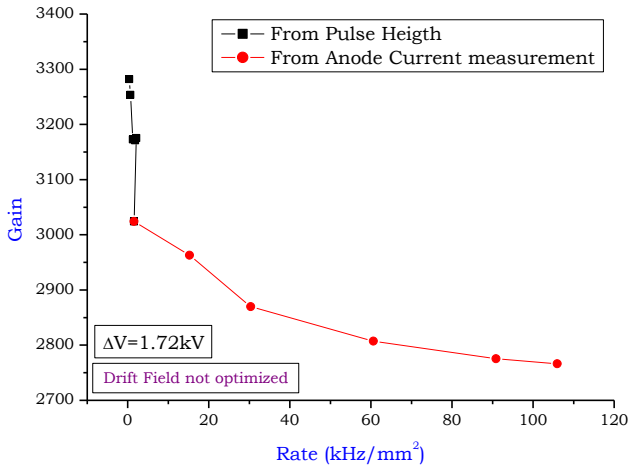

Figure 7.28: Blind THGEM detector, rate capability measurement. The two techniques used for the measurement are discussed in Sec. 7.6

7.8 Conclusions about the characterisation studies

The outcomes from this systematic study are the following:

- large rim size (∼0.1 mm) allows to reach very high gain, but the detector stabilisation time is long, the response depends on the irradiation history and rate effects are present; the energy resolution attainable is poor;
- small rims (<10 μm) or no rim devices have pretty stable response in time and do not suffer of rate effects up to extremely high rates, and good energy resolution can be obtained;
- the coupling between the drift and induction fields and the dipole field is more pronounced in THGEM than in GEM detectors due to the larger hole diameter;
- the diameter and pitch size affect the maximum gain achievable and the energy resolution;
- high gain can be obtained using Blind THGEMs, but the Blind THGEM detector is a slow detector.

Chapter 8

Effective CsI quantum efficiency in gaseous atmosphere

8.1 Effective quantum efficiency

In general, the Quantum Efficiency (QE) of a photoconverting material depends on several parameters: the nature of the material itself, the presence of contaminants, the morphology and the impinging photon energy. The QE is modified in presence of electric field. In a gas atmosphere, the photoelectrons extracted from a photoconverting material can interact with the gas molecules, experience a backscatter and be absorbed in the photoconverter; these phenomena depend on the gas atmosphere and the microscopic gas properties [108][109].

Because of all the effects mentioned above, for practical purposes instead of the absolute QE, an effective QE is considered.

8.2 Information about the effective CsI quantum efficiency from the literature

The effective CsI QE has been largely investigated by several groups, in particular, in the context of the RD26 collaboration [110], as the goal of this collaboration was to develop large gaseous photon detectors for particle

identification employing CsI photocathodes. A protocol for CsI deposition that maximises the effective QE and allows to obtain reproducible results is one of the achievements of RD26 collaboration. The CsI is evaporated by Joule effect in vacuum (10^{-7} to 10^{-6} Torr), at rates between 2 to 10 nm/s and at 50 to 60 °C. The substrates are accurately cleaned and out-gassed at 60 °C under vacuum before the evaporation. The crucibles, closed by shutters, are kept at evaporation temperature for a few minutes before starting the coating. The same shutters are closed when the desired thickness of the CsI film (typically 600 nm) is reached. After evaporation, the layer is kept for several hours under vacuum at 50-60 °C. Besides, the morphology of the CsI coating depends on the substrate. The morphological information is obtained by scanning Electron Emission (SEM), Scanning Tunnelling Microscope (STM), by Electron Microscopy for Chemical Analysis (ESCA) and Photo-Emission Electron Microscopy. The structural information is obtained from the X-rays diffraction measurements. The outcome is that the CsI layers exhibiting high effective QE are characterised by a structure of contiguous micro-crystals, which is obtained using well polished substrates, while the CsI deposited on "rough" printed circuit boards exhibits lower QE and a very inhomogeneous texture. Moreover it was observed (X-rays diffraction spectra) that the CsI evaporated on pure Cu substrates and on gold-covered copper exhibits peaks of pure Cs and pure iodine instead of CsI peaks. In fact, during the evaporation, Cu promotes the dissociation of the CsI or prevents its formation from the vapour phase. To prevent this phenomenon, a chemical deposition of a nickel layer covered by a film of gold is applied on the Cu substrate. Figure 8.1 summarises the CsI effective QE versus wavelength in vacuum obtained from a large set of measurements performed within the RD26 collaboration.

About QE in vacuum, it is important to remark that it depends also on the electric field and it reaches a plateau at about 100 V/cm, as shown in Fig. 8.2.

About the backscattering, the photoelectrons return to the photocathode because of the elastic scattering with the gas molecules. The large mass difference between the elastically scattered electrons and gas molecules de-

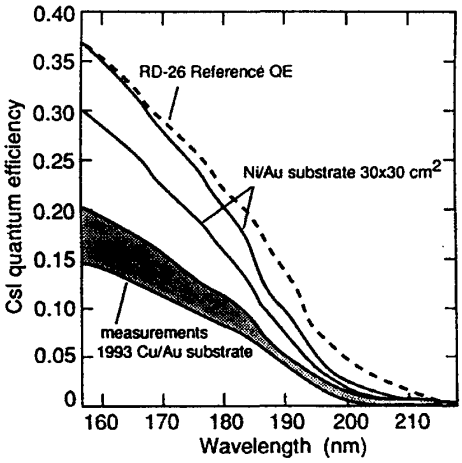

Figure 8.1: The CsI effective QE from RD26 measurements: reference curve, namely maximum obtained using a stainless steel substrate (dotted line); band of values obtained using a PCB substrate without Ni coating (black band) and with Ni coating (white band) [110].

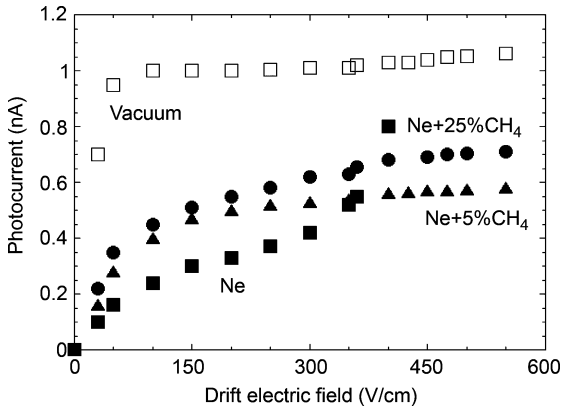

Figure 8.2: Measurement of the photo-current versus drift field in vacuum and in some gasses at atmospheric pressure [97].

termines a wide range of scattering angles, with a small energy transfer per collision. For energies below ionisation threshold, the backscattering effect is therefore more pronounced, in particular in nobles gasses, where the elastic cross section largely exceeds the inelastic one, because of the lack of vibrational and rotational levels.

At high electric field the energy of photoelectrons becomes high enough to excite and to ionise the molecules of the gas and the probability for elastic scattering decreases due to the opening of new, inelastic channels in the electron-molecule collisions.

The inelastic channels don't lead to backscattering, since the photoelectrons losses their energy without a substantial change of its direction of motion. When the probability of the elastic collisions drops down to zero, the QE in gasses should reach the vacuum value. Recently Monte Carlo simulations have been performed and compared with the experimental data in order to investigate better the photoelectron backscattering effects in several gas mixtures. In particular, Neon mixtures with quenchers (Figs. 8.3 and 8.4) have been considered [107]. Figure 8.5 summarises a large set of experimental data concerning the extraction efficiency normalised to the vacuum measurement. The extraction efficiency for CH_4 and CF_4 is larger than 0.7 times the value in the vacuum already at 1 kV/cm thanks to large vibrational cross-section as extensively reported in literature. The extraction efficiency of the Neon with 10 % of methane is around 0.6 times the value in the vacuum for 1 kV/cm at atmospheric pressure [107].

In [111], a CsI QE enhancement has been also observed in correspondence of breakdown events, when the detector is in multiplication mode or under high light flux. A concentration of positive ions on the CsI nonconductive surface may become large enough to create a high electric field within the CsI film. This could be responsible for the increase of the photoelectron extraction probability. Positive ions deposited on such regions can be gradually neutralised by charge transfer processes, for example as a charge exchange reaction with gas molecules. The neutralisation process can depend on the nature of the gas. Most likely, this phenomenon is at the base of the long recovery time after a discharge in gaseous detectors with CsI photocathodes (Sec. 2.2).

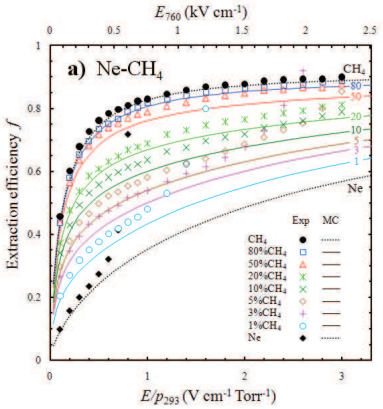

Figure 8.3: Photoelectron extraction efficiency measurements (symbols) compared with the Monte Carlo results (full and dotted curves) as a function of the reduced field (bottom scale) and electric field at 1 atm (top scale) for Neon/methane based gas mixtures [107].

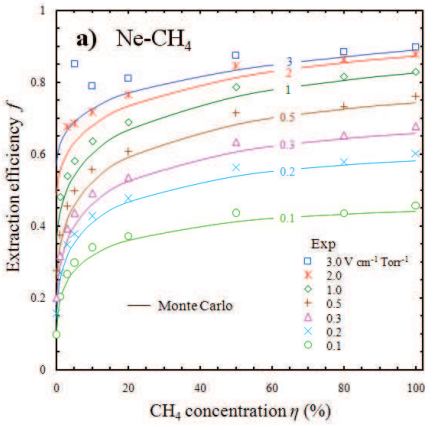

Figure 8.4: Photoelectron extraction efficiency measurements (symbols) compared with the Monte Carlo results (curves) as a function of the concentration η of methane in the Ne/CH_4 mixture for a set of reduced electric field, $\frac{E}{p}$ [107].

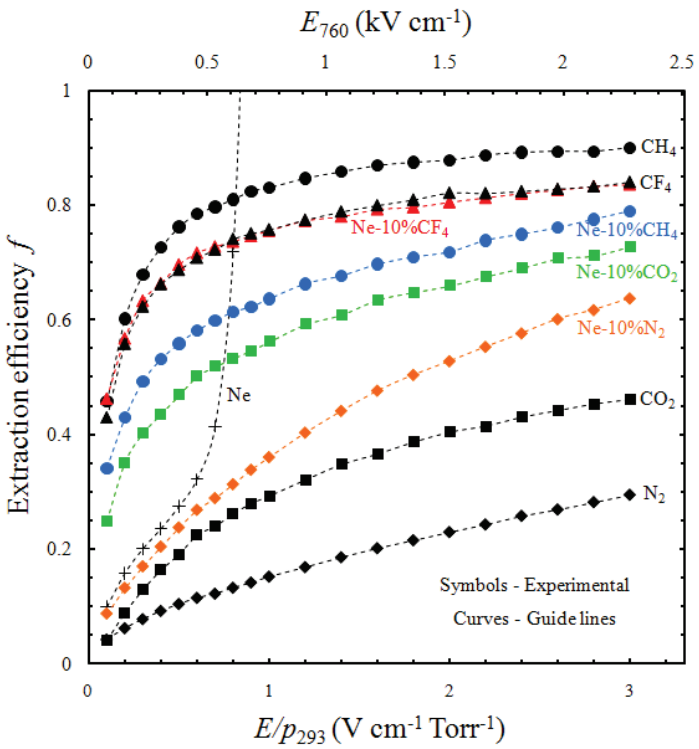

Figure 8.5: The extraction efficiency normalised to the vacuum extraction efficiency as a function of the reduced electric field (bottom scale) and the electric field (top scale) for several gasses and gas mixtures, experimental data. The curves joining the data points are guidelines [107].

8.3 Measurements of CsI quantum efficiency in gasses

We have performed a set of measurements to gain direct experience concerning the effective QE of different gas mixtures, listed in Table 8.1. We have used the chamber described in Sec. 5.8 and the light source AvaLight-D(H)-S-DUV, described in Sec. 5.7. The vacuum level reachable in our chamber is of a few Torr, namely it is not enough to perform QE measurements in vacuum. In practise, we have performed relative measurements of photocurrent comparing the results in different gas atmospheres. We use measurements in N_2 as reference, as explained in the following.

The protocol used for the measurements consists in:

1. gas evacuation of the chamber using the vacuum pump;
2. filling of the chamber with the Nitrogen at atmospheric pressure;
3. measurement of the CsI effective QE;
4. emptying of the chamber with the vacuum pump;
5. filling with the gas or gas mixture for the measurement;
6. measurements of the CsI effective QE at atmospheric pressure as well as at lower pressure values;
7. emptying of the chamber with the vacuum pump;
8. filling of the chamber with the Nitrogen at atmospheric pressure;
9. measurement of the CsI quantum efficiency.

For every measurement the temperature and atmospheric pressure conditions are recorded. The N_2 measurements acquired at the beginning and at the end of the measurement with the gas of interest allow to control the variation of the environmental conditions (pressure and temperature) during the measurement. Typically, a measurement takes three hours. The variation of the environmental conditions are considered linear in such short time

Gas	Gas	Mixture
Argon		100
Argon	CH_4	90:10
Argon	CH_4	81:19
Argon	CH_4	66:34
CH_4		100
Argon	CO_2	70:30
CF_4		100
N_2		100
Neon		100
Neon	CH_4	90:10
Neon	CH_4	81:19
Neon	CH_4	70:30
Neon	CH_4	62:38

Table 8.1: The gas mixtures used in our effective QE measurements.

interval; a nitrogen curve relative to the measurement is built averaging the two nitrogen curves. This curve is then normalised to the reference N_2 measurement, calculating a normalisation factor. It is so possible to remove the result dependence coming from the fluctuations of the light intensity. This normalisation factor is included in all our results. From a set of repeated measurements, we estimate that our results are reproducible at the $\sim$2 %, as shown in Fig. 8.6.

Figures 8.7, 8.8 and 8.9 present the photo-current measured for different gas mixtures at atmospheric pressure. From previous studies it is known that methane is one of the best gas to use coupled to obtain high effective QE using CsI as photoconverter; our data confirm this behaviour. It is important to underline that, at atmospheric pressure, a plateau in the photocurrent measurements is reached only for electric fields as high as $\sim$ 1kV/cm. Another relevant comment concerns Ar/CH_4 mixtures rich in methane ($\sim$50 %): the photocurrent is very near to what is obtained for pure methane.

For completeness, we have performed photocurrent measurements at pressures different from the atmospheric one. An example is shown in Fig. 8.10: the measurements are in good agreement with similar ones [108].

To conclude, in order to maximise the rate of extracted photoelectrons,

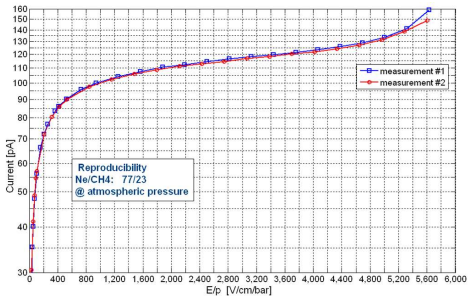

Figure 8.6: Two different photocurrent measurements at atmospheric pressure for the same gas mixture Ne/CH_4 (77:23), normalisation procedure applied. The reproducibility of the measurements is at the $\sim$2 % level.

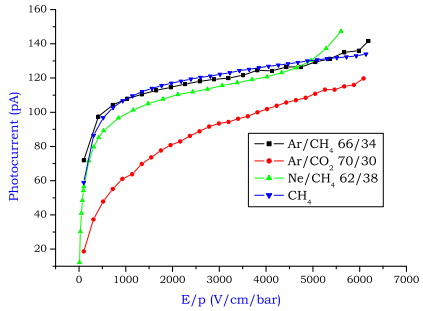

Figure 8.7: Photocurrent measurements versus reduced field for four gas mixtures at atmospheric pressure.

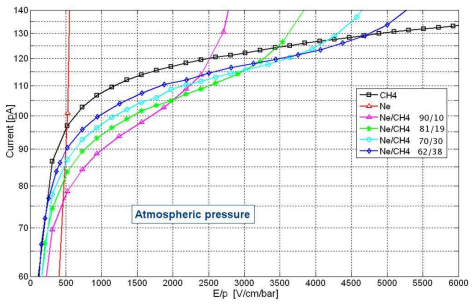

Figure 8.8: Photocurrent measurement versus reduced field in Neon/methane mixture at atmospheric pressure.

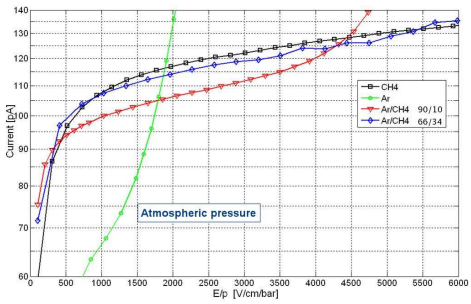

Figure 8.9: Photo-current measurement versus reduced field in Argon/methane mixture at atmospheric pressure.

the best gas choices are pure methane or argon-methane mixtures with high methane fraction. Neon-methane mixtures are interesting, but less favourable. CF_4 can also be considered. All these gas mixtures entail different voltage conditions and, as a consequence, different dipole fields on the THGEM surface. The various studies clearly indicate that high fields at the photocathode surface are desirable and, thus, the optimal gas mixture has to

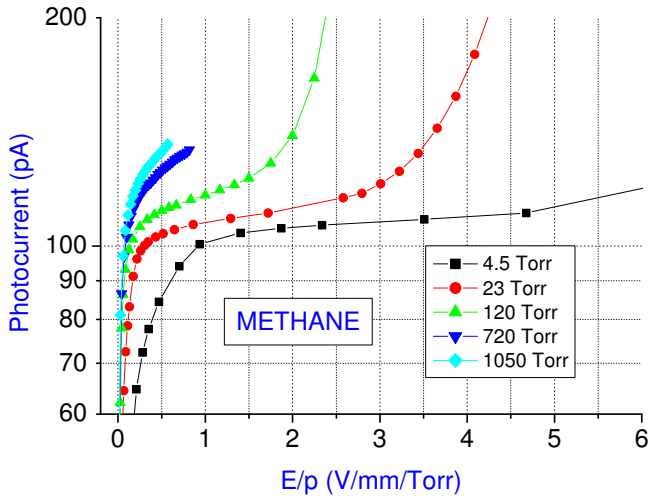

Figure 8.10: Set of the photo-current measurements in pure methane at different pressure.

be chosen also on the base of field considerations. This point will be further discussed in Chapter 9, where we report about electrostatic calculations and measurements to determine the electric field at the photocathode surface.

Chapter 9

The development of THGEM-based single photon detectors

9.1 The proposed architecture of a THGEM-based photon detector

A good photon detector requires high effective quantum efficiency, a parameter which includes the photoelectron collection efficiency (Chapter 8), and high gain in order to detect the single photons with good efficiency. The architecture that we propose for a THGEM-based photon detector takes into account these requirements: it consists in multiple THGEM electrodes, the first one coated with a CsI film and acting as a reflective photocathode; the anode electrode is segmented (Fig. 9.1).

The choice to use a reflective photocathode instead of a semitransparent one comes from the larger effective QE that can be obtained. In fact, a semitransparent photocathode requires the application of a thin metallic film to keep the entrance window at a fix potential: this metallic film absorbs photons; also, the probability of photoelectron absorption is lower in a reflective photocathode than in a semitransparent one as the conversion probability is maximum at the entrance surface of the photoconveter layer. Moreover the thickness of the coating layer is non critical in the reflective configuration, as illustrated in Fig. 9.2. Aiming at large size detectors, this consideration

is particularly important, as it is difficult to obtain a very uniform thickness of the photocathode layer over large surfaces.

Another crucial aspect is the fraction of the surface available for coating, that we indicate as *active area*: it depends on the THGEM geometry (Table 9.1). The wires of the electrode plane above the photocathode (typically 50 μm diameter and 2 mm pitch) create a small shadow on the CsI photocathode. Nevertheless, they are required because they allow to control the electric field at the photocathode surface (Sec. 9.2).

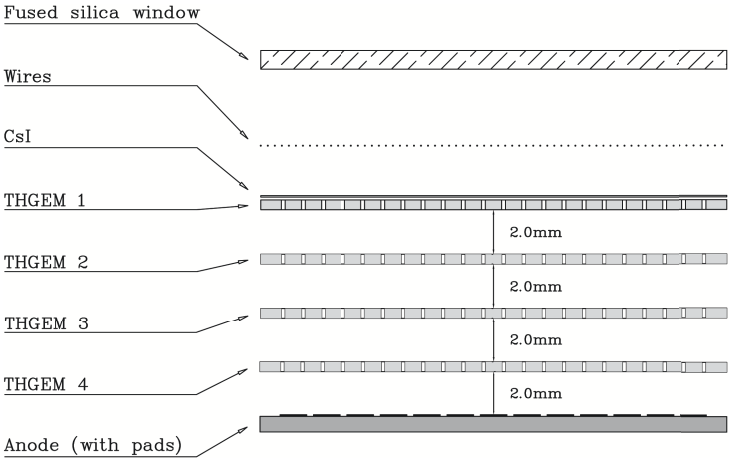

Figure 9.1: Scheme of a four-layer THGEM-based photon detector with reflective cathode (not to scale).

Diameter (mm)	Pitch (mm)	Active area (%)
0.3	0.5	67.4
0.3	0.6	77.3
0.3	0.7	83.4
0.4	0.7	70.4
0.4	0.8	77.3
0.5	0.7	53.8

Table 9.1: Active area (percentage) for THGEMs with different geometries.

Multilayer architectures provide higher gain respect to single layer structures (Sec. 9.2). Moreover multilayer architectures reduce to almost zero the

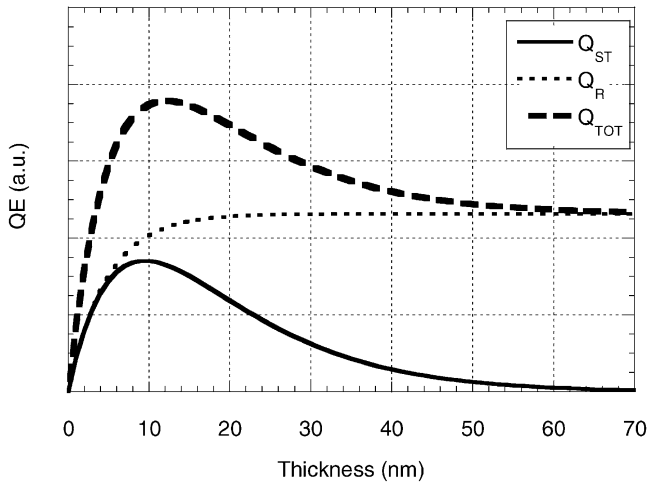

Figure 9.2: Effective QE for semitransparent QE_{ST} and reflective QE_R CsI photocathodes versus the thickness of the layer; QE_{TOT} is the sum of the two [112].

feedback of photons produced in the multiplication process and help to reduce the ions backflow towards the photocathode. As discussed in Sec. 2.3, this aspect is a crucial issue to overcome electrical instability and ageing issues of gaseous photon detectors equipped with CsI photocathode.

9.2 Gain Measurements

The amplitude distribution resulting from a multiplication process started from a single electron is a Polya distribution (Sec. 2.4), that, in the simplest case, coincides with an exponential distribution. All the spectra that we have collected using THGEM-based photon detectors, even at pretty high gain, exhibit an exponential shape. This observation is in agreement with the fact that the electric field inside the holes is highly non homogeneous, namely the multiplication factor undergoes large variations. To determine the gain, we perform a best fit of the exponential spectrum and we extract the gain value from the slope parameter.

In the following, we present results obtained using a triple THGEM struc-

ture in Ar/CH_4 (50:50) gas mixture. The THGEM geometry is: d=0.4 mm, p=0.8 mm, t=0.4 mm and rim=10 μm.

Figure 9.3 shows the amplitude spectra obtained varying the voltage of the second THGEM and keeping the remaining two at fixed voltage.

Figure 9.4 offers an example of the voltage scans for each THGEM of the triple structure, keeping unchanged the voltage applied to the other two. The THGEM labelled #1 is the THGEM with the CsI deposit while the THGEM #3 is just in front of to the anode electrode. THGEM #2 is the intermediate layer. The drift field is set at zero; the induction field and the transfer fields are set at 3 kV/cm and 1 kV/cm respectively.

As it is the case for GEM-based detectors, very similar gain values are obtained for different dipole potential over the THGEMs, provided that the sum of the differences of potential is constant.

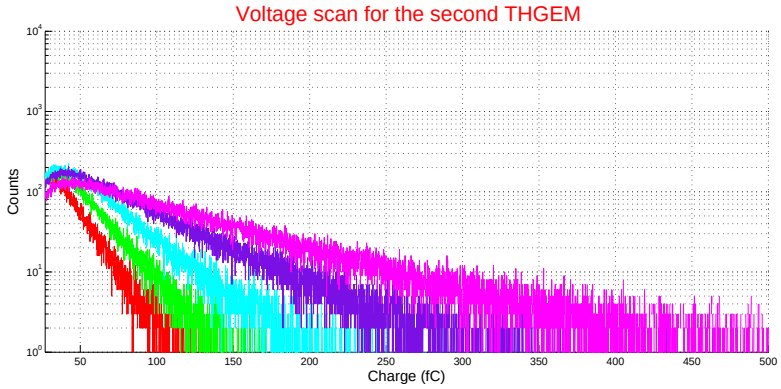

Figure 9.3: Detection of single photons, amplitude spectra obtained varying the voltage of the second THGEM. The units on the abscissa are fC.

9.3 Time Resolution

Time response has been measured employing a triple THGEM architecture in Ar/CH_4 (50:50) gas mixture at a gain of $\sim 5\times10^5$. The THGEM geometrical parameters are t=0.4 mm, p=0.8 mm, d=0.4 mm and rim=10 μm.

The electronic read-out used is described in Sec. 5.6. The light source used is the UV LED driven by the PDL 800B controller (Sec. 5.7), which

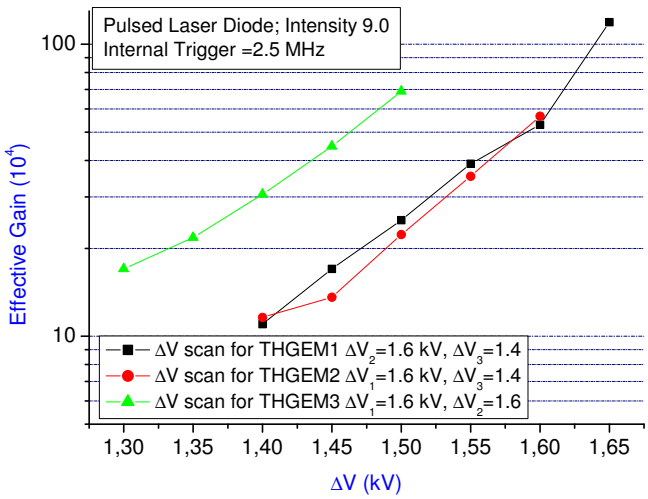

Figure 9.4: Effective gain versus the bias applied to the THGEMs.

provides 600 ps long light pulses. The illumination condition is the single photoelectron mode. The trigger used is the signal provided by the controller in coincidence with the light pulse. Figure 9.5 presents the time response obtained; the Gaussian best fit of the peak is characterised by an r.m.s. of 10.8 ns. A second example, obtained with a chamber with similar parameters (described in Sec. 5.9) operated at a gain of 7×10^4, and the same illumination, is shown in Fig. 9.6; in this case the r.m.s. of the Gaussian peak is 8.8 ns. Figure 9.7 shows the time resolution for the same chamber of Fig. 9.6 measured in substantially different conditions. The light source is the Cherenkov one produced by hadrons crossing a fused silica radiator (Sec. 5.9). The trigger is defined by the coincidence of the signals from three scintillating counters. The detector gain is 4×10^4. The r.m.s. of the Gaussian peak is 9.4 ns. These measurements indicate that a detector based on a triple THGEM structure can detect single photons with a time resolution of about 10 ns.

9.4 Photocollection efficiency

In Sec. 8.2 the photoelectron extraction efficiency is discussed in relation with the proper choice of the gas in terms of backscattering. Here we consider

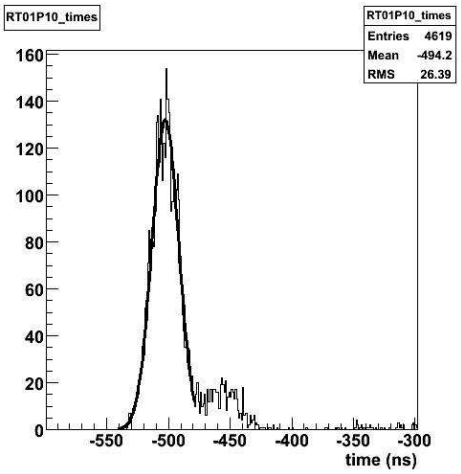

Figure 9.5: Time response of a triple THGEM detector illuminated using a LED; details about the detector, the light source and the trigger are given in the text.

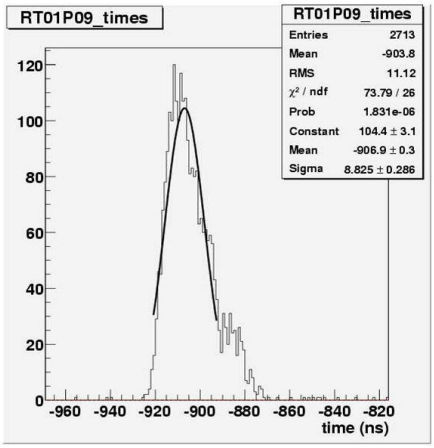

Figure 9.6: Time response of a triple THGEM detector illuminated using a LED; details about the detector, the light source and the trigger are given in the text.

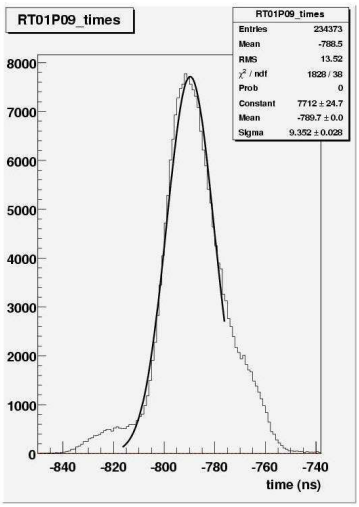

Figure 9.7: Time response of a triple THGEM detector detecting Cherenkov light; details about the detector, the measurement conditions and the trigger are given in the text.

the photoelectron extraction related to the electric field at the photocathode surface, when the photocathode substrate is a THGEM. The field at the pho-

tocathode surface is the combination of the electric field due to the dipole potential applied between the two THGEM faces and the drift field due to the potential between the photocathode surface and the drift electrode facing it. A calculation of the electrostatic fields configuration of the THGEM (parameters: diameter 0.4 mm, pitch 0.8 mm, thickness 0.6 mm and no rim) has been obtained using the software package ANSYS[1] (finite element calculation). The electron trajectories from the top THGEM surface (photocathode) for three different drift field configurations have been simulated using GARFIELD and making use of the field calculated using ANSYS; the multiplication process is switched off; the drift field configurations are: zero field, -0.5 kV/cm and 0.5 kV/cm; a bias of 1.5 kV is applied to the THGEM. When the drift field is positive, the electrode at the lowest potential is the drift one. This is the fields configuration used to detect ionising particles. When the drift field is negative, the electrode at the lowest potential is the THGEM top one. Figure 9.9 and 9.10 show the simulated electron trajectories for the zero field configuration in two orthogonal cross-sections, indicated in Fig. 9.8. Similarly, Figs. 9.11 and 9.12 show the simulated trajectories for -0.5 kV/cm drift field and Figs. 9.13 and 9.14 show the simulated trajectories for 0.5 kV/cm drift field. For zero drift field, all electrons are driven into the holes in both cross section. For -0.5 kV/cm drift field (field pointing towards the drift electrode), part of the electrons are collected at the drift electrode and, thus, lost from the point of view of the detection. For 0.5 kV/cm drift field (field pointing towards the top THGEM electrode), the sum of the drift field and the dipole field results, in certain regions of the THGEM surface, either in a field pointing inside the THGEM or very feeble; in both cases the electrons are not guided to the holes and are lost.

This modellisation has been verified experimentally, detecting UV light with a detector making use of a single THGEM, coated with CsI. The currents in all electrodes are read out by the picoammeters.

Figure 9.15 shows the variation of the anodic current versus the drift field for various settings of the dipole voltage. All the curves exhibit similar behaviour. The plots clearly indicate a sharp current decrease when the

[1] ANSYS, ANSOFT Co. Pittsburg, PA, USA

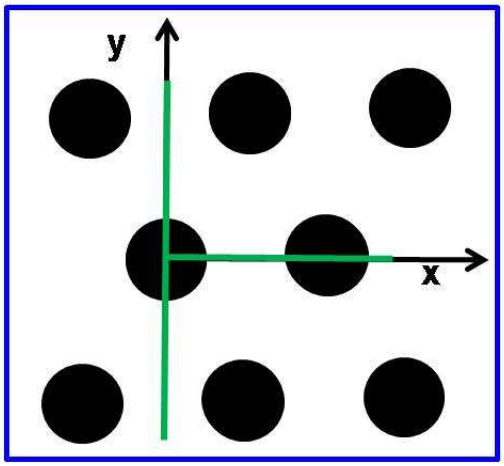

Figure 9.8: Reference frame on the THGEM surface.

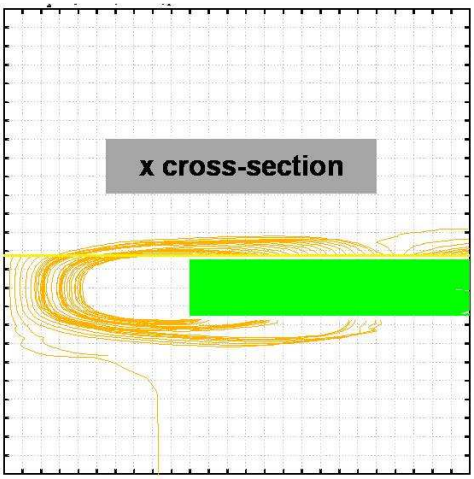

Figure 9.9: GARFIELD simulation of the photoelectrons trajectories, THGEM cross-section along the x-axis; zero drift field.

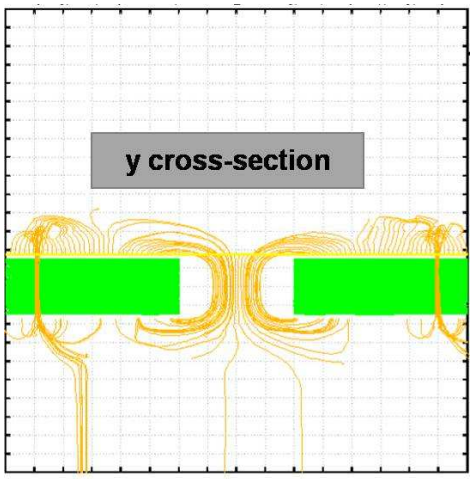

Figure 9.10: GARFIELD simulation of the photoelectrons trajectories, THGEM cross-section along the y-axis; zero drift field.

additional field points towards the drift electrode (negative field values), a rough plateau for moderate values of the additional field oriented towards the photocathode (positive field values), followed by a drop when the total field (sum of the dipole and drift fields) becomes too low. In particular, the current drops at lower values of the drift field when the dipole voltage is

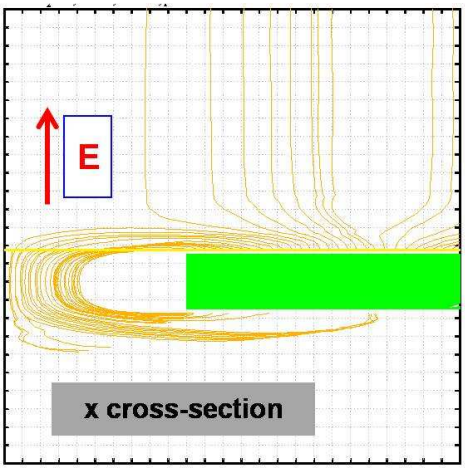

Figure 9.11: GARFIELD simulation of the photoelectrons trajectories, THGEM cross-section along the x-axis; drift field: -0.5 kV/cm.

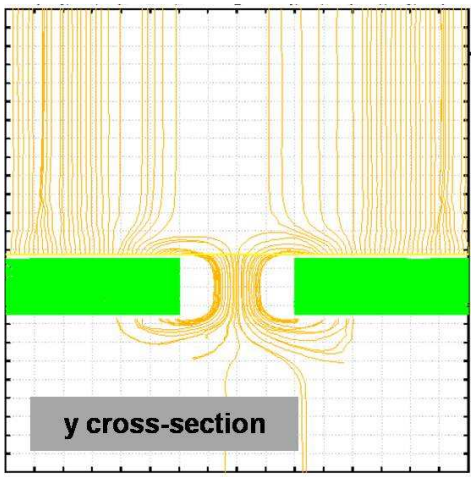

Figure 9.12: GARFIELD simulation of the photoelectrons trajectories, THGEM cross-section along the y-axis; drift field: -0.5 kV/cm.

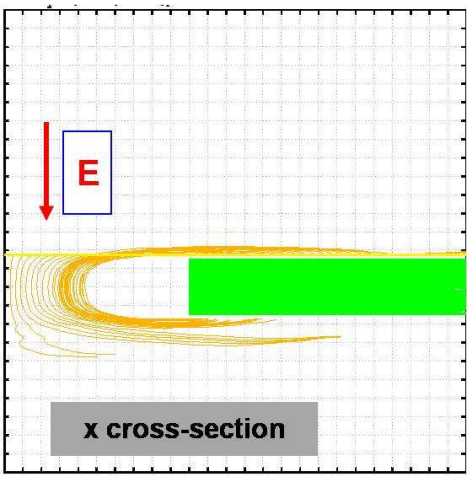

Figure 9.13: GARFIELD simulation of the photoelectrons trajectories, THGEM cross-section along the x-axis; drift field: 0.5 kV/cm.

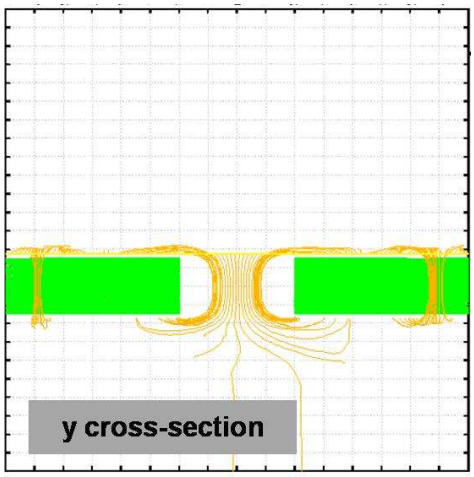

Figure 9.14: GARFIELD simulation of the photoelectrons trajectories, THGEM cross-section along the y-axis; drift field: 0.5 kV/cm.

smaller, namely for lower dipole field. These features confirm the modellisation discussed above and suggest that a pretty high voltage has to be applied to the THGEM, which is the substrate of the photocathode.

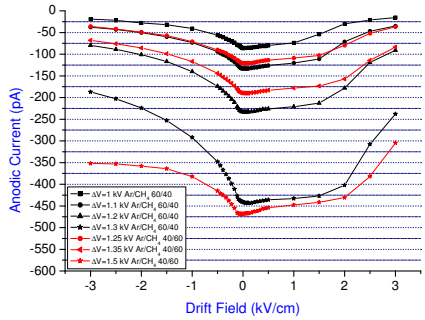

Figure 9.15: Anodic current versus drift field for different values of the dipole voltage ΔV; two gas mixtures have been used: Ar/CH_4 (60:40) (black) and Ar/CH_4 (40:60) (red).

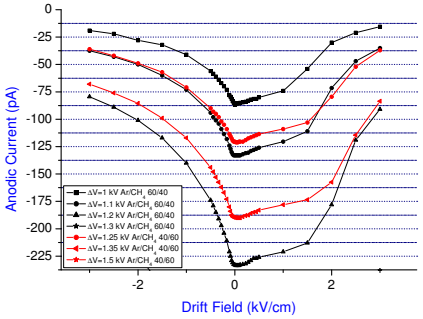

Figure 9.16: Same as Fig. 9.15 with larger y-axis scale.

9.5 Ion feedback in THGEM-based photon detectors

The ion feedback rate to the photocathode has been estimated illuminating the photocathode and measuring the currents on all the electrodes. A typical result (Table 9.2) has been obtained with a triple THGEM structure in Ar/CH_4 (50:50) gas mixture. The THGEM geometry is: d=0.4 mm, p=0.8 mm, t=0.4 mm and rim=10 μm. At an effective gain of 10^6 the total amount of electron produced is about 2×10^6 and the ion flow to the photocathode is a quarter of that amount, namely about 5×10^5. This value is too high and should be ten times smaller to avoid the long recovery time after a detector trip and CsI ageing effects, as discussed in Sec. 2.3. The further reduction of the ion feedback flow requires dedicated work, not performed in the context of this thesis. Possible handles are

- the use, for the intermediate THGEM layer, of a less transparent THGEM, namely a THGEM with smaller holes or
- the use, as first THGEM, of a THGEM with a more articulated electrode pattern; the top face, which is CsI coated, remains the same,

while the bottom face includes, between the standard electrodes surrounding the holes, a second set of electrodes kept at a potential more negative than that of the standard ones, so to collect there the positive ions (Cobra structure [113]).

Electrode	Current Sign	Current Fraction
THGEM1,top (photocathode)	+	26 %
THGEM1, bottom	+	1 %
THGEM2, top	+	5 %
THGEM2, bottom	-	4 %
THGEM3, top	+	68 %
THGEM3, bottom	-	49 %
Anode	-	47 %

Table 9.2: Current sharing on the electrodes of a triple THGEM detector; detector parameters are given in the text.

9.6 Conclusions about the single photon detection

We have demonstrated that single photons can be efficiently detected employing stable THGEM-based detector operating at high gain. The various measurement campaigns reported here indicate how to design and optimise a THGEM-based photon detector. The only open point that still requires further study is the reduction of the ion feedback rate.

The parameters of the THGEM geometry are suggested:

- by the request of gain stability (rim $\leq$10 μm) and
- by the necessity to establish a good compromise between the request to maximise the active area and the need to have high electric field at the photocathode surface; for instance, an adequate choice is t=0.4 mm, d=0.4 mm and p=0.8 mm.

A multilayer structure is mandatory to get large gain, an essential request to reach high efficiency in single photon detection, due to the exponential

shape of the amplitude spectrum; moreover, the multilayer architecture allows to eliminate the feedback of the photons from the multiplication region and it is a handle to limit the ion feedback to the photocathode. It has been shown that a detector with this architecture has a typical time resolution around 10 ns. Adequate gas mixtures are pure methane or argon methane with consistent methane fraction (∼50%): this is both to limit the photoelectron loss due to electron backscattering in the gas, and to operate at high voltage, thus producing a high electric field at the photocathode surface, a condition that favors the photoelectron extraction. As a consequence, the total voltage across a three THGEM layer detector in operating conditions can reach 8 kV.

The studies reported in this thesis have been performed using small prototypes. They are part of an R&D project aiming at the development of THGEM-based photon detectors of large size (active surface ∼600×600 mm^2). This goal implies engineering aspects not discussed within this thesis. For completeness, they are shortly mentioned here. For example, the 576×576 mm^2 THGEM sample shown in Fig. 6.13 presents no holes in two strips along the diagonals: a reinforcement has to be glued in this area in order to give more stiffness to the plate reducing the sagitta when an electric field is present.

Another critical issue requiring engineering skill is the electrical insulation of all the electrodes respect to the detector box and all the fed-through elements.

THGEMs have huge capacitance. For example, for t=0.4 mm, a 30×30 mm^2 THGEM has a capacitance of ∼100 pF, a 100×100 mm^2 THGEM of ∼1.2 nF and a 600×600 mm^2 THGEM of ∼20 nF. In case of discharges, large energy is transfered, which can destroy the read-out electronics. To overcome this problem, the front-end electronics must be equipped with protection circuits and the THGEM surface must be properly segmented in sectors having smaller capacitance.

Chapter 10

Conclusions

The R&D activity reported about in this thesis represents an important step forward towards the construction of THGEM-based detectors. The parameter choices to obtained stable detectors have been determined, as illustrated in Sec. 7.8; these results are relevant for all possible application of THGEM electron multipliers. Concerning photon detectors employing THGEMs, several key points have been studied (Chapters 8 and 9) and the only principle problem still open is the ion feedback level that can be reached (Sec. 9.5). Part of the engineering aspects of THGEM-based photon detectors have been faced and solved in the construction of the detector prototypes used for our studies (Secs. 5.2 and 5.9). Those related to the construction of large size detectors still need dedicated efforts.

In conclusion, the possibility to use in experiments a new generation of gaseous photon detectors employing THGEMs for Cherenkov imaging application is presently very near.

Bibliography

[1] http://rd51-public.web.cern.ch/RD51-Public/Welcome.html

[2] P.A. Cherenkov, Phys. Rev. **52** (1937) 378.

[3] I.E. Tamm, I.M. Frank, Dokl. Akad. Nauk SSSr **14** (1937) 107.

[4] E. Nappi, "RICH detectors", Lectures at 8^{th} ICFA School on Instrumentation in Particle Physics (Istanbul, 1999), CERN-EP/99-149

[5] E. Albrecht *et al.*, Nucl. Instr. and Meth. **A 502** (2003) 112; E. Albrecht *et al.*, Nucl. Instr. and Meth. **A 518** (2004) 586; E. Albrecht *et al.*, Nucl. Instr. and Meth. **A 553** (2005) 215.

[6] M. Alekseev *et al.*, Nucl. Instr. and Meth. **A 553** (2005) 53; P. Abbon *et al.*, Nucl. Instr. and Meth. **A 567** (2006) 114; P. Abbon *et al.*, Nucl. Instr. and Meth. **A 572** (2007) 419; P. Abbon *et al.*, Studies for a fast RICH, World Scientific ISBN 981-256-798-4,Singapore, 2006, page 103; P. Abbon *et al.*, Nucl. Instr. and Meth. **A 580** (2007) 906; P. Abbon *et al.*, Nucl. Phys. **B**, Proc. Suppl., **172** (2007) 75; P. Abbon *et al.*, Nucl. Instr. and Meth. **A 581** (2007) 419; P. Abbon *et al.*, Nucl. Instr. and Meth.**A 587** (2008) 371.

[7] The ALICE collaboration, Technical Design Report of the High Momentum Particle Identification Detector, CERN/LHCC 98-19, ALICE TDR 1, 14 August 1998.

[8] A. Braem *et al.*, Nucl. Instrum. and Meth. in Phys. Research **A 499** (2003) 720.

[9] I. Adam *et al.*, Nucl. Instr. and Meth. **A 538** (2005) 281.

[10] M. Pommot Maia *et al.*, Nucl. Instrum. and Meth. **A 326** (1993) 496; J. Engelfried et al., The SELEX Phototube RICH detector, Fermilab/Pub-98/299-E, hep-ex/9811001.

[11] Blair N. Ratcliff, Nucl. Instrum. and Meth. in Phys. Research **A 371** (1996) 309.

[12] PHENIX Conceptual Design Report, January 1993.

[13] P. Krizan *et al.*, Nucl. Instrum. and Meth. **A 387** (1997) 146.

[14] P. Abbon *et al.*, Nucl. Instrum. and Meth. **A 595** (2008) 177.

[15] P. Weilhammer, Nucl. Instrum. and Meth. **A 446** (2000) 289.

[16] M. Yokoyama *et al.*, Nucl. Instr. and Meth. **A 610** (2009) 362.

[17] S. Korpar, *"Particle identification system for Belle-II"* presented at the 11th ICATPP Conference, Como, 5-9 October 2009.

[18] E. Albrecht *et al.*, Nucl. Instrum. and Meth. **A 433** (1999) 47 and references therein.

[19] R. McCarthy *et al.*, Nucl. Instrum. and Meth. **A 248** (1986) 69.

[20] H.-W. Siebert *et al.*, Nucl. Instrum. and Meth. **A 343** (1994) 60.

[21] M. Artuso *et al.*, Nucl. Instrum. and Meth. **A 554** (2005) 147.

[22] The RD26 Collaboration, RD26 status reports: CERN/DRDC 93-36, CERN/DRDC 94-49, CERN/DRDC 96-20; Nucl. Instrum. and Meth. **A 371** (1996) 96.

[23] J. Friese *et al.*, Nucl. Instrum. and Meth. **A 438** (1999) 86; for the NA44 collaboration, M. Spegel, Nucl. Instrum. and Meth. **A 433** (1999) 366.

[24] J. Friese *et al.*, Nucl. Instrum. and Meth. **A 438** (1999) 86; H. Rabus *et al.*, Nucl. Instrum. and Meth. **A 438** (1999) 94; R. Gernhaeuser *et al.*, Nucl. Instrum. and Meth. **A 438** (1999) 104.

[25] E. Albrecht *et al.*, Nucl. Instrum. and Meth. **A 553** (2005) 215 and references therein.

[26] F. Garibaldi *et al.*, Nucl. Instrum. and Meth. **A 502** (2003) 117; M. Iodice *et al.*, Nucl. Instrum. and Meth. **A 553** (2005) 231.

[27] A. Braem *et al.*, Nucl. Instrum. and Meth. **A 553** (2005) 187; H. Hoeldmoser *et al.*, Nucl. Instrum. and Meth. **A 574** (2007) 28.

[28] Z. Fraenkel *et al.*, Nucl. Instrum. and Meth. **A 546** (2005) 466.

[29] A. Milov *et al.*, J. Phys. G Nucl. Part. Phys. **34** (2007) S701.

[30] W. R. Leo, *Techniques for Nuclear and Particle Physics Experiment*, Springer-Verlag Ed.

[31] `http://indico.cern.ch/getFile.py/access?resId=1&materialId=68confId=a042930`

[32] `http://en.wikipedia.org/wiki/File:Wire_chamber.gif`

[33] W. Blum, W. Riegler and L. Rolandi, *Particle Detection with Drift Chambers*, Second Edition, Springer.

[34] `http://www.phenix.bnl.gov/WWW/tracking/dc/experts/Drift_Chamber_principle_of_operation.html`

[35] `http://www-flc.desy.de/tpc/img/TPCeng.jpg`

[36] R. Santonico *et al.*, Nucl. Instrum. and Meth. **A 263** (1988) 20.

[37] A. Sharma, Nucl. Instrum. and Meth. **A 602** (2009) 854 and references therein.

[38] A. Oed, Nucl. Instr. Meth., **A 263** (1988) 351.

[39] A. Akindinov *et alias*, Nucl. Instrum. and Meth. **A 602** (2009) 372.

[40] Y. Giomataris *et alias*, Nucl. Instrum. and Meth. **A 376** (1996) 29.

[41] "*GAS ELECTRON MULTIPLIER DETECTORS: performance and applications*", MPGD Workshop CERN, January 20, 2006; `http://gdd.web.cern.ch/GDD/`

[42] F. Sauli, Nucl. Instrum. and Meth. **A 386** (1997) 531.

[43] J. Benlloch *et al.*, IEEE NS-45 (1998) 234.

[44] S. Bachmann *et al.*, Nucl. Instrum. and Meth. in Phys. Research **A 438** (1999) 376 and references therein.

[45] A. Bressan *et al.*, Nucl. Instrum. and Meth. **A 424** (1999) 321; S. Bachmann *et al.*, Nucl. Instrum. and Meth. **A 479** (2002) 294.

[46] R. Veenhof, Nucl. Instrum. and Meth. **A 419** (1998) 726.

[47] V. Tikhonov, R. Veenhof, Nucl. Instrum. and Meth. **A 478** (2002) 452.

[48] P. Abbon *et al.*, Nucl. Instrum. and Meth. **A 577** (2007) 455.

[49] C. Altunbas *et al.*, Nucl. Instrum. and Meth. **A 490** (2002) 177.

[50] B. Ketzer *et al.*, IEEE Trans. Nucl. Sci. **N12-5**, Vol.1, 242-244; M. Kramer *et al.*, IEEE Trans, Nucl. Sci. **N43-6**, 2920-2925.

[51] `http://gdd.web.cern.ch/GDD/` under COMPASS directory.

[52] M.J. French *et al.*, Nucl. Instr. and Meth. **A 466** (2001) 359.

[53] G. Anelli *et al.*, 2008 JINST **3** S08007.

[54] M.G. Bagliesi *et al.*, "The TOTEM T2 telescope based on triple-GEM chambers", Nucl. Instrum. and Meth. **A** (2009), in press.

[55] A. Augusto Alves Jr.*et al.*, 2008 JINST **3** S08005.

[56] M. Alfonsi *et al.*, Nucl. Instr. and Meth. **A 572** (2007) 12.

[57] LC-TPC Collaboration, `https://wiki.lepp.cornell.edu/ilc/bin/view/Public/WWS/`

[58] L. Schmitt *et al.*, Nucl. Instrum. and Meth. **A 581** (2007) 542; `http://www.gsi.de/informationen/wti/library/scientificreport2007/PAPERS/FAIR-EXPERIMENTS-35.pdf`.

[59] V. Dangendorf *et al.*, Nucl. Instr. and Meth. **A 542** (2005) 197.

[60] C. Iacobaeus et al., IEEE Trans. Nucl. Sci,48 (2001) 1496; J. Ostling et al., IEEE Trans. Nucl. Sci., 50 (2003) 809.

[61] C. Hagmann, A. Bernstein, IEEE Trans. Nucl. Sci. **51** (2004) 2151; P.S. Barbeau, J.I. Collar, J. Miyamoto, I. Shipsey, IEEE Trans. Nucl. Sci. **50** (2003) 2185.

[62] J. Dodd, et al., Private communication and the report on The Nevis Laboratories Summer 2000 Education Workshop, BNL and Columbia University (Nevis Laboratories), 2000, unpublished. See also `http://www.nevis.columbia.edu/ebubble/`.

[63] A. Rubbia, e-print:hep-ph/0510320 (2005).

[64] M. Chen, A. Bolozdynya, US patent 5665971, 1997.

[65] A. Buzulutskov A. et al., Two-phase cryogenic avalanche detectors for astroparticle and medical imaging // Proposal for INTAS grant 04-78-6744. 2004. Proc. of the SNIC Symposium, Stanford, California, Apr.3-6 (2006).

[66] A. Bondar *et al.*, Nucl. Instr. and Meth. **A 581** (2007) 241.

[67] T. Meinschad *et al.*, Nucl. Instr. and Meth. **A 535** (2004) 324; F. Sauli, Nucl. Instr. and Meth. **A 553** (2005) 18.

[68] I. Tserruya *et al.*, IEEE CNF Vol. **2** (2004) 1137.

[69] B. Azmoun *et al.*, IEEE Trans. Nucl. Sci. Vol. **56** (2009) 1544.

[70] A. Buzulutskov *et al.*, Nucl. Instr. and Meth. **A 442** (2000) 68; D. Mörmann *et al.*, Nucl. Instr. and Meth. **A 504** (2003) 93.

[71] R. Chechik *et al.*, Nucl. Instr. and Meth. **A 502** (2003) 195.

[72] A. C. Agocs *et al.*, JINST 3 P02012, February 2008.

[73] P. Martinengo *et al.*, Nucl. Instr. and Meth. **A 604** (2009) 8.

[74] R. Chechik *et al.*, Nucl. Instr. and Meth. **A 535** (2004) 303.

[75] J.M. Bidault *et al.*, Nucl. Phys. **B**(Proc. suppl) **158** (2006) 199.

[76] A. White, *"Digital Hadron Calorimetry for the International Linear Collider using GEM technologies"*, presented at the 1st International Conference on Micro Pattern Gaseous Detectors, MPGD2009, Kolympari, Crete, Greece, 12-17 June 2009.

[77] K. Gnanvo, private communication.

[78] A. Rubbia, private communication.

[79] R.Veenhof, GARFIELD, simulation program for gaseous detectors, CERN, Version 6.33; V. Tikhonov and R. Veenhof, Nucl. Instr. and Meth. **A 360** (1995) 481.

[80] C. Shalem *et al.*, Nucl. Instr. and Meth. **A 558** (2006) 475 and references therein.

[81] C. Shalem *et al.*, Nucl. Instr. and Meth. **A 558** (2006) 468.

[82] C. Shalem, M.Sc. Thesis, *R&D of a novel electron multiplier - the THGEM*,
`http://jinst.sissa.it/jinst/theses/2005$\_$JINST$\_$TH$ \_$001.pdf.`

[83] A. Buzulutskov *et al.*, Nucl. Instr. and Meth. **A 443** (2000) 164.

[84] A. Breskin *et al.*, Nucl. Instr. and Meth. **A 483** (2002) 670.

[85] S. Mukhopadhyay , *"Electrostatics of Micromesh-Based Detectors", presented at the 1st International Conference on Micro Pattern Gaseous Detectors*, MPGD2009, Kolympari, Crete, Greece, 12-17 June 2009.

[86] R. Veenhof, private communication.

[87] M. Alfonsi and G. Croci, private communication.

[88] M. Cortesi *et al.*, 2009 JINST 4 P08001.

[89] R. Alon *et al.*, 2008 JINST 3 P01005.

[90] A. Breskin *et al.*, Nucl. Instr. and Meth. **A 598** (2009) 107.

[91] R. Alon *et al.*, 2008 JINST 3 P11001.

[92] R. Alon, M.Sc.Thesis, *Noble-gas operation, timing and imaging properties of Thick Gaseous Electron Multiplier (THGEM)-based radiation detectors*,
`http://jinst.sissa.it/jinst/theses/2008$\_$JINST$_$TH$\ \_$001.pdf.`

[93] M. Cortesi *et al.*, 2007 JINST 2 P09002.

[94] R. Oliveira *et al.*, Nucl. Instr. and Meth. **A 576** (2007) 362.

[95] B. Clark *et al.*, "Development and preliminary tests of Resistive GEMs manufactred by a screen printing technology", arXiv:0708.2344, Aug. 2007.

[96] G. Charpak *et al.*,IEEE Trans. Nucl. Sci., vol.55, no.3, June 2008.

[97] A. Di Mauro *et al.*,IEEE Trans. Nucl. Sci., vol.56, no.3, June 2009.

[98] TECAPEEK GF 30; datasheet in www.ensinger.ltd.uk.

[99] www.keithley.com; Model 6517A Electrometer User's Manual Rev. D, A-2 Specifications.

[100] `http://www.lumenera.com/resources/documents/datasheets/industrial/Lu270-Lu275-datasheet.pdf`

[101] P. Abbon *et al.*, Nucl. Instr. and Meth. **A 587** (2008) 371.

[102] F. Gonnela, M. Pegoraro, CERN-LHCC-2001-034, p. 204.

[103] H. Fischer *et al.*, Nucl. Instr. and Meth. **A 461** (2001) 507.

[104] M. Alexeev *et al.*, IEEE NSS '08, pages 1335-1340.

[105] F. Tessarotto, "Production of THGEM at ELTOS S.p.A.", talk at 2nd RD51 Collaboration meeting, Paris, France, 13-15 October 2008, `http://indico.cern.ch/materialDisplay.py?contribId=31&sessionId=20&materialId=slides&confId=35172`.

[106] M. Alfonsi *et al.*, "Performance measurements on closed geometry GEM-like detectors", poster presented at the MPGD2009 conference, Kolympari,Crete, Greece, `http://candia.inp.demokritos.gr/mpgd2009/`, to be submitted to JINST.

[107] J. Escada *et al.*, 2009 JINST **4** P11025.

[108] D.F. Anderson, S. Kwan, V. Peskov, Nucl. Instr. and Meth. **A 343** (1994) 109.

[109] A. Di Mauro *et al.*, Nucl. Instr. and Meth. **A 371** (1996) 137.

[110] J. Almeida *et al.*, Nucl. Instr. and Meth. **A 367** (1995) 332.

[111] A. Breskin *et al.*, Nucl. Instr. and Meth. **A 344** (1994) 537.

[112] A. Valentini *et al.*, Nucl. Instr. and Meth. **A 482** (2002) 238.

[113] A. Lyashenko *et al.*, Nucl. Instr. and Meth. **A 598** (2009) 116.

Acknowledgement

My heartfelt thanks go to Prof. Daniele Panzieri and Dr. Silvia Dalla Torre because they gave me the opportunity to investigate an interesting and new topic such as the THGEM-based photon detector within a stimulating and international framework. In particular, I'm very grateful to Dr. Silvia Dalla Torre who supervised and corrected my thesis coping with the many obligations as Director of Sezione INFN of Trieste.

I owe a special thank-you to Dr. Leszek Ropelewski, leading the MPGD group at CERN who taught not only the "secrets" of the gaseous detectors, but also how to grow up as a physicist broadly speaking.

The several THGEM tests performed within the THGEM collaboration during my Ph.D. period, here at CERN, have been particularly interesting in the scientific aspect and certainly unforgettable for the nice company. I owe to thank Dr. Fulvio Tessarotto who organised and led these THGEM tests and my colleagues: Maxim Alekseev, Michela Chiosso, Vera Jahodova, Stefano Levorato, Jarda Polak, Christian Schill, Sebastian Schopferer, Dr. Miloslav Slunecka, Lukas Steiger, Prof. Miroslav Sulc and Heiner Wollny for sharing pleasant night and day shifts.

I'd like to thank Serge Duarte Pinto, Marco Villa and Miranda Van Stenis for the nice time spent together in the MPGD laboratory and for the useful discussions about the gaseous detectors physics. In particular from the colleagues of the GDD group I want to thank Gabriele Croci who was always present when I needed a help and who gave me his friendship as a present.

A big thanks to all my colleagues from Torino and Trieste, in particular to: Antonio Amoroso, Andrea Bressan, Marialaura Colantoni, Vinicio Duic, Carmine Elia, Ivan Gnesi, Giulia Pesaro, Giulio Sbrizzai, Stefano Sosio, Fed-

erica Sozzi and Stefano Takekawa for the always present and kind remote support.

Moreover I think of myself as a lucky person because I have friends who showed me with their friendship that the distance is just a relative concept; so thanks to: Carlo Battilana, Giuseppe Codispoti, Erica Fanchini, Sara Furcas, Teresa Negrini, Jerome Samarati and Massimo Venaruzzo.

The search of the proper words explaining my whole gratitude to my parents will never ends complete. I hope that, Mum&Dad, you will understand, as usual, the feelings going beyond the mere words.

I'm keeping the special place of thank-you for my fiancé, Matteo. Your professionalism as physicist, your patience, your determination and our love are my reference points by now for becoming a better person.